JETP Letters, Vol. 73, No. 7, 2001, pp. 313–316. Translated from Pis'ma v Zhurnal Éksperimental'noĭ i Teoreticheskoĭ Fiziki, Vol. 73, No. 7, 2001, pp. 355–358.

Cosmic Rays of Energies $E_0 \geq 10^{19}$ eV and the Large-Scale Structure of the Universe

A. V. Glushkov

Institute of Cosmophysical Research and Aeronomy, Yakut Research Center, Siberian Division, Russian Academy of Sciences, pr. Lenina 31, Yakutsk, 677891 Russia

e-mail: a.v.glushkov@ikfia.ysn.ru

Received March 1, 2001

Arrival directions of cosmic rays with energies $E_0 \geq 10^{19}$ eV are analyzed in the supergalactic coordinates. It is shown that increased particle fluxes arrive from the supergalactic plane and regions symmetrically adjoining it at angles $\pm b_{SG} \approx 6.5°$. Relatively high densities of clusters of galaxies and quasars, which are related to the large-scale structure of the universe, are observed in these regions. © *2001 MAIK "Nauka/Interperiodica"*.

PACS numbers: 98.70.Sa; 98.65.Dx; 96.40 Pq

1. A search for the sources of primary cosmic radiation (PCR) which forms extensive air showers (EASs) of energies $E_0 \geq 10^{19}$ eV is one of the most difficult problems in studying the origin of PCR with extremely high energies. The reason is that their fluxes are very low. World data accumulated to date [1–5] includes ≈2500 such events. On the global scale, these data do not contradict the isotropic distribution, although they indicate some correlation between the arrival directions and the galactic plane (see, e.g., [6–9]).

Stanev *et al.* [10] have demonstrated that cosmic rays of energies $E_0 \geq 4 \times 10^{19}$ eV also show positive correlation with the plane of local galactic supercluster (Supergalaxy). To some extent, this conclusion was corroborated by the Akeno Giant Air Shower Array (AGASA) group [5], although a statistically significant result was not obtained. Strong correlation between the PCR with $E_0 \geq 10^{19}$ eV and the supergalactic plane was observed in [9, 11], where the Yakutsk EAS array data were examined.

2. Characteristics being studied and discussion. Below, Yakutsk data collected in 1974–2000 on the EASs with $E_0 \geq 10^{19}$ eV and zenith angles $\theta \leq 60°$ are considered. These events are selected by the largest number of detectors with an efficiency of ~100% and provide minimum errors for the basic parameters of EASs (axis directions and coordinates, E_0, etc.). Moreover, the primary particles with such energies are least subjected to magnetic fields, so that their arrival directions indicate the sources most trustworthy.

In Fig. 1a, the observed N_{exp} (histogram) and the expected N_{ran} (line) distributions of arrival directions of 583 showers with indicated energies are presented as functions of their arrival latitude b_{SG} in the supergalactic coordinates (the equatorial coordinates of the north pole of the Supergalaxy are $\alpha = 286.2°$ and $\delta = 14.1°$) with step $\Delta b_{SG} = 2°$. Figure 1b shows the deviations $n_\sigma = (N_{exp} - N_{ran})/\sigma$ of the number of detected occurrences from their expected number in standard units $\sigma = \sqrt{N_{ran}}$. In my opinion, this representation is most convenient because it equalizes the statistics in different Δb_{SG} intervals and reflects the pattern as a whole.

The N_{ran} values were found from the following drawing of occurrences randomly distributed over the celestial sphere. For each shower, 500 directions in the supergalactic coordinates were obtained through replacing the measured real arrival time and azimuth by random values (in the horizontal coordinate system of the array). The resulting distributions of random occurrences were then normalized in magnitude to the real distributions.

Figure 1 demonstrates that the enhanced PCR fluxes are observed from the supergalactic disk ($|\Delta b_{SG}| \leq 2°$) and from the regions symmetrically adjoining it at angles $\pm b_{SG} \approx 6°–7°$ (peaks *2* and *3*). They are particularly pronounced on the background of the symmetrically arranged neighboring dips $\approx -1\sigma$ at $|\Delta b_{SG}| = 12°–20°$.

Let us focus on these details of distributions and leave aside for a while the other properties. It is believed that peaks *1–3* are not accidental. This is corroborated by the distribution shown in Fig. 2 for 44 and 50 showers with energies $E_0 \geq 10^{19}$ eV taken from [1] and reported by Nagano,[1] respectively, as well as 47 showers with $E_0 \geq 4 \times 10^{19}$ eV taken from [5]. The expected distribution N_{ran} was obtained according to the above-mentioned method through replacing the measured real right ascension by its random value in the range 0°–360°. These showers were detected at the Vol-

[1] M. Nagano, private communication, Kofu, 1990.

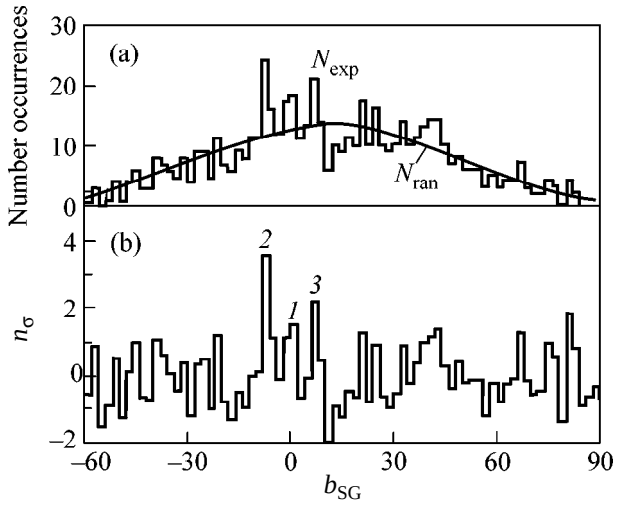

Fig. 1. Distributions of 583 showers with $E_0 \geq 10^{19}$ eV and zenith angles $\theta \leq 60°$ detected at the Yakutsk EAS array as functions of their arrival latitude in the supergalactic coordinates with step $\Delta b_{SG} = 2°$. (a) N_{exp} is experimental data, and N_{ran} is the distribution expected for an isotropic flux; (b) $n_\sigma = (N_{exp} - N_{ran})/\sqrt{N_{ran}}$; *1–3* are the peaks near the supergalactic plane.

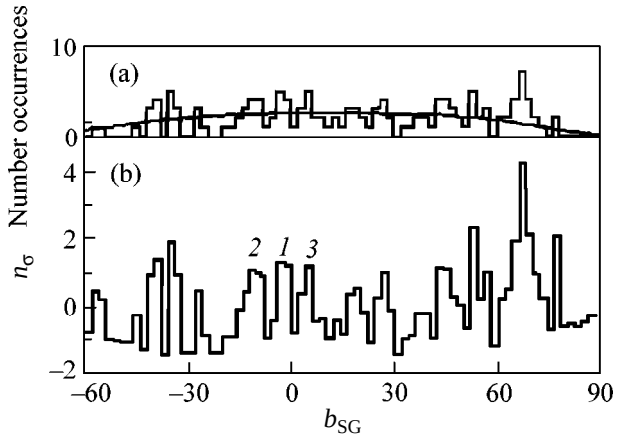

Fig. 2. The same as in Fig. 1, but for 141 showers detected at the Volcano Ranch array [1] and AGASA[1] [5].

cano Ranch array [1] and AGASA[1] [5], which are similar to the Yakutsk array in the detector type (scintillation counters) and methods of sampling and processing EASs.

Peaks *1–3* are also seen in Fig. 2, although the number of occurrences in this figure is one-fourth that in Fig. 1. The peaks are merely shifted leftward from 0 by ≈–2°. This shift may be of accidental character. The mutual arrangement of the peaks is the same as in Fig. 1. The other details of these distributions also coincide to some extent.

The observations and the theory indicate (see, e.g., [12]) the presence of large (100–130 Mpc) voids separated by comparatively thin (20–30 Mpc) layers in the universe. These layers concentrate up to 60–80% of galaxies that tend to group into elongated and oblate superclusters. One of them is the Supergalaxy under consideration (with diameter 50–60 Mpc). Many superclusters are likely joined together to form a unified cellular structure of the universe [12].

Based on an analysis of the correlations between the arrival directions of cosmic rays with $E_0 \geq 10^{18}$ eV and the galactic and supergalactic planes, it was assumed in [9] that the particles with these energies are predominantly of an extragalactic origin and are electrically neutral. This is corroborated by the results presented in Figs. 1 and 2, which reflect, to some extent, the distribution of the PCR sources in the ordered structure of the universe.

Splitting of the PCR arrival directions into peaks *1–3* can be treated as a corroboration of the adiabatic ("pancake") Zel'dovich theory [13], in which the geometry of metagalactic structures is characterized by the presence of giant planar structures separated by large (~10^5 Mpc) volumes almost free of galaxies.

Let us consider some universe objects that can clarify the origin of peaks *1–3*. Figure 3 (upper panel) shows the latitudinal distribution of 49 superclusters in the supergalactic coordinates. These superclusters are localized in the region of galactic latitudes $b_G > 30°$ and at distances of 100–500 Mpc [14]. This sample is complemented by 52 randomly chosen clusters and bright galaxies at distances of ≥10 Mpc [15, 16]. In this figure, peaks *2* and *3* are also seen near the supergalactic plane. Although these peaks may be ≈1.5° closer to the supergalactic plane, they approximately coincide with the respective peaks in Figs. 1 and 2. Note that peak *2* includes the central part of the Virgo supercluster and peak *3* includes the Coma Berenices supercluster, which involve several galactic clusters at various distances up to ~1000 Mpc [12].

Figure 3 (lower panel) shows the distribution of 131 quasars [17] with red shifts $z \leq 0.2$ [at distances of ≤800 Mpc for $H = 75$ km/(s Mpc)]. Peaks *2* and *3* coinciding with the respective peaks in Fig. 1 are clearly seen in this figure. This may indicate that PCR with energies of interest originates from quasars. The absence of peak *1* in Fig. 3 is possibly due to the fact that the optical radiation from quasars is absorbed by denser matter in the supergalactic plane. For cosmic rays of ultrahigh energies, the universe structure is more transparent.

The data considered above confirm that the matter structure in the universe is ordered on the cosmological scale. Einasto *et al.* [18] assume that this structure may be of the three-dimensional checkerboard type. Peaks *2* and *3* indicate that noticeable concentrations of the galaxy and quasar clusters, where cosmic rays of extremely high energies are possibly generated, are

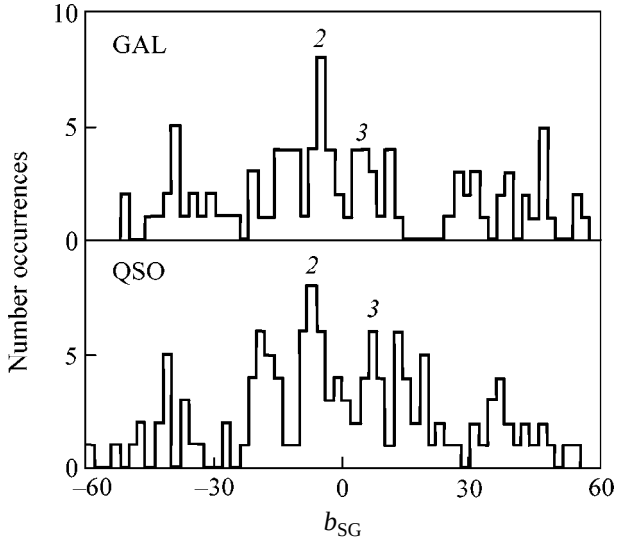

Fig. 3. Latitudinal distributions in the supergalactic coordinates of (GAL) 49 superclusters [14] and 52 clusters and bright galaxies [15, 16] and (QSO) 131 quasars with red shifts $z \le 0.2$ [17]. For peaks *2* and *3*, see Fig. 1.

present at an angular distance of ≈6°–7° on either side of the supergalactic plane.

Let us estimate the transverse dimensions of the structures (that may relate to peaks *2* and *3*) from the relationship $D \approx 2r\tan(6.5°)$ for quasars. According to [19], the sample of quasars with $z \le 0.2$ has a distribution peak at $\langle z\rangle = 0.14$. It follows that $r = c\langle z\rangle/H = 560$ Mpc, where c is the speed of light and $H = 75$ km/(s Mpc). The resulting value $D \approx 127$ Mpc agrees with the above-mentioned dimensions of voids in the cellular structure of the universe [12].

Note that peaks *2* and *3* in Fig. 3 (lower panel) are observed for different red shifts of quasars (see Fig. 4). This likely indicates the global scale of the preferential directions near the supergalactic plane in the universe. Moreover, Fig. 4 shows additional peaks, which are likely due to other fragments of the large-scale structure of the universe.

3. In summary, the Yakutsk EAS array data, the data from [1, 5], and the Nagano data[1] for PCR of energies $E_0 \ge 10^{19}$ eV corroborate the correlation found in [9, 11] between the arrival direction of PCR and the supergalactic plane. In this study, a finer structure (peaks *1*–*3*) in the distribution of PCR of extremely high energies is found.

Peaks *2* and *3* at angles $\pm b_{SG} \approx 6°$–$7°$ with respect to the supergalactic plane are also observed in the galaxy and quasar clusters. The distributions also exhibit other peaks coinciding with each other. One of them at $b_{SG} \approx$ 66°–68° is noteworthy. This suggests that the peaks are not accidental.

The above features of cosmic rays with extremely high energies require further in-depth investigation,

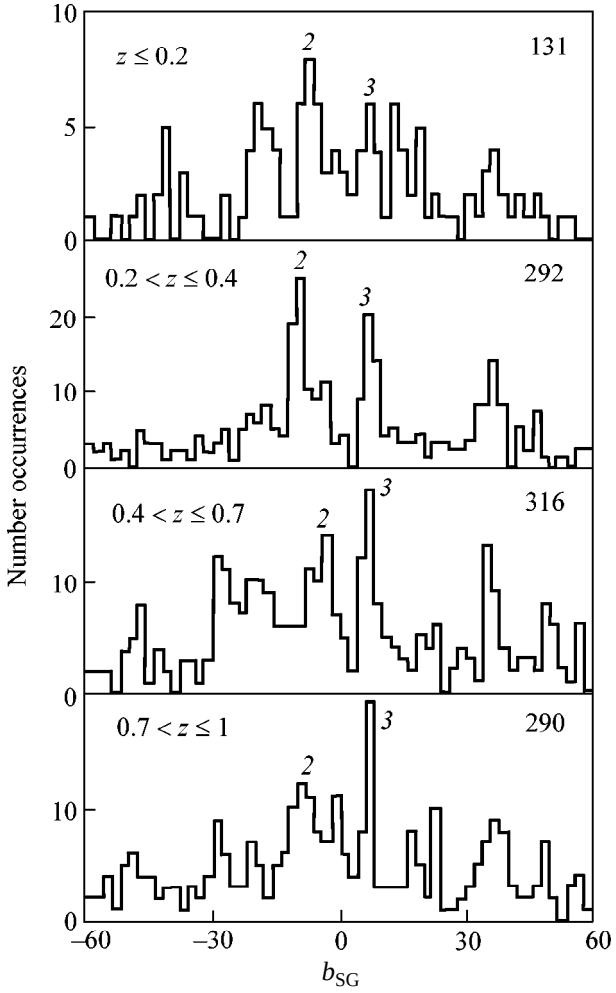

Fig. 4. Latitudinal distributions in the supergalactic coordinates of quasars with red shifts (from top to bottom) $z \le 0.2$, 131 objects; $0.2 < z \le 0.4$, 292 objects; $0.4 < z \le 0.7$, 316 objects; and $0.7 < z \le 1$, 290 objects [17]. For peaks *2* and *3*, see Fig. 1.

and it will be continued. Even now, one can state that the basic sources of particles with these energies are most likely beyond the Galaxy. Their positions in the space are likely associated with the large-scale structure of the universe.

This work was supported by the Ministry of Science of the Russian Federation (support for the Yakutsk complex EAS array included under no. 01-30 in the "Register of Unique Research and Experimental Instruments of National Significance").

REFERENCES

1. J. Linsley, *Catalogue of Highest Energy Cosmic Rays* (Wold Data Center C2 for Cosmic Rays Institute of Physical and Chemical Research, No. 1, Tokyo, 1980).
2. G. Cunningham, D. M. Edge, D. England, *et al.*, *Catalogue of Highest Energy Cosmic Rays* (Wold Data Cen-

ter C2 for Cosmic Rays Institute of Physical and Chemical Research, No. 1, Tokyo, 1980).
3. M. M. Winn *et al.*, *Catalogue of Highest Energy Cosmic Rays* (Wold Data Center C2 for Cosmic Rays Institute of Physical and Chemical Research, No. 2, Tokyo, 1986).
4. N. N. Efimov, T. A. Egorov, D. D. Krasilnikov, *et al.*, *Catalogue of Highest Energy Cosmic Rays* (Wold Data Center C2 for Cosmic Rays Institute of Physical and Chemical Research, No. 3, Tokyo, 1988).
5. M. Takeda, N. Hayashida, K. Honda, *et al.*, Astrophys. J. **522**, 225 (1999).
6. J. Szabelsky, J. Wdowczyk, and A. W. Wolfendale, J. Phys. G **12**, 1433 (1986).
7. B. N. Afanasiev, M. N. Dyakonov, T. A. Egorov, *et al.*, in *Proceedings of the 24th International Cosmic Ray Conference, 1995*, Vol. 2, p. 756.
8. A. A. Mikhailov, in *Proceedings of the 26th International Cosmic Ray Conference, 1999*, Vol. 3, p. 268.
9. A. V. Glushkov and M. I. Pravdin, Zh. Éksp. Teor. Fiz. **119** (2001) (in press) [JETP **92** (2001) (in press)].
10. T. Stanev *et al.*, Phys. Rev. Lett. **75**, 3056 (1995).
11. A. V. Glushkov and I. E. Sleptsov, Izv. Akad. Nauk, Ser. Fiz. **65**, 437 (2001).
12. B. A. Vorontsov-Vel'yaminov *et al.*, in *The Large Scale Structure of the Universe: International Astronomical Union Symposium No. 79, Tallinn, 1977*, Ed. by M. S. Longair and J. Einasto (D. Reidel, Dordrecht, 1978; Mir, Moscow, 1981).
13. Ya. B. Zel'dovich, Pis'ma Astron. Zh. **8**, 195 (1982) [Sov. Astron. Lett. **8**, 102 (1982)].
14. V. S. Lebedev and I. A. Lebedeva, Pis'ma Astron. Zh. **14**, 18 (1988) [Sov. Astron. Lett. **14**, 7 (1988)].
15. V. K. Abalakin, *Astronomical Calendar. Continual Part* (Nauka, Moscow, 1981).
16. M. V. Zombeck, *Handbook of Space Astronomy and Astrophysics* (Cambridge Univ. Press, Cambridge, 1982).
17. A. Hewitt and G. Burbidgr, Astrophys. J., Suppl. Ser. **63**, 1 (1987).
18. J. Einasto *et al.*, Nature **385**, 139 (1997).
19. M. F. Khodyachikh, Astron. Zh. **73**, 11 (1996) [Astron. Rep. **40**, 6 (1996)].

Translated by R. Tyapaev

JETP Letters, Vol. 73, No. 7, 2001, pp. 317–322. From Pis'ma v Zhurnal Éksperimental'noĭ i Teoreticheskoĭ Fiziki, Vol. 73, No. 7, 2001, pp. 359–363.

The Bound State Corrections to the Leptonic Decays of the *B* Meson: The Light-Front Approach Versus ACM Model[1]

I. L. Grach, P. Yu. Kulikov, and I. M. Narodetskii

Institute for Theoretical and Experimental Physics, Moscow, 117259 Russia

e-mail: kulikov@heron.itep.ru

Received February 27, 2001

A generalization of the parton-like formula is used for the first time to find the differential distributions in the inclusive semileptonic weak decays of the *B* meson. The main features of this new approach are the treatment of the *b* quark as an on-mass-shell particle and the inclusion of the effects arising from the *b*-quark transverse motion in the *B* meson. Using the *b*-quark light-front (LF) distribution function related to the equal time momentum wave function taken from the ACM model, we compute the electron energy spectra and the total semileptonic widths of the *B* meson. We find an impressive agreement between the electron energy spectra calculated in the LF approach and the ones obtained in the ACM model, provided the *b*-quark mass is identified with the average of the floating *b*-quark mass in the ACM model. In spite of the simplicity of the model, we obtain a fairly good description of the CLEO data for $|V_{cb}| = 0.042$. © *2001 MAIK "Nauka/Interperiodica".*

PACS numbers: 13.20.He; 12.39.Ki; 14.40.Nd

1. INTRODUCTION

Study of the leptonic spectra in weak semileptonic $B \longrightarrow X_c(X_u)l\nu_l$ decays[2] is important to extract $|V_{cb}|$ and $|V_{ub}|$. The latter plays an important role in the determination of the unitarity triangle. Since the *b* quark is heavy compared to the QCD scale, the inclusive semileptonic *B* decays can be treated with the help of an operator product expansion (OPE) combined with the heavy-quark expansion (HQE) [1]. The result (away from the endpoint of the spectrum) is that the inclusive differential decay width $d\Gamma/dE$ may be expanded in Λ/m_b, where Λ is a QCD-related scale of order 500 MeV, and m_b is the mass of the heavy quark. The leading term (zeroth order in Λ/m_b) is the free-quark decay spectrum, the subleading term vanishes, and the subsubleading term involves parameters from the heavy quark theory, but should be rather small, as it is of order $(\Lambda/m_b)^2$. However, near the end point, the $1/m_b$ expansion has to be replaced by an expansion in twist. To describe this region, one has to introduce a so-called "shape function," which in principle introduces a large hadronic uncertainty. This is quite analogous to what happens for the structure function in deep inelastic scattering in the region where the Bjorken variable $x_B \longrightarrow 1$. A model-independent determination of the shape function is not available at the present time; therefore, a certain model dependence in this region seems to be unavoidable unless lattice data become reasonably precise.

As to phenomenological analyses of the photon spectra up to now, they have been solely based on the ACM model [2, 3]. Various light-front (LF) approaches to the consideration of the inclusive semileptonic transitions were suggested in [4–7]. In [4, 5] the Infinite Momentum Frame prescription, $p_b = \xi P_B$, and, correspondingly, the floating *b*-quark mass, $m_b^2(\xi) = \xi^2 M_B^2$, have been used. The transverse *b*-quark momenta were consequently neglected. In [7], the *b* quark was considered as an on-mass-shell particle with the definite mass m_b, and the effects arising from the *b*-quark transverse motion in the $\bar{B}$ meson were included. The corresponding ansatz of [7] reduces to a specific choice of the primordial LF distribution function $\left|\psi(\xi, p_\perp^2)\right|^2$, which represents the probability of finding a *b* quark carrying an LF fraction ξ and a transverse momentum squared $p_\perp^2 = |\mathbf{p}_\perp|^2$. As a result, a new parton-like formula for the inclusive semileptonic $b \longrightarrow c, u$ width has been derived [7], which is similar to the one obtained by Bjorken *et al.* [8] in case of infinitely heavy *b* and *c* quarks.

In this paper, we use the techniques developed in [7] to evaluate the nonperturbative corrections to the lepton spectrum in the inclusive $B \longrightarrow X_c l\nu_l$ decays. We strive to implement the binding and the *B*-meson wave-function effects on the lepton energy spectrum. The main purpose of the paper is to confront the lepton spectra

[1] This article was submitted by the authors in English.

[2] Throughout this paper, we use the charge conjugated notations.

0021-3640/01/7307-0317$21.00 © 2001 MAIK "Nauka/Interperiodica"

and the total semileptonic decay widths calculated in the LF and ACM approaches. We find that the discrepancy between the two is very small numerically.

2. ACM VERSUS LF

The decay spectrum in the ACM model is determined by the kinematic constrains on the b quark. It incorporates some of the corrections related to the fact that the decaying b quark is not free but in a bound state. The model treats the B meson with mass m_B as consisting of the heavy b quark plus a spectator with fixed mass m_{sp}; the latter usually represents a fitting parameter. The spectator quark has a momentum distribution $\phi(|\mathbf{p}|)$, where $\mathbf{p}$ is its three-dimensional momentum. The momentum distribution is usually taken to be Gaussian:

$$\phi(|\mathbf{p}|) = \frac{4}{\sqrt{\pi}p_f^3}\exp\left(-\frac{|\mathbf{p}|^2}{p_f^2}\right), \tag{1}$$

which is normalized so that the integral over all momenta of $\phi(|\mathbf{p}|)p^2$ is unity. The energy–momentum conservation in the B-meson vertex implies that the b-quark energy $E_b = m_B - \sqrt{\mathbf{p}^2 + m_{sp}^2}$, where m_B is the mass of the B meson; thus the b quark cannot possess a definite mass. Instead, one obtains a "floating" b-quark mass $(m_b^f)^2 = m_B^2 + m_{sp}^2 - 2m_B\sqrt{\mathbf{p}^2 + m_{sp}^2}$ that depends on $|\mathbf{p}|$. The lepton spectrum is first obtained from the spectrum $d\Gamma_b^{(0)}(m_f, E')/dE'$ of the b quark of invariant mass m_b^f (in the b-quark rest frame) and then boosting back to the rest frame of the B meson and averaging over the weight function $\phi(|\mathbf{p}|)$ (further details can be found in the original work [3]).

The LF approach differs from that of the ACM model in two respects. First, similar to the ACM model, the LF quark model treats the beauty meson B as consisting of the heavy b quark plus a spectator quark. Both quarks have fixed masses m_b and m_{sp}, though. This is at variance with the ACM model, which has been introduced in order to avoid the notion of the heavy-quark mass at all. Secondly, the calculation of the distribution over lepton energy in the LF approach does not require any boosting procedure but, instead, is based on the standard Lorentz-invariant kinematic analysis (see, e.g., [9]), which we now briefly discuss.

There are three independent kinematic variables in the inclusive phenomenology, for which we choose the lepton energy E_l, q^2, where $q = p_l + p_{\nu_l}$, and the invariant mass $M_X^2 = (p_B - q)^2$ of a hadronic state. Introducing the dimensionless variables $y = 2E_l/m_B$, $t = q^2/m_B^2$, and $s = M_X^2/m_B^2$, the differential decay rate for semileptonic (SL) B decay can be written as

$$\frac{d\Gamma_{\rm SL}}{dy} = \frac{G_F^2 m_B^5}{64\pi^3}|V_{cb}|^2\int_0^{t_{\max}} dt\int_{s_0}^{s_{\max}} ds$$
$$\times\left\{tW_1 + \frac{1}{2}[y(1+t-s) - y^2 - t]W_2 \right. \tag{2}$$
$$\left. + t\left[\frac{1+t-s}{2} - y\right]W_3 + \ldots\right\},$$

where the structure functions $W_i = W_i(s, t)$ appear in the decomposition of the hadronic tensor $W_{\alpha\beta}$ in Lorentz covariants [9]. The ellipsis in Eq. (2) denotes the terms proportional to the lepton mass squared. The kinematic limits of integration can be found from the equation

$$\frac{s}{1-y} + \frac{t}{y} \le 1. \tag{3}$$

They are given by $0 \le y \le y_{\max} = 1 - (m_{X_c}^{(\min)}/m_B)^2$, where $m_{X_c}^{(\min)}$ is the minimal mass of the hadronic state X_c, $s_{\max} = 1 + t - (y + t/y)$, and $t_{\max} = y(1 - (1 - y_{\max})/(1 - y))$.

3. LIGHT-CONE DISTRIBUTION FUNCTIONS

In a parton model, we treat inclusive semileptonic $B \longrightarrow X_c l\nu_l$ decay in a direct analogy to deep inelastic scattering. Specifically, we assume that the sum over all possible charm final states X_c can be modeled by the decay width of an on-shell b quark into on-shell c quark weighted by the b quark distribution. Following the above assumption, the hadronic tensor $W_{\alpha\beta}$ is written as

$$W_{\alpha\beta} = \int w_{\alpha\beta}^{(cb)}(p_c, p_b)\delta[(p_b - q)^2 - m_c^2] \times\frac{\left|\psi(\xi, p_\perp^2)\right|^2}{\xi}\theta(\varepsilon_c)d\xi d^2p_\perp, \tag{4}$$

where

$$w_{\alpha\beta}^{(cb)}(p_c, p_b) = \frac{1}{2}\sum_{spins}\bar{u}_c O_\alpha u_b\cdot\bar{u}_b O_\beta^+ u_c, \tag{5}$$

with $O_\alpha = \gamma_\alpha(1 - \gamma_5)$. The factor $1/\xi$ in Eq. (4) comes from the normalization of the B-meson vertex [10].

Equation (4) amounts to averaging the perturbative decay distribution over the motion of a heavy quark governed by the distribution function $f(x, p_\perp^2) = \left|\psi(x, p_\perp^2)\right|^2$. In this respect, our approach is similar to the parton model in deep inelastic scattering, although it is not

really a parton model in its standard definition. The normalization condition reads

$$\pi\int_0^1 d\xi\int dp_\perp^2 f(\xi, p_\perp^2) = 1. \quad (6)$$

The function $\theta(\varepsilon_c)$, where ε_c is the c-quark energy, is inserted in Eq. (4) for consistency with the use of the valence LF wave function in calculating the b-quark distribution in the B meson.

Since we do not have an explicit representation for the B-meson Fock expansion in QCD, we will proceed with making an ansatz for $\psi(\xi, p_\perp^2)$. This is a model-dependent enterprise but has a close equivalent in studies of electron spectra using the ACM model. We choose the momentum–space structure of an equal-time (ET) wave function $\phi(|\mathbf{p}|)$ as in Eq. (1). We convert from ET to LF momenta by leaving the transverse momenta unchanged and setting

$$p_{iz} = \frac{1}{2}(p_i^+ - p_i^-) = \frac{1}{2}\left(p_i^+ - \frac{p_{i\perp}^2 + m_i^2}{p_i^+}\right) \quad (7)$$

for both b quark ($i = b$) and quark spectator ($i = sp$). The longitudinal LF momentum fractions ξ_i are defined as $\xi_{sp} = p_{sp}^+/P_B^+$, $\xi_b = p_b^+/P_B^+$, with $\xi_b + \xi_{sp} = 1$. In the B-meson-rest frame, $P_B^+ = m_B$. Then, for the distribution function $|\psi(\xi, p_\perp^2)|^2$ ($\xi = \xi_b$) normalized according to Eq. (6), one obtains[3]

$$|\psi(\xi, p_\perp^2)|^2 = \frac{4}{\sqrt{\pi}p_f^3}\exp\left(-\frac{p_\perp^2 + p_z^2}{p_f^2}\right)\left|\frac{\partial p_z}{\partial \xi}\right|, \quad (8)$$

where

$$p_z^2(\xi, p_\perp^2) = \frac{1}{2}\left((1-\xi)m_B - \frac{p_\perp^2 + m_{sp}^2}{(1-\xi)m_B}\right),$$
$$\left|\frac{\partial p_z}{\partial \xi}\right| = \frac{1}{2}\left(m_B + \frac{p_\perp^2 + m_{sp}^2}{(1-\xi)^2 m_B}\right). \quad (9)$$

The calculation of the structure functions $W_i(t, s)$ in the LF parton approximation (4) is straightforward. The result is

$$W_i(t, s) = \int w_i(s, t, \xi, p_\perp^2)\delta[(p_b - q)^2 - m_c^2] \times \frac{|\psi(\xi, p_\perp^2)|^2}{\xi}\theta(\varepsilon_c)d\xi d^2 p_\perp, \quad (10)$$

where $w_i(s, t, \xi, p_\perp^2)$ are the structure functions for the free-quark decay. For further details, see Appendix in [7]. Equation (10) differs from the corresponding expressions in [4] and [5] by the nontrivial dependence on $p_\perp^2$, which enters both $|\psi(\xi, p_\perp^2)|^2$ and argument of the δ function. For further details, see [7].[4]

4. RESULTS

Having specified the nonperturbative aspects of our calculations, we proceed with presenting numerical results for the lepton spectrum in the decay $B \longrightarrow X_c e\nu_e$. Our main computation refers to the case $m_{sp} = 0.15$ GeV and $m_c = 1.5$ GeV, as chosen in [11].

The choice of m_b in our approach deserves some comments. In the ACM model, it was shown [11, 12] (see also [13]) that the corrections to the first order in $1/m_b$ to both the inclusive semileptonic width and the regular part of the lepton spectrum can be absorbed into the definition of the quark mass: $m_b^{\mathrm{ACM}} = \langle m_b^f \rangle$, where $\langle m_b^f \rangle$ is the value of the floating mass averaged over the distribution $\phi(|\mathbf{p}|)$.

The choice of m_b in the LF approach was first addressed in the context of the LF model for $b \longrightarrow s\gamma$ transitions in [14]. Using the scaling feature of the photon spectrum in the LF model, it was suggested that m_b^{LF} can be defined from the requirement of vanishing of the first moment of the distribution function. This condition coincides with that used in HQE to define the pole mass of the b quark. In this way, one avoids an otherwise large (and model-dependent) correction of order $1/m_b$, though at the expense of introducing the shift in the constituent quark mass, which largely compensates the bound-state effects. It has also been demonstrated that the values of m_b^{LF} found by this procedure agree well with the average values $\langle m_b^f \rangle$ in the ACM model. The photon energy spectra calculated in the LF approach were found to agree well with the ones obtained in the ACM model.

Accepting the identification $m_b^{\mathrm{LF}} = m_b^{\mathrm{ACM}}$, we are now in position to check whether this result holds for the description of other channels like $b \longrightarrow c$. We find again a good agreement between the LF and ACM

[3] On the same footing, one can consider $|\mathbf{p}|$ in Eq. (1) as the *relative* momentum between heavy and light quarks. In this case, it is more convenient to use the quark–antiquark-rest frame instead of the B-meson-rest frame. Recall that in the LF formalism these two frames are different. Then, the longitudinal LF momentum fractions ξ_i are defined as $\xi_{sp} = p_{sp}^+/M_0$ and $\xi_b = p_b^+/M_0$, where the free mass M_0 is $M_0 = \sqrt{m_b^2 + \mathbf{p}^2} + \sqrt{m_{sp}^2 + \mathbf{p}^2}$, with $\mathbf{p}^2 = p_\perp^2 + p_z^2$ and $p_z = \left(\xi - \frac{1}{2}\right)M_0 - (m_b^2 - m_{sp}^2)/2M_0$. In this case, the explicit form of $|\partial p_z/\partial\xi|$ is given, e.g., by Eq. (10) in [6]. We have checked that numerically both approaches yield identical results for the electron spectra.

[4] Note that the expressions for w_i in [7] miss an extra factor of 2.

For the values of p_f in column (1), we display the average value of the floating b-quark mass $\langle m_b^f \rangle$ (both in units of GeV) in the second column and the total semileptonic width of the free b quark (in units of ps^{-1}) in the third column. In the fourth and fifth columns, we compare the total semileptonic widths calculated in the ACM and LF approaches, respectively. In all cases, $m_{sp} = 0.15$ and $m_c = 1.5$ GeV and the radiative corrections are neglected. In the sixth and seventh columns, we give the fractional deviation in percent between the semileptonic widths determined in the LF and ACM models and that of a free quark. A momentum distribution of the b quark is taken in the standard Gaussian form (1) with the Fermi momentum p_f. $|V_{cb}| = 0.04$

p_f	$\langle m_b^f \rangle$	Γ_{SL}^b	$\Gamma_{SL}^{\mathrm{ACM}}$	$\Gamma_{SL}^{\mathrm{LF}}$	δ^{ACM}	δ^{LF}
0.1	5.089	0.1007	0.1005	0.1005	0.2	0.2
0.2	5.004	0.0906	0.0902	0.0901	0.4	0.5
0.3	4.905	0.0799	0.0792	0.0789	0.9	1.2
0.4	4.800	0.0696	0.0688	0.0682	1.1	2.0
0.5	4.692	0.0602	0.0592	0.0584	1.7	3.0

results, but now for the semileptonic $b \longrightarrow c$ decays. The results of our computations of electronic spectra and semileptonic widths are reported in Fig. 1 and the table using $|V_{cb}| = 0.04$. Different curves in Fig. 1 correspond to different values of p_f. For each case, we show separately the inclusive differential semileptonic decay widths for the LF and ACM models and the free-quark decay. The quark-decay spectra vanish for $y > (m_b/m_B)(1 - m_c^2/m_b^2)$, whereas the physical endpoint is $y_{\max} = 1 - m_D^2/m_B^2$, where m_D is the mass of the D meson. In the LF approach, the endpoint for the electronic spectrum is in fact not $y_{\max}$ but $y_{\max}^{\mathrm{LF}} = 1 - m_c^2/m_B^2$. This is the direct consequence of the $p_\perp^2$ integration in Eq. (10) [7]. Note that $y_{\max}^{\mathrm{LF}}$ coincides with $y_{\max}^{\mathrm{ACM}}$ with an accuracy of $\sim m_{sp}/m_B$. For $m_c \sim 1.5$ GeV, the difference between $y_{\max}^{\mathrm{LF}} \sim y_{\max}^{\mathrm{ACM}}$ and $y_{\max}$ is on the order of 10^{-2}. Another possibility advocated in [6] is to sum the electron spectra from the exclusive $B \longrightarrow D$, D^* channels and from the inclusive $B \longrightarrow X_c$ channels, where X_c is the hadronic state with mass $m_{X_c} \geq m_{D^*}$. Such a "hybrid" approach will be considered elsewhere.

In the table, for different values of p_f, we give the corresponding values of the total semileptonic width for a free quark with mass $m_b = \langle m_b^f \rangle$ and the B-meson semileptonic widths calculated using the LF and ACM approaches, respectively. In the last two columns, we give the fractional deviation $\delta = \Delta\Gamma_{SL}/\Gamma_{SL}^b$ (in percent) between the semileptonic widths determined in the LF and ACM models and that of the free quark. The agreement between the LF and ACM approaches for the electronic spectra is excellent for small p_f, as is exhibited in Fig. 1. A similar agreement also holds for integrated rates shown in the table. This agreement is seen to break down at $p_f \geq 0.4$ GeV, but even for $p_f \sim 0.5$ GeV the difference between the ACM and LF inclusive widths is still small and is on the order of a percent level.

Finally, we calculate the $b \longrightarrow c$ spectrum and compare it with the experimental data from the CLEO collaboration [15]. This is a direct calculation of the spectrum and not a χ^2 fit. We briefly investigated the sensitivity of the electronic spectra to the other parameters of the models and found that the choice $p_f = 0.4$ GeV, $m_c = 1.5$ GeV, $m_{sp} = 0.15$ GeV is quite acceptable.

We display the results in Fig. 2, where three theoretical curves are presented for the LF, ACM, and free-quark models. In these calculations, we have implicitly included the $O(\alpha_s)$ perturbative corrections arising from the gluon Bremsstrahllung and one-loop effects, which modify an electron energy spectra at the partonic level (see, e.g., [16] and references therein). It is customary to define a correction function $G(x)$ to the electronic spectrum $d\Gamma_b^{(0)}$ calculated in the tree approximation for the free-quark decay through

$$\frac{d\Gamma_b}{dx} = \frac{d\Gamma_b^{(0)}}{dx}\left(1 - \frac{2\alpha_s}{3\pi}G(x)\right), \qquad (11)$$

where $x = 2E/m_b$. The function $G(x)$ contains the logarithmic singularities $\sim \ln^2(1-x)$ which appear for $m_c = 0$ at the quark-level endpoints $x_{\max} = 1$. This singular behavior at the endpoint is clearly a signal of the inadequacy of the perturbative expansion in this region. The problem is solved by taking into account the bound-state effects [4]. Since the radiative corrections must be convolved with the distribution function, the endpoints of the perturbative spectra are extended from the quark level to the hadron level and the logarithmic singularities are eliminated. In actual calculations, we neglect the terms $\sim\rho$ in $G(x)$ and take this function from [16] [Eq. (4.10)].

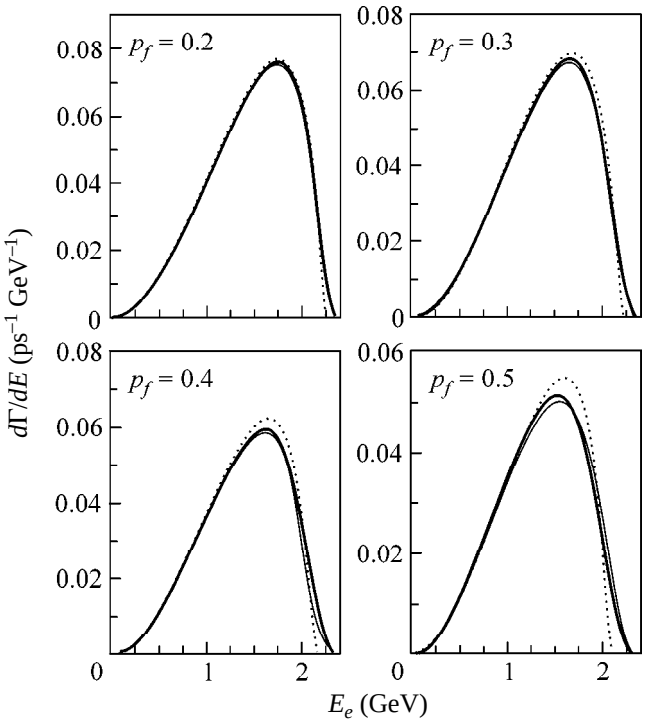

Fig. 1. The inclusive differential semileptonic decay widths $d\Gamma_{SL}/dE_e$ in units ps^{-1} GeV^{-1} for the LF model (thick solid lines), ACM model (thin solid lines), and the free-quark decays (dashed lines). The parameters are p_f = 0.2–0.5 GeV, m_{sp} = 0.15 GeV, and m_c = 1.5 GeV; $|V_{cb}| = 0.04$.

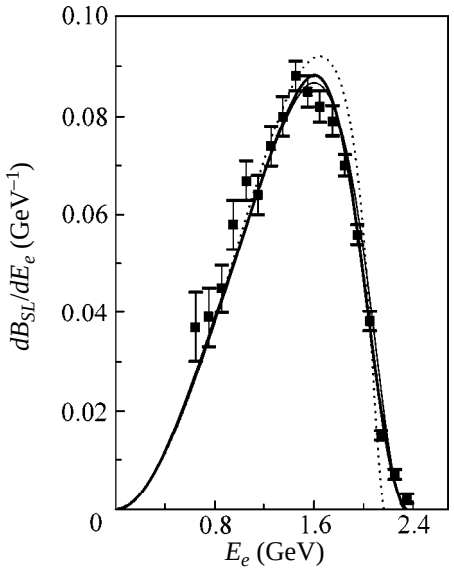

Fig. 2. The predicted electron energy spectrum compared with the CLEO data [15]. The calculation uses p_f = 0.4 GeV, m_b = 4.8 GeV, m_c = 1.5 GeV, and α_s = 0.25 for the perturbative corrections. Thick solid line is the LF result, thin solid line is the ACM result, and dashed line refers to the free-quark decay. The spectra are normalized to 10.16, 10.23, and 10.36%, respectively. $|V_{cb}| = 0.042$.

The agreement with the experimental data is good. Using $|V_{cb}| = 0.042$ for the overall normalization,[5] we obtain for the semileptonic branching ratios

$$BR_{\rm LF} = 10.16\%,$$
$$BR_{\rm ACM} = 10.23\%, \quad (12)$$
$$BR_{\rm free} = 10.37\%,$$

in agreement with the experimental finding [15] $BR_{SL} = 10.49 \pm 0.17 \pm 0.43\%$.

5. CONCLUSIONS

We have applied a new LF formula [7] to calculate the partial electronic spectra in semileptonic B decays. Using the ET and LF b-quark distribution functions related by a simple kinematic transformation, we compared the LF and ACM models by computing the $b \longrightarrow c$ decays for $m_b^{\rm LF} = \langle m_b^f \rangle$. A summary of our results presented in the table and Fig. 1 shows a good agreement between the results of the two models. We have also calculated (Fig. 2) the $b \longrightarrow c$ spectrum including the perturbative corrections and found an agreement with the experimental data from the CLEO collaboration [15]. A more detailed fit to the measured spectrum can impose constraints on the distribution function and the mass of the charm quark. Such a fit should also account for the detector resolution.

The same formulas can also be applied to nonleptonic B-decay widths (corresponding to the underlying quark decays $b \longrightarrow cq_1q_2$), thus making it possible to calculate the B lifetime. A preview of this calculation can be found in [18]. It would be interesting to check whether the effective values of the b-quark mass can prove to be approximately the same for different quark channels and for different beauty hadrons. This work is in progress, and the results will be reported elsewhere.

We thank Marco Battaglia and Pepe Salt for discussions and Karen Ter-Martirosyan for interest in this work. This work was supported in part by the Russian Foundation for Basic Research, project nos. 00-02-16363 and 00-15-96786.

REFERENCES

1. I. Bigi *et al.*, Annu. Rev. Nucl. Part. Sci. **47**, 591 (1997).
2. A. Ali and E. Pietarinen, Nucl. Phys. B **154**, 512 (1979).
3. G. Altarelli, N. Cabbibo, G. Corbo, *et al.*, Nucl. Phys. B **202**, 512 (1982).
4. C. H. Jin, M. F. Palmer, and E. A. Paschos, Phys. Lett. B **329**, 364 (1994); C. H. Jin and E. A. Paschos, in *Proceedings of the International Symposium on Heavy Flavor and Electroweak Theory, Beijing, 1995*, Ed. by C. H. Chang and C. S. Huang (World Scientific, Singapore, 1996), p. 132.

[5] This value agrees with the combined average $|V_{cb}| = (40.2 \pm 1.9) \times 10^{-3}$ in [17].

5. V. L. Morgunov and K. A. Ter-Martirosyan, Yad. Fiz. **59**, 1279 (1996) [Phys. At. Nucl. **59**, 1221 (1996)].
6. I. L. Grach, I. M. Narodetskii, S. Simula, and K. A. Ter-Martirosyan, Nucl. Phys. B **592**, 227 (1997).
7. S. Kotkovsky, I. M. Narodetskii, S. Simula, and K. A. Ter-Martirosyan, Phys. Rev. D **60**, 114024 (1999).
8. J. Bjorken, I. Dunietz, and M. Taron, Nucl. Phys. B **371**, 111 (1992).
9. B. Block, L. Koyrakh, M. Shifman, and A. I. Vainshtein, Phys. Rev. D **49**, 3356 (1994).
10. N. B. Demchuck, I. L. Grach, I. M. Narodetskii, and S. Simula, Yad. Fiz. **59**, 2235 (1996) [Phys. At. Nucl. **59**, 2152 (1996)].
11. L. Randall and R. Sundrum, Phys. Lett. B **312**, 148 (1993).
12. I. Bigi, M. Shifman, N. Uraltsev, and A. Vainstein, Phys. Lett. B **328**, 431 (1994).
13. K. Y. Lee and J. K. Kim, Phys. Lett. B **377**, 153 (1996).
14. Y.-Y. Keum, P. Yu. Kulikov, I. M. Narodetskii, and H. S. Song, Phys. Lett. B **471**, 72 (1999).
15. B. Barish *et al.* (CLEO Collaboration), Phys. Rev. Lett. **76**, 1570 (1996).
16. M. Jezabek and J. H. Kühn, Nucl. Phys. B **320**, 20 (1989).
17. ALEPH, CDF, DELPHI, L3, OPAL, SLD Collab., hep-ex/0009052 (2000).
18. P. Yu. Kulikov, I. M. Narodetskii, and A. I. Onischenko, Pis'ma Zh. Éksp. Teor. Fiz. **71**, 528 (2000) [JETP Lett. **71**, 362 (2000)]; I. M. Narodetskii, hep-ph/0010169.

JETP Letters, Vol. 73, No. 7, 2001, pp. 323–326. Translated from Pis'ma v Zhurnal Éksperimental'noĭ i Teoreticheskoĭ Fiziki, Vol. 73, No. 7, 2001, pp. 364–368.

Doppler–Rabi Oscillations of a Two-Level Atom Moving in a Cavity

A. V. Kozlovskiĭ

Lebedev Physical Institute, Russian Academy of Sciences, Leninskiĭ pr. 53, Moscow, 117924 Russia

e-mail: kozlovsk@sci.lebedev.ru

Received November 13, 2000; in final form, February 9, 2001

The interaction with a quantum mode of a high-Q cavity is considered for a two-level atom uniformly moving along the classical trajectory. The method of dressed states is employed to deduce the recursion relation for the probability of atomic transition with photon emission. It is shown that the dependence of the transition probability on the position of a moving atom in the cavity and the magnitude of this probability are qualitatively influenced by the ratio between the Doppler shift of transition frequency and the Rabi frequency of atom–field system. © *2001 MAIK "Nauka/Interperiodica".*

PACS numbers: 32.80.-t; 42.50.Ct

The Hamiltonian of a system consisting of a two-level atom moving along the classical trajectory and a single standing-wave mode of quantized electromagnetic field in a cavity [1] can be written in the form

$$\begin{aligned} H(t) &= \hbar\omega_C a^+ a + \frac{\hbar\omega_A}{2}\sigma^z + \hbar g(t)B \\ &= \hbar(C_1 + C_2(t)), \end{aligned} \tag{1}$$

where the operator of atom–field interaction in the rotary-wave approximation

$$B = a^+\sigma^- + \sigma^+ a$$

is written through the operators $\sigma^- = |\downarrow\rangle\langle\uparrow|$ and $\sigma^+ = |\uparrow\rangle\langle\downarrow|$ of transition between the upper $|\uparrow\rangle$ and lower $|\downarrow\rangle$ atomic states. The inversion operator is written as $\sigma^z|\uparrow\rangle\langle\uparrow| - |\downarrow\rangle\langle\downarrow|$, where $a^+(a)$ is the field creation (annihilation) operator.

The coupling constant for an atom moving along the trajectory $x(t)$ in a field has the form [2–5]

$$g(t) = g_0\cos(k_C x(t)), \quad g_0 = d\sqrt{\frac{2\pi\omega_A}{\hbar V}}, \tag{2}$$

where $k_C = \omega_C/c$ is the cavity mode wavevector, d is the dipole transition moment of a two-level atom, and V is the cavity volume. For a uniform motion of atomic center of mass with velocity v (the case considered in this work), the coupling constant is

$$\begin{aligned} g(t) &= g_0\cos(\Omega_D t + \Delta\Omega t), \quad \Omega_D = \frac{v}{c}\omega_A, \\ \Delta\Omega &= \frac{v}{c}\Delta\omega, \end{aligned} \tag{3}$$

where Ω_D is the atomic Doppler shift and $\Delta\omega = \omega_C - \omega_A$ is the detuning of the atomic frequency from the cavity frequency.

Hamiltonian (1) can be represented as a sum $\hbar(C_1 + C_2(t)$, where

$$C_1 = \omega_C\left(a^+ a + \frac{\sigma^z}{2}\right), \quad C_2(t) = g(t)B - \frac{\Delta\omega}{2}\sigma^z. \tag{4}$$

One can readily verify that the operators C_1 and $C_2(t)$ commute at any instant of time. Acting on the basis-set vectors $|n, j\rangle \equiv |n\rangle|j\rangle$ by operators C_1 and $C_2(t)$, where $|n\rangle$ is the Fock basis for the field states and $j = \uparrow$ and $\downarrow$, one can easily see that C_1 is diagonal in the $|n, j\rangle$ basis with eigenvalues $\omega_C(n \pm 1/2)$, while $C_2(t)$ is nondiagonal. By using the basis set of C_1 eigenvectors, one can determine the basis in which both C_1 and $C_2(t)$ are diagonal [1]; evidently, $H(t)$ is also diagonal in this case. This basis will be taken in the form of the following linear combinations of the $|n, j\rangle$ elements:

$$\begin{aligned} |+, n\rangle_t &= \cos\theta_n(t)|n+1, \downarrow\rangle + \sin\theta_n(t)|n, \uparrow\rangle, \\ |-, n\rangle_t &= -\sin\theta_n(t)|n+1, \downarrow\rangle + \cos\theta_n(t)|n, \uparrow\rangle. \end{aligned} \tag{5}$$

If the cavity field is absent at zero time $t = 0$, then $n = 0$ and $|+, 0\rangle_t$, and $|-, 0\rangle_t$.

Acting on the elements of this dressed basis by the C_1 operator, one gets

$$C_1|\pm, n\rangle_t = \omega_C\left(n + \frac{1}{2}\right)|\pm, n\rangle_t; \tag{6}$$

i.e., the $|\pm, 0\rangle_t$ states are the degenerate eigenstates of this operator. Let us now act on $|\pm, 0\rangle_t$ by $C_2(t)$ and

require that $C_2(t)$ be diagonal in this basis; i.e.,

$$C_2(t)|\pm, n\rangle_t = \Omega^{(R)}_{\pm, n}(t)|\pm, n\rangle_t; \tag{7}$$

one then has from Eq. (5) for the Rabi frequency

$$\Omega^{(R)}_{+,n}(t) = -\Omega^{(R)}_{-,n}(t) = \sqrt{\left(\frac{\Delta\omega}{2}\right)^2 + g^2(t)(n+1)},$$
$$\theta_n(t) = \frac{1}{2}\arctan\left(\frac{2g(t)}{\Delta\omega}\sqrt{n+1}\right). \tag{8}$$

In the basis of dressed states diagonalizing the Hamiltonian $H(t)$, one has

$$H(t)|\pm, n\rangle_t = \left(\frac{\hbar\omega_C}{2} + \hbar\Omega^{(R)}_{\pm, n}(t)\right)|\pm, n\rangle_t$$
$$\equiv \hbar\Omega_{\pm, n}(t)|\pm, n\rangle_t. \tag{9}$$

Making use of Eq. (5) and the fact that the dressed basis is orthonormalized, one finds for the relation between the $|\pm, n\rangle_t$ and $|n, j\rangle$ sets at a fixed instant of time

$$|n+1, \downarrow\rangle = \cos\theta_n(t)|+, n\rangle_t - \sin\theta_n(t)|-, n\rangle_t,$$
$$|n, \uparrow\rangle = \sin\theta_n(t)|+, n\rangle_t + \cos\theta_n(t)|-, n\rangle_t. \tag{10}$$

The elements of the parametrically time-dependent basis of dressed states are not orthonormalized for different instants of time, and this should be taken into account in the subsequent calculations. The relations between the elements of the dressed basis for different instants of time are ($\forall t_1 \neq t_2$)

$$|+, n\rangle_{t_1} = \cos(\theta_n(t_2) - \theta_n(t_1))|+, n\rangle_{t_2}$$
$$- \sin(\theta_n(t_2) - \theta_n(t_1))|-, n\rangle_{t_2},$$
$$|-, n\rangle_{t_1} = \sin(\theta_n(t_2) - \theta_n(t_1))|+, n\rangle_{t_2}$$
$$+ \cos(\theta_n(t_2) - \theta_n(t_1))|-, n\rangle_{t_2}. \tag{11}$$

In the Schrödinger representation, the time evolution of an atom interacting with field is described by the propagator (evolution operator) $U(t, t_0)$ in such a way that the state vector at time t has the form

$$|\psi(t)\rangle = U(t, t_0)|\psi(t_0)\rangle. \tag{12}$$

Let us partition a finite time interval $[t_0, t]$ into a large number $M \gg 1$ of small subintervals Δt and assume that the time dependence of the total Hamiltonian can be ignored within each of these subintervals. Then the time evolution of the system is described by the propagator

$$|\psi(t)\rangle = e^{-\frac{i}{\hbar}H(t_M)\Delta t} e^{-\frac{i}{\hbar}H(t_{M-1})\Delta t} \ldots e^{-\frac{i}{\hbar}H(t_1)\Delta t}|\psi(t_0)\rangle,$$
$$\Delta t = \frac{t}{M}. \tag{13}$$

In what follows, the atom is assumed to be in the excited state at the initial time $t_0 = 0$, while the field is assumed to be in the vacuum state; i.e., $|\psi(t_0 = 0)\rangle = |0, \uparrow\rangle$.

By using Eqs. (12), (13), and (8) and employing Eqs. (9) and (10), one arrives at the following recursion relation for the state of the system at the final instant of time:

$$|\psi(t = t_M)\rangle = A_{+, M}|+, 0\rangle_{t = t_M} + A_{-, M}|-, 0\rangle_{t = t_M}, \tag{14}$$

where the $A_{\pm, M}$ quantities are evaluated using the recursion relations

$$A_{+, t_j} = e^{-i\Omega_{+, n}(t_j)\Delta t}(\cos(\Delta\theta_{0, j})A_{+, t_{j-1}}$$
$$+ \sin(\Delta\theta_{0, j})A_{-, t_{j-1}}),$$
$$A_{-, t_j} = e^{-i\Omega_{-, n}(t_j)\Delta t}(-\sin(\Delta\theta_{0, j})A_{+, t_{j-1}} \tag{15}$$
$$+ \cos(\Delta\theta_{0, j})A_{-, t_{j-1}}),$$
$$\Delta\theta_{0, j} \equiv \theta_0(t_j) - \theta_0(t_{j-1})$$

for any $0 < j \leq M$ and

$$A_{+, t_1} = \sin(\theta_0(\Delta t))e^{-i\Omega_{+, 0}(\Delta t)\Delta t},$$
$$A_{-, t_1} = \cos(\theta_0(\Delta t))e^{-i\Omega_{-, 0}(\Delta t)\Delta t}. \tag{16}$$

The probability of atomic transition to the lower state with emission of a photon into the cavity mode is then given by

$$P(t) = |\langle 1\downarrow|\psi(t)\rangle|^2 = \langle a^+(t)a(t)\rangle$$
$$= |\cos(\theta_0(t))A_{+, t} - \sin(\theta_0(t))A_{-, t}|^2. \tag{17}$$

One can easily see that, when using Eq. (17) in calculations, the replacement $\Omega_{+, 0}(t) \longrightarrow \pm\Omega^{(R)}_0(t)$ in Eqs. (15) and (16) will not change the result.

The assumption about classical character of atomic motion in a cavity sets certain limits on the atomic velocity and mass. In the further calculations with the use of formulas derived above, it will be assumed that the de Broglie wavelength $\lambda = h/mv$ (m is atomic mass) is much shorter than the wavelength $\lambda = 2\pi/k_C$ of the cavity mode; i.e., the atomic mass and/or the velocity of its center of mass is large. The assumption about the uniformity of atomic movement, i.e., the neglect of photon-emission recoil momentum, also implies that the coupling energy $\hbar g_0$ is small in comparison with the kinetic energy $mv^2/2$ of the atomic center of mass. A detailed analysis of the applicability of the classical approximation to the problem of interaction of an atom moving in a cavity is given, e.g., in [3].

It is also assumed that the cavity Q factor is sufficiently large for the time of interaction between atom and field to be shorter than γ^{-1}, where γ is field dissipation rate due to mirror loss. These assumptions corre-

spond to a micromaser configuration in [6–12], where the Jaynes–Cummings model was used.

As is well known, the probability of photon emission by a quiescent atom in an electromagnetic vacuum oscillates in time with vacuum Rabi frequency

$$P(t) = \frac{4g_0^2}{\Delta\omega^2 + 4g_0^2}\sin^2(\Omega_0^{(R)}t).$$

If the atomic frequency is detuned from the frequency of cavity mode by $\Delta\omega \ll \Delta g_0$, then the transition probability (in our case it is equal to the mean number of photons in the cavity) is given, according to [2], by the simple expressions

$$P(t) = \langle a^+(t)a(t)\rangle = \sin^2\left[\frac{g_0}{\Omega_D}\sin(\Omega_D t)\right]. \quad (18)$$

Calculations by Eqs. (16) and (17) show that the time behavior of transition probability for a moving atom strongly depends on the ratio between the velocity of center of mass, coupling constant, and frequency detuning. Depending on the ratio between these quantities, $\xi = \Omega_R/\Omega_D$, and $\Omega_R = \sqrt{g_0^2 + (\Delta\omega/2)^2}$, the Rabi oscillations in the time dependence of emission probability may be absent. At $\xi \ll 1$, the probability of photon emission by the atom and its escape from the cavity in the lower state may be low even for large coupling constants and small detunings (Fig. 1). In this case, the oscillation frequency of transition probability corresponds to the $(1/\xi)$th harmonic of the Rabi frequency and the probability magnitude decreases as ξ^2. As follows from Eq. (18), the transition probability at $\xi \ll 1$ is equal to $g_0^2/\Omega_D^2\sin^2(\Omega_D t)$; i.e., the oscillation frequency is determined by the Doppler shift of atomic frequency.

The condition for the occurrence of Rabi-type probability oscillations is the Doppler resonance $\xi = 1$ (Fig. 2). According to Eq. (18), in this case $P \le \sin^2(1)$.

If $\xi > 1$, i.e., if the Doppler shift is smaller than the Rabi frequency, the maximum transition probability is unity, as for the atom at rest. One can see from Fig. 3a that the oscillations with Rabi frequency are absent for $\xi = 2$, but they are regained near the field antinodes with an increase in ξ (Figs. 3b, 3c). As expected, the usual Rabi oscillations occur at $\xi \gg 1$, but, for a finite atomic velocity, only near the antinodes of cavity field.

At present, the theory of micromasers [6–9] appeals to the Jaynes–Cummings model for a quiescent atom. A comparison with the experiment shows [8–13] that the predictions of this theory do not necessarily agree with the experiment. For example, the photon statistics of maser radiation was studied experimentally in [12] for the atomic transition frequency $\omega_A = 21.5$ GHz, cavity length $L = 2.4$ cm, coupling constant $g_0 = 10$ kHz, and time $L/v = 50$ μs of atom flight through the cavity, and it was found that there is a qualitative discordance

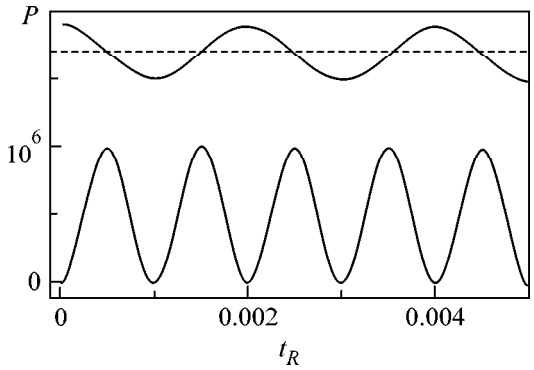

Fig. 1. Probability P of atomic transition from the excited state to the lower state with photon emission vs. dimensionless time $t_R = \Omega_R t/\pi$ ($\Omega_R = \sqrt{g_0^2 + (\Delta\omega/2)^2}$) for $\Delta\omega \ll g_0$ and $\xi = \Omega_R/\Omega_D = 10^{-3}$. The $\cos(k_C x(t_R))$ function is shown in the upper part of the figure.

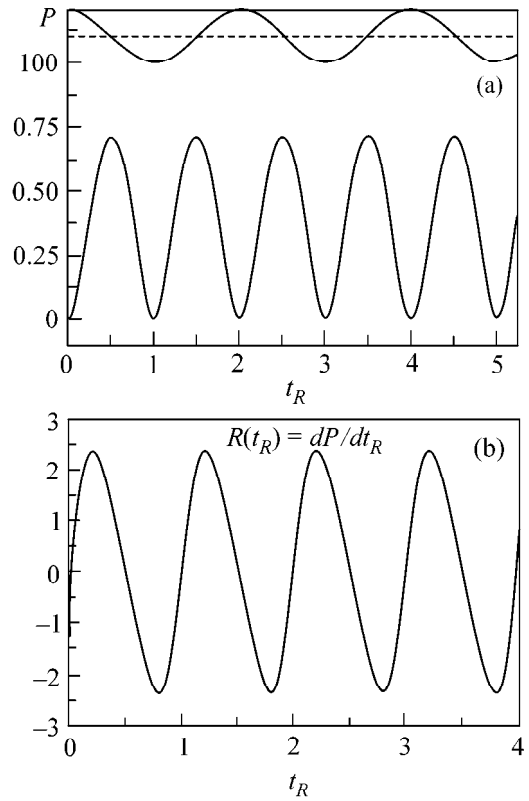

Fig. 2. (a) The same as in Fig. 1 for the regime of Doppler–Rabi resonance $\xi = \Omega_R/\Omega_D = 1$. (b) Transition rate $R(t_R) = dP(t_R)/dt_R$.

between the theory and experiment. At the same time, the agreement with theory is achieved after changing the micromaser parameters in such a way that the time of interaction between the atom and field is reduced to $L/v = 35$ μs and the coupling constant increases to $g_0 \approx 44$ kHz. Calculation by Eq. (17), which takes into

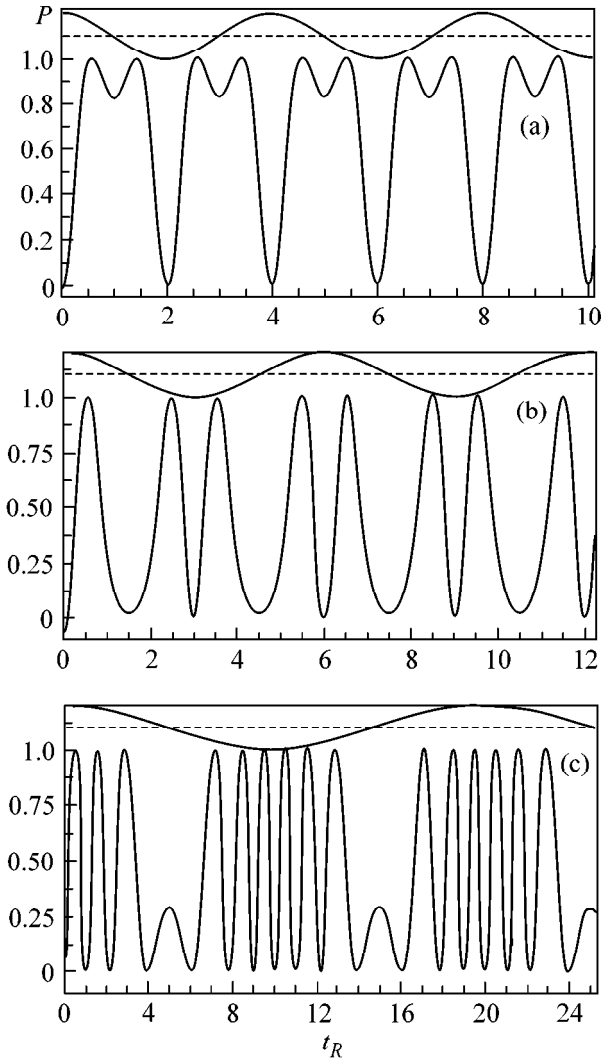

Fig. 3. The same as in Fig. 1 for ξ = (a) 2, (b) 3, and (c) 10.

account the influence of atomic motion on the interaction of the atom with the field, shows that the system state in the latter case is close to the Doppler–Rabi resonance ($\xi \approx 1$) and the transition probability changes following the law resembling the usual Rabi oscillations (Fig. 2) of an atom at rest, whereas, under the other experimental conditions, the ratio between the Rabi frequency and the Doppler shift is appreciably smaller, $\xi \approx 0.3$, so that the situation is drastically different from the resonance ($\xi = 1$) and corresponds to the regime of energy exchange between the atom and field similar to that shown in Fig. 1 for $\xi \ll 1$.

The calculations also show that the effects associated with the atomic motion in a cavity must be allowed for in the theory of micromasers for both a flat-mirror cavity and a confocal cavity with spherical mirrors [14, 15], as well as for micromaser schemes where the flow of excited atoms is passed through the cavity [16].

REFERENCES

1. E. T. Jaynes and F. W. Cummings, Proc. IEEE **51**, 89 (1963).
2. P. Meystre, Opt. Commun. **90**, 41 (1992).
3. W. Ren, J. D. Cresser, and H. J. Carmichael, Phys. Rev. A **46**, 7162 (1992).
4. M. Wilkens and P. Meystre, Opt. Commun. **94**, 66 (1992).
5. W. Ren and H. J. Carmichael, Phys. Rev. A **51**, 752 (1995).
6. P. Filopowicz, J. Javanainen, and P. Meystre, Phys. Rev. A **34**, 3077 (1986).
7. L. A. Lugiato, M. O. Scully, and H. Walther, Phys. Rev. A **36**, 740 (1987).
8. D. Meschede, W. Walther, and G. Müller, Phys. Rev. Lett. **54**, 551 (1985).
9. H.-J. Briegel, B.-G. Englert, and M. O. Scully, Phys. Rev. A **54**, 3603 (1996).
10. M. O. Scully, G. M. Meyer, and H. Walther, Phys. Rev. Lett. **76**, 4144 (1996).
11. G. Rempe, H. Walther, and N. Klein, Phys. Rev. Lett. **58**, 353 (1987).
12. G. Rempe, F. Schmidt-Kaler, and H. Walther, Phys. Rev. Lett. **64**, 2783 (1990).
13. M. Weidinger, B. T. H. Varcoe, R. Heerlein, and H. Walther, Phys. Rev. Lett. **82**, 3795 (1999).
14. M. Brune, F. Schmidt-Kaler, A. Maali, *et al.*, Phys. Rev. Lett. **76**, 1800 (1996).
15. M. Brune, P. Nussenzveig, F. Schmidt-Kaler, *et al.*, Phys. Rev. Lett. **72**, 3339 (1994).
16. G. T. Forster, S. L. Mielke, and L. A. Orozco, Phys. Rev. A **61**, 053821 (2000).

Translated by V. Sakun

JETP Letters, Vol. 73, No. 7, 2001, pp. 327–330. Translated from Pis'ma v Zhurnal Éksperimental'noĭ i Teoreticheskoĭ Fiziki, Vol. 73, No. 7, 2001, pp. 369–372.

Critical Dynamics of Homogeneous Magnetization above T_c in $Nd_{0.77}Ba_{0.23}MnO_3$ Single Crystals

I. D. Luzyanin, V. P. Khavronin, V. A. Ryzhov, I. I. Larionov, and A. V. Lazuta

Konstantinov Institute of Nuclear Physics, St. Petersburg, Russian Academy of Sciences, Gatchina, Leningrad region, 188300 Russia

e-mail: luzyanin@mail.pnpi.spb.ru

Received February 15, 2001

The behavior of the linear and nonlinear dynamic susceptibilities of a $Nd_{0.77}Ba_{0.23}MnO_3$ single crystal is studied with the aim to verify whether sealing theory is applicable for describing the critical phenomena in manganites with cubic symmetry. The experimental results obtained for the exchange temperature region ($4\pi\chi \ll 1$) agree well with the theoretical predictions, whereas the appearance of magnetically ordered formations in the paramagnetic phase is presumably due to the orbital ordering. *© 2001 MAIK "Nauka/Interperiodica".*

PACS numbers: 75.40.Gb; 75.50.Cc

The critical dynamics of homogeneous magnetization in simple cubic ferromagnets has been rather well studied both theoretically and experimentally. The results of these studies are in good agreement with each other. However, the applicability of sealing theory to the second-order magnetic phase transitions in complex non-Heisenberg magnets such as manganites is questionable. At the same time, to our knowledge, no special experimental studies of the critical phenomena in manganites have been carried out so far.

It is evident that the study of critical dynamics of complex magnets should begin with the simplest systems. For this purpose, we studied the critical behavior of the linear and nonlinear susceptibilities in the paramagnetic phase of $Nd_{0.77}Ba_{0.23}MnO_3$ manganite characterized by cubic symmetry. Special attention was given to the study of the nonlinear response to an ac magnetic field. Below, we will show that higher harmonics are much more singular than the linear susceptibility, making it possible to test the applicability of sealing theory more reliably. A good agreement between the experimental and theoretical results was obtained for the temperature range corresponding to the static susceptibility $4\pi\chi_0 < 1$, whereas the phenomena observed at lower temperatures were presumably due to orbital ordering.

The dynamics of homogeneous magnetization is determined by the interactions not conserving the total spin of the system. In the case of cubic ferromagnets, the main interaction of this kind is, as a rule, the dipolar interaction, which is the only one that is taken into account in most studies of the dynamics of critical fluctuations of homogeneous magnetization. In this case, according to the existing concepts, the decay of fluctuations represents a relaxation process characterized by the critical damping coefficient Γ. In the theory of dynamic sealing, two temperature regions are distinguished depending on the relative role of the dipolar forces: one region corresponds to the static susceptibility $4\pi\chi_0 \ll 1$ (exchange region), and the other corresponds to $4\pi\chi_0 \gg 1$ (dipolar region). In the exchange region, the characteristic energy of critical fluctuations is $\Omega_e \approx kT_c\tau^{5/3}$, and the inverse relaxation time Γ_H of homogeneous magnetization is determined by the dipolar forces and grows as the temperature approaches T_c according to the law $\Gamma_H \propto \tau^{-1}$ [1], where $\tau = (T - T_c)/T_c$ is the relative temperature.

In the dipolar region, the characteristic energy of critical fluctuations and the inverse relaxation time Γ_0 of homogeneous magnetization are of the same order of magnitude. In the theory, two versions are considered for the behavior of Γ_0 in this region: $\Gamma_0 \propto \tau^{4/3}$ (normal or "soft" version) [2] and $\Gamma_0 \propto \tau^{2/3}$ ("stiff" version) [3].

Let us now consider the behavior of the linear and nonlinear susceptibilities in a cubic ferromagnet at a temperature above T_c in the absence of a constant magnetic field. Let a sample be placed in an alternating magnetic field $h = h_0\cos\omega t$ at $T > T_c$. Then, for a sufficiently weak field, the expression for the magnetization can be represented as a series

$$m(h) = \chi_0(\omega)h + \chi_3(\omega)h_0^3 + \chi_5(\omega)h_0^5 + \ldots . \quad (1)$$

Here, $\chi_0(\omega)$ is the longitudinal linear dynamic susceptibility, and $\chi_{2n+1}(\omega)$ ($n = 1, 2, 3, \ldots$) are the nonlinear dynamic susceptibilities. The corresponding expressions for the static case can be found in [4]. It should be noted that the nonlinear dynamic phenomena that occur in the critical region of a ferromagnet are poorly investigated both theoretically and experimentally. In fact, there are only two publications, one of which [5] is devoted to the theoretical study of some limiting cases

and the other [6] considers in detail the second harmonic of magnetization. Below, we will use some results obtained in [5] for low frequencies and lower harmonics ($n\omega \sim \omega$).

It should be noted that expansion (1) is valid only for weak magnetic fields [4]:

$$g\mu h_0 \ll kT_c\tau^{5/2}. \quad (2)$$

Here, the conventional notations are used for the g factor and the Bohr magneton μ. Evidently, this rather strict condition must be satisfied if we want to compare the experimental and theoretical results. For such a comparison, it is also necessary that the frequency of the alternating magnetic field be much smaller than the characteristic energy of critical fluctuations. For the exchange region, this condition has the form

$$\omega \ll \Gamma_H \ll \Omega_e, \quad (3)$$

and in the dipolal region it can be represented as

$$\omega \ll \Gamma_0. \quad (4)$$

In the case of low frequencies in the absence of a constant magnetic field, sealing theory yields the following expression for the odd harmonics [5]:

$$m_{2n+1}(t) = 2M(\tau)\left(\frac{g\mu h_e S}{2\Omega_e}\right)^{2n+1} \times \frac{r_{2n+1}(0)}{1+4\pi\chi_0 N}\cos(2n+1)\omega t, \quad (5)$$

$$h_e = h_0/(1+4\pi\chi'(\omega)N).$$

Here, $M(\tau) = M_0\tau^\beta$, where $\beta \approx 1/3$ and M_0 is a quantity on the order of the spontaneous magnetic moment at $T = 0$; N is the demagnetization factor; S is the atomic spin; and r_{2n+1} is the τ-independent dimensionless amplitude. It follows from this approximation that

$$\chi_0 \propto \tau^{-4/3},\ \chi_3 \propto \tau^{-14/3},\ \chi_5 \propto \tau^{-24/3}, \ldots. \quad (6)$$

In the presence of a constant magnetic field, the response contains, apart from the odd harmonics, even harmonics of magnetization oscillations at frequencies $\omega_{2n} = 2n\omega$. When the alternating and constant magnetic fields are collinear, the expression for the even harmonics in the case of low frequencies ($\omega < g\mu H$) and a weak field ($g\mu h_0$, $g\mu H < \Omega_e$) has the form [5]

$$m_{2n}(t) = 2M(\tau)\left(\frac{g\mu h_e S}{\Omega_e}\right)^{2n} \times \frac{g\mu HS}{2\Omega_e}\frac{(2n+1)r_{2n}(0)}{1+4\pi\chi_0 N}\cos 2n\omega t. \quad (7)$$

One can see from Eqs. (5) and (7) that both odd and even harmonics are singular at the Curie point in the limit $\omega \longrightarrow 0$, $h \longrightarrow 0$. The characteristic feature of Eqs. (5) and (7) is that the dependence on the sample shape, i.e., on N, is contained in the expression for the replacement of the external field by an internal field and in the additional factor $(1 + 4\pi\chi_0 N)^{-1}$. All other factors appearing in these expressions are independent of N. Such a relation of m_{2n+1} and m_{2n} with N occurs regardless of the specific type of theory that describes the magnetic system. This result immediately follows from the method used in deriving Eqs. (5) and (7), which was described in [5]. As one can see from Eqs. (5) and (7), for $N \neq 0$ and $4\pi\chi > 1$ the higher harmonics decrease faster with increasing n because of the demagnetization.

The behavior of the linear and nonlinear dynamic susceptibilities was studied for a $Nd_{0.77}Ba_{0.23}MnO_3$ single-crystal sample with dimensions $2 \times 2 \times 3$ mm (m = 54.5 mg). According to the X-ray diffraction data, it was a single-phase sample with cubic structure both above and below T_c (a = 3.899 Å at T = 300 K [6]).

The measurements of the real (χ') and imaginary (χ'') parts of the linear susceptibility and the third harmonic amplitude were performed in the frequency range 1–100 kHz. The data for the real ($\mathrm{Re}M_2$) and imaginary ($\mathrm{Im}M_2$) components of the second harmonic of magnetization in the parallel constant and alternating magnetic fields were obtained as functions of the constant field H at frequency f = 15.7 MHz.

In studying the critical phenomena, the most important (and difficult) problem is to determine the temperature of phase transition. Theoretically, the correlation radius at T_c is infinite; i.e., all quantities related to it are singular at this point. However, because of the finiteness of the magnetic field, the temperature instability, etc., the singularity is not observed in the experiment. Hence, one can expect that the temperature dependences of the quantities physically singular at T_c will exhibit maxima at some temperature, which can be called the experimental Curie point. However, this is not always the case. For example, in the temperature dependence of the real part of susceptibility, a maximum corresponding to the singularity at T_c is usually not observed (except for the singularity at $T > T_c$ that is caused by the transition from the $\omega \ll \Gamma_0$ regime to the $\omega \gg \Gamma_0$ regime, see [7]), which is presumably due to the formation of the domain structure immediately below T_c. Therefore, it is necessary to find other approaches for determining the phase transition temperature. In this study, as in our previous experiments [8, 9], the Curie point was determined from the position of a maximum observed in the temperature dependence of the third harmonic amplitude. The aforementioned experiments [8, 9] were performed for $CdCr_2Se_4$ and $CdCr_2S_4$ single crystals and showed that the Curie point determined in this way coincided with its value obtained from the temperature behavior of the critical damping coefficient Γ_0, which testified to the validity of the general scaling considerations in choosing the value of T_c.

Let us now turn to the measured temperature dependences of the linear and nonlinear susceptibilities. In connection with the main problem considered in this paper, we will concentrate on the data for the exchange region ($4\pi\chi_0 < 1$). For the case $4\pi\chi_0 > 1$ (dipolar region), a comparison of the experimental results with the theory seems to be impossible because of the demagnetization effects caused by the sample shape.

Figure 1 shows the temperature dependence of the third-order susceptibility whose maximum corresponding to the Curie point [T_c = 124.1(0.03) K] is indicated by the arrow; the inset shows the dependence of $4\pi\chi_3$ on τ. This dependence was found to obey the power law with exponent 5.4(0.2), which does not contradict sealing theory [see Eq. (5)]. The small interval of τ within which the dependence of χ_3 on τ obeys the scaling law is determined, on the one hand, by the smallness of the third harmonic amplitude away from T_c and, on the other hand, by the stronger effect of the demagnetization factor on the higher harmonics, as compared to the linear susceptibility. Note that over the whole temperature range of measurements, the amplitude of the third harmonic was proportional to h_0^3; i.e., the important condition that the field be weak was satisfied. In addition, as one can see from Fig. 2, the dependence $\chi''(T)$ also has a maximum at $T \approx 124.1$ K, which is presumably due to the effect of the critical slowing down. One can see from this dependence that the imaginary part of linear susceptibility is extremely small in the exchange region ($4\pi\chi_0 < 1$), and, therefore, one can assume that $\chi' = \chi_0$ in this region.

From the dependence $\chi'(T)$ shown in Fig. 2 and from the value T_c = 124.1 K, it was found that γ = 1.34(0.01) for a τ interval larger than an order of magnitude (inset in Fig. 2). At the same time, the best fit of the experimental data to the law $\chi \propto \tau^{-\gamma}$ ($\gamma = 4/3$) gives the value T_c = 124.15 K, which practically coincides with the high-temperature maximum in the $4\pi\chi_3(T)$ dependence (Fig. 1). A departure from the scaling law is observed at $\tau \approx 0.1$ and can also be attributed to the effect of the demagnetization factor. As one can see from Fig. 2, the transition from the exchange region to the dipolar one ($4\pi\chi \approx 1$) occurs at $\tau \le 1.10^{-2}$ ($T \le 127$ K).

Let us now turn to the results of the experiments with the second harmonic; specifically, we consider the temperature dependence of its real part (Fig. 3). In the temperature range 147 < T < 210 K (0.2 < τ < 0.9), the quantity $\mathrm{Re}M_2$ is proportional to H and h_0^2, indicating that the weak-field condition is fulfilled. At the same time, the EPR measurements suggested that the ratio $\omega/\Gamma \sim 10^{-2}$. This allows us to assume that we deal with the quasi-static case. One can see from the inset in Fig. 3 that the dependence $\mathrm{Re}M_2(\tau)$ has the form of a power law with exponent 5.2(0.2), in fairly good agreement with the expected value [see Eq. (7)].

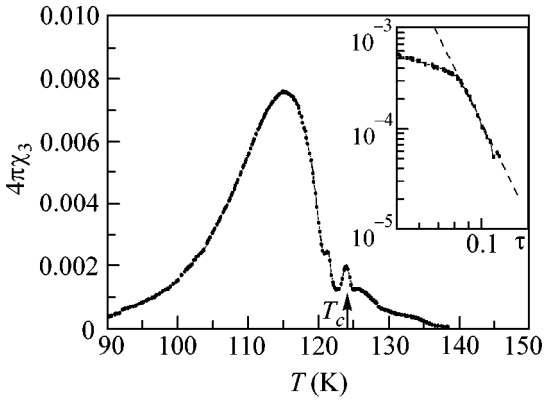

Fig. 1. Temperature dependence of the susceptibility $4\pi\chi_3$. The inset shows the $4\pi\chi_3(\tau)$ dependence. H = 0 and h_0 = 1 Oe.

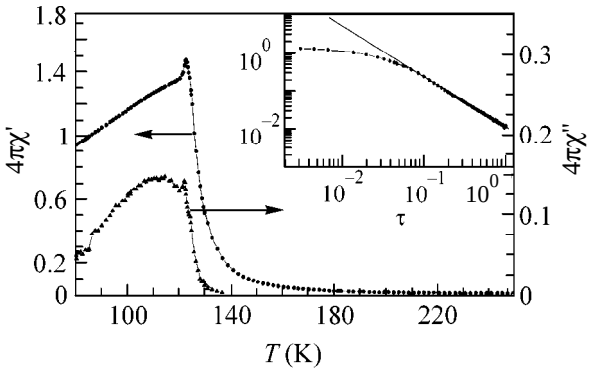

Fig. 2. Temperature dependence of the linear susceptibility. The inset shows the dependence of its real part on the relative temperature. H = 0 and h_0 = 1 Oe.

The departure of the temperature dependences of χ', χ_3, and $\mathrm{Re}M_2$ from the power law at $4\pi\chi_0 \approx 1$ is caused by both the demagnetization effects and the appearance of magnetically ordered formations in the crystal. At T = 146.7 K ($\tau \approx 0.2$), the imaginary part $\mathrm{Im}M_2$ of the second harmonic is characterized by a magnetic hysteresis, and the real part $\mathrm{Re}M_2(H)$ is characterized by two regions of linear dependence with different slopes. The hysteresis of the second harmonic in a very weak field $H \sim 5$ Oe was observed at $\tau \le 0.08$ and at low frequencies. Thus, one can assume that the magnetically ordered formations appear above T_c. Note that the anomalous phenomena partially cover the τ region which corresponds to the scaling-type dependence $\chi_0(\tau)$, but the value of γ remains unaffected. This can presumably be explained by the smallness of the volume occupied by the ordered formations. Nevertheless, the fact that the exponents in the $\chi_3(\tau)$ and $\mathrm{Re}M_2(\tau)$ dependences are somewhat higher than those predicted by the theory can be attributed to this phenomenon. Since the crystal under study possesses cubic symmetry, Yahn–Teller distortions, if any, are extremely weak

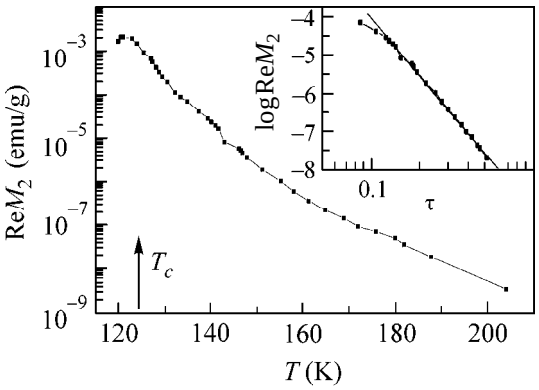

Fig. 3. Temperature dependence of the real part of the second harmonic of magnetization. The inset shows the Re$M_2(\tau)$ dependence. $H \approx 200$ Oe.

and cannot be the main mechanism responsible for the formation of the new magnetic phase above T_c. One of the possible mechanisms of this phenomenon is the orbital ordering of manganese lattices [10]. However, it should be noted that in the earlier studies of the critical behavior of homogeneous magnetization in Heisenberg ferromagnets ($CdCr_2S_4$ and $CdCr_2Se_4$) [8, 9], we also revealed two temperature regions near T_c, namely, the scaling region and the anomalous one, which differed in the character of critical phenomena. In the scaling region, the behavior of the linear susceptibility and the higher harmonics observed in the experiment agrees well with the predictions of scaling theory. In the anomalous temperature region immediately adjoining T_c ($\tau \leq 10^{-2}$), the dynamic susceptibility exhibits a "glasslike" behavior (with $\chi' \propto \log\omega$ and χ'' being practically independent of ω), the field hysteresis of the second harmonic is observed, etc.

Thus, the results of our experiments show that the character of critical phenomena in the paramagnetic phase of $Nd_{0.77}Ba_{0.23}MnO_3$ is similar to that observed in cubic Heisenberg ferromagnets above T_c.

We are grateful to I.O. Troyanchuk and D.D. Khalyavin (Institute of Solid State and Semiconductor Physics, National Academy of Sciences of Belarus) for the fruitful cooperation under a joint project of the Belarussian and Russian Foundations for Basic Research; to Yu.P. Chernenkov for the structure studies; to S.M. Dunaevskii for useful discussions; and to I.A. Kiselev, I.R. Metskhvarishvili, and Ya.V. Gresheva for their participation in the experiment. This work was supported by the Russian Foundation for Basic Research, project nos. 00-02-81205-Bel2000a and 00-02-16729.

REFERENCES

1. D. L. Huber, J. Phys. Chem. Solids **32**, 2145 (1971).
2. S. V. Maleev, Zh. Éksp. Teor. Fiz. **66**, 1809 (1974) [Sov. Phys. JETP **39**, 889 (1974)].
3. G. B. Teĭtel'baum, Pis'ma Zh. Éksp. Teor. Fiz. **21**, 339 (1975) [JETP Lett. **21**, 154 (1975)].
4. A. Z. Patashinskiĭ and V. L. Pokrovskiĭ, *Fluctuation Theory of Phase Transitions* (Nauka, Moscow, 1982, 2nd ed.; Pergamon, Oxford, 1979).
5. S. V. Maleev, Phys. Rev. A **8**, 323 (1987).
6. A. V. Lazuta, I. I. Larionov, and V. A. Ryzhov, Zh. Éksp. Teor. Fiz. **100**, 1964 (1991) [Sov. Phys. JETP **73**, 1086 (1991)].
7. I. O. Troyanchuk, D. D. Khalyavin, S. V. Trukhanov, and H. Szymczak, J. Phys.: Condens. Matter **11**, 8707 (1999).
8. I. D. Luzyanin and V. P. Khavronin, Zh. Éksp. Teor. Fiz. **85**, 1029 (1983) [Sov. Phys. JETP **58**, 599 (1983)].
9. I. D. Luzyanin and V. P. Khavronin, Zh. Éksp. Teor. Fiz. **87**, 2129 (1984) [Sov. Phys. JETP **60**, 1229 (1984)].
10. S. Okamoto, S. Ishihara, and S. Maekawa, Phys. Rev. B **61**, 451 (2000).

Translated by E. Golyamina

JETP Letters, Vol. 73, No. 7, 2001, pp. 331–335. Translated from Pis'ma v Zhurnal Éksperimental'noĭ i Teoreticheskoĭ Fiziki, Vol. 73, No. 7, 2001, pp. 373–377.

On the Possibility of Superconductivity in a MgB_2 Compound

R. O. Zaĭtsev

Russian Research Centre Kurchatov Institute, pl. Kurchatova 1, Moscow, 123182 Russia

e-mail: zaitsev@mbslab.kiae.ru

Received February 16, 2001

A concept of strong interaction in a single unit cell is used to predict Cooper instability in a system with hopping between main-group cations and anions. A phase diagram of ferromagnetic ordering is constructed for different degrees of $(n_p)p^6$- and $(n_s)s^2$-shell filling in main-group elements. © *2001 MAIK "Nauka/Interperiodica".*

PACS numbers: 74.20.De; 74.70.Ad; 74.25.Dw

The discovery of superconductivity in MgB_2 at temperatures as high as 40 K [1] provides evidence for the presence of a substantial contribution from the nonphonon superconducting mechanism. The mean number n_s of magnesium *s* electrons and the mean number n_p of boron *p* electrons in the titled compound satisfy the electroneutrality relation

$$2n_p + n_s = 4, \quad 0 < n_s < 2, \quad 1 < n_p < 2. \tag{1}$$

Therefore, one should find out how the four-electron boron $p_{x,y}$ shell and two-electron magnesium $3s^2$ shell are filled in the hexagonal unit cell of MgB_2.[1]

The Hubbard energies of magnesium (6.88 eV) and boron (8.43 eV) are the largest energetic parameters of the problem. For this reason, the approach used in this work is based on the generalized Hubbard model with infinitely strong repulsion for both *s* and *p* electrons.

The trigonal lattice of magnesium cations is situated between the layers of boron anions which form a honeycomb lattice (see [2] and Fig. 1).

With an eye to the computer computations, it is convenient to express the matrix elements through the real wave functions. The corresponding matrix of transitions from the *a*-boron to the *b*-boron atoms has the following form:

$$\hat{A} = \begin{pmatrix} \sum_k e^{+ip_k}\cos^2(\gamma_k); & \sum_k \cos(\gamma_k)\sin(\gamma_k)e^{+ip_k} \\ \sum_k \cos(\gamma_k)\sin(\gamma_k)^{+ip_k}; & \sum_k \sin^2(\gamma_k)e^{+ip_k} \end{pmatrix}. \tag{2}$$

[1] The p_z-shell filling is disregarded because the distance between the boron layers (3.52 Å) is larger than between the carbon layers in graphite (3.4 Å).

The notations used in this expression are appropriate to the plane trigonal lattice:

$$p_0 = 0, \quad p_\pm = \pm\frac{p_x}{2} + \frac{\sqrt{3}p_y}{2}, \quad \gamma_0 = -\frac{\pi}{2}, \quad \gamma_+ = \frac{\pi}{6}, \quad \gamma_- = 5\frac{\pi}{6}. \tag{3}$$

The matrix of transitions from Mg to the *a*-boron atoms is

$$\hat{\tau}_a(\mathbf{p}) = -t\nu(p_z)e^{-ip_+}\left(\sum_k \cos(\alpha_k)e^{+ip_k}, \ \sum_k \sin(\alpha_k)e^{+ip_k}\right), \tag{4}$$

where $\nu(p_z) = 1 - e^{ip_z}$, $\alpha_0 = -\pi/2$, $\alpha_+ = \pi/6$, and $\alpha_- = 5\pi/6$. Likewise, one has for the transitions from Mg to the *b*-boron atoms

$$\hat{\tau}_b(\mathbf{p}) = -t\nu(p_z)e^{ip_-}\left(\sum_k \cos(\beta_k)e^{-ip_k}; \ \sum_k \sin(\beta_k)e^{-ip_k}\right), \tag{5}$$

where $\beta_0 = \pi/2$, $\beta_+ = -5\pi/6$, and $\beta_- = -\pi/6$.

Substituting the values of α, β, and γ angles into the matrices, one gets the following expressions in terms of two independent quantities $W_\pm = \exp(ip_+) \pm \exp(ip_-)$:

$$\hat{A} = \begin{pmatrix} c^2W_+; & csW_- \\ csW_-; & 1 + s^2W_+ \end{pmatrix};$$

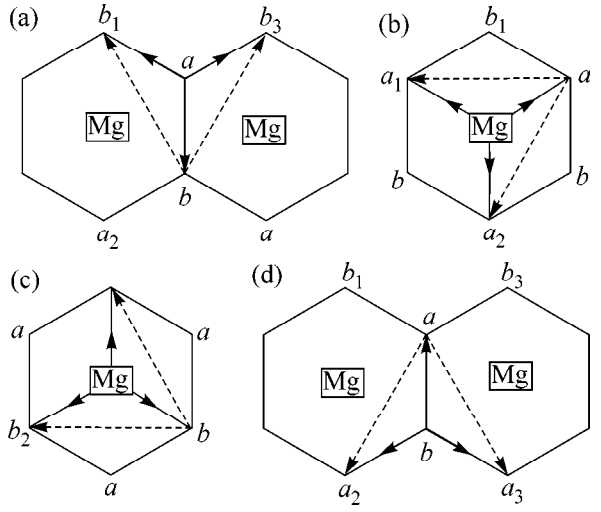

Fig. 1. Fragments of the AlB_2-type lattice. Solid and dashed arrows indicate the transition directions and the fundamental translation vectors, respectively.

$$\hat{B} = \begin{pmatrix} c^2 W_+^*; & csW_-^* \\ csW_-^*; & 1 + s^2 W_+^* \end{pmatrix}; \tag{6}$$

$$c = \frac{\sqrt{3}}{2}, \quad s = \frac{1}{2},$$

$$\begin{aligned} \hat{\tau}_a &= -t\nu(p_z)e^{-ip_+}(cW_-; \quad -1 + sW_+), \\ \hat{\tau}_b &= +t\nu(p_z)e^{ip_-}(cW_-^*; \quad -1 + sW_+^*). \end{aligned} \tag{7}$$

In the simplest one-loop (Hubbard I) approximation, the inverse Green's function matrix has the form

$$\hat{G}^{-1} = \begin{pmatrix} E_s; & -f_s\hat{\tau}_a; & -f_s\hat{\tau}_b \\ -g_p^2 f_p\hat{\tau}_a^+; & E_p\hat{I}; & -g_p^2 f_p\tau\hat{A} \\ -g_p^2 f_p\hat{\tau}_b^+; & -g_p^2 f_p\tau\hat{B}; & E_p\hat{I} \end{pmatrix}, \tag{8}$$

where $E_k = i\omega_n - \epsilon_k$. In Eq. (8), τ is the nearest-neighbor hopping integral for the honeycomb boron lattice. The end multipliers f_k are equal to the sum of occupation numbers for the initial and final states, and g_p^2 is the sum of squares of genealogical coefficients. Both are calculated for each of the integer intervals of mean occupation numbers (see [3, 4] and below).

Notice that the equation for the spectrum splits into first-degree and fifth-degree equations whose coefficients depend on three combinations each invariant about hexagonal transformations $p_+ \longrightarrow -p_- \longrightarrow (-p_+ + p_-) \longrightarrow p_+$:

$$S_k = \cos[kp_+] + \cos[kp_-] + \cos[k(-p_- + p_+)],$$
$$k = 1, 2.$$

The third invariant is expressed through the first two ones:

$$\begin{aligned} S_3 &= \cos[2p_+ - p_-] \\ &+ \cos[2p_- - p_+] + \cos[p_- + p_+], \\ S_3 &= S_1^2 - S_1 - \frac{1}{2}S_2 - \frac{3}{2}. \end{aligned} \tag{9}$$

The equation for the spectrum of excitations has the following general form:

$$\begin{aligned} \det = \left(E_p - \frac{3}{2}z\right)\left\{\left(E_p + \frac{3}{2}z\right)E_s\left[E_p^2 - z^2\left(\frac{3}{4} + \frac{1}{2}S_1\right)\right]\right. \\ \left. - 2w\left[E_p^2(3 - S_1) + E_p z(3 - S_3) + \frac{3}{4}z^2(S_1 - S_2)\right]\right\} = 0, \end{aligned} \tag{10}$$

where

$$z = \tau f_p g_p^2, \quad w = 4 f_s f_p g_p^2 t^2 \sin^2\left(\frac{p_z}{2}\right).$$

Hence, although the *p* subband splits off, the spectrum of excitations is still determined from a rather complex fourth-degree equation, and its calculation involves rather cumbersome mathematics. Because of this, the problem is simplified below in such a way that the spectrum coincides with its exact form at the Γ point. As regards the rest of the Brillouin zone, it is assumed that the spectrum depends only on a single invariant combination S_1, while determinant (10) of the inverse matrix is factorized as

$$\begin{aligned} \det = \left(E_p - \frac{3}{2}z\right)\left[E_p^2 - z^2\left(\frac{3}{4} + \frac{1}{2}S_1\right)\right] \\ \times\left[\left(E_p + \frac{3}{2}z\right)E_s - 2w(3 - S_1)\right]. \end{aligned} \tag{11}$$

In the absence of hybridization ($w = 0$), determinant (11) coincides with Eq. (10); hence, it is actually assumed that only the lowest localized *p* state with energy $-3z/2$ is hybridized.

Thus, there are one *s*–*d* hybridized, two nonhybridized, and one localized *p*-electron subbands.

Let us write the equations of state that relate chemical potential μ to the mean numbers of *s* and *d* electrons,

$$n_s = [n_s] + f_s R_s K_s, \quad n_p = [n_p] + f_p R_p K_p. \tag{12}$$

The square brackets in these equations stand for the integral part, while the end multipliers f_p and f_s and the

coefficients R_s and R_p are calculated for each integer interval of n_s and n_p values and given in the table. The K_s and K_p functions normalized to unity are expressed through the integrals of Fermi functions $n_F(\epsilon)$:

$$K_s = \sum_{\mathbf{p},\,\lambda=\pm} A_{\mathbf{p}}^{(-\lambda)} n_F(\xi_{\mathbf{p}}^{\lambda}),$$
$$K_p = \frac{1}{4}\sum_{\mathbf{p}}\left\{\sum_{\lambda=\pm} A_{\mathbf{p}}^{(\lambda)} n_F(\xi_{\mathbf{p}}^{\lambda}) + \sum_{\nu=o,\pm} n_F(\xi_{\mathbf{p}}^{\nu})\right\}. \quad (13)$$

The normal coordinates can conveniently be expressed through the same variables as those used for energies of hybridized excitations

$$A_s^{(\pm)}(y) = \frac{1}{2}\left\{1 \pm \frac{\mathrm{sgn}(r-v)}{\sqrt{1+sy^2}}\right\}, \quad s = \frac{144 g_p^2 f_p f_s t^2}{(r-v)^2}, \quad (14)$$

$$y^2 = \tau_p^2 \sin^2(p_z/2),$$
$$\xi_s^{\pm}(y) = -\frac{v}{2} \pm \frac{|r-v|}{2}\sqrt{1+sy^2} - \mu, \quad (15)$$
$$\tau_p = \frac{\sqrt{2}}{3}\sqrt{3 - S_1(p)}, \quad \mu = -\frac{\epsilon_p + \epsilon_s}{2},$$

$$\xi_p^{\pm}(x) = \pm vx + \frac{r}{2} - \mu, \quad 0 < x < 1,$$
$$\xi^o = v + \frac{r}{2} - \mu, \quad r = \epsilon_p - \epsilon_s, \quad v = \frac{3}{2} g_p^2 f_p \tau. \quad (16)$$

Further calculations are performed with the use of a flat-band model in which the density of states for τ_p is replaced by a constant. The excitation energies depend on the transverse momentum p_z through the $\sin^2(p_z/2)$ multiplier. The resulting expression for the density of states is evaluated by the following formula:

$$\rho(\epsilon) = \frac{2}{\pi}\int_0^1 d\xi \int_0^{\pi/2} d\alpha\, \delta(\epsilon - \xi\sin^2(\alpha)) = \frac{2}{\pi}\sqrt{\frac{1-\epsilon}{\epsilon}}. \quad (17)$$

With this density of states, the integrals in the equations of state take the form

$$K_s = \sum_{\lambda=\pm}\frac{4}{\pi}\int_0^1 A_s^{(-\lambda)}(y) n_F(\xi_s^{(\lambda)}(y))\sqrt{1-y^2}\,dy,$$
$$K_p = \frac{1}{4}\left\{\sum_{\lambda=\pm}\frac{4}{\pi}\int_0^1 A_s^{(\lambda)}(y) n_F(\xi_s^{(\lambda)}(y))\sqrt{1-y^2}\,dy + \int_{-1}^1 n_F(\xi_p(x))dx + n_F(\xi^o)\right\}. \quad (18)$$

From here on, the two $p^{\pm}$ subbands are regarded as a single subband with energy $\xi_p(x) = vx + \epsilon_p$ and a doubled density of states $\rho_p(x) = \theta(1-x^2)/v$.

The condition for Cooper pairing can be obtained using the general formula for the superconducting transition temperature in a system with infinite Hubbard energy [5–7]:

$$1 = \frac{\gamma_s \epsilon_s}{f_s}\sum_{\mathbf{p},\,\lambda=\pm}\frac{|A_{\mathbf{p}}^{(-\lambda)}|^2}{\xi_{\mathbf{p}}^{\lambda}}\tanh\left(\frac{\xi_{\mathbf{p}}^{(\lambda)}}{2T}\right) + \frac{\gamma_p \epsilon_p}{g_p^2 f_p}\sum_{\mathbf{p}}\left\{\sum_{\lambda=\pm}\frac{|A_{\mathbf{p}}^{(\lambda)}|^2}{\xi_{\mathbf{p}}^{\lambda}}\tanh\left(\frac{\xi_{\mathbf{p}}^{(\lambda)}}{2T}\right) + \sum_{\nu=\pm}\frac{1}{\xi_{\mathbf{p}}^{\nu}}\tanh\left(\frac{\xi_{\mathbf{p}}^{(\nu)}}{2T}\right)\right\}. \quad (19)$$

Accordingly, the BCS constant is represented as a sum $\Lambda_{\nu}^{\lambda} = \Lambda^{\lambda} + \Lambda_p^{\nu}$, where

$$\Lambda^{\pm} = 2\sum_{\mathbf{p}}\left\{\frac{\gamma_s \epsilon_s}{f_s}|A_{\mathbf{p}}^{(\mp)}|^2 + \frac{\gamma_p \epsilon_p}{g_p^2 f_p}|A_{\mathbf{p}}^{(\pm)}|^2\right\}\delta(\xi_{\mathbf{p}}^{\pm}),$$
$$\Lambda_p^{\nu} = 2\frac{\gamma_p \epsilon_p}{g_p^2 f_p}\sum_{\mathbf{p}}\delta(\xi_p^{(\nu)}(\mathbf{p})), \quad (20)$$

$\epsilon_p = r/2 - \mu$, and $\epsilon_s = -r/2 - \mu$. The remaining coefficients $\gamma_{s,p}$, g_p^2, and $f_{s,p}$ are determined separately for

Table

Interval	γ_s	f_s	g_s^2	R_s	K_s	f_s
$0 < n_s < 1$	–1	$1 - n_s/2$	1	2	$n_s/(2-n_s)$	$1/(1+K_s)$
$1 < n_s < 2$	1	$n_s/2$	1	1	$2(n_s-1)/(n_s)$	$1/(2-K_s)$
Interval	γ_p	f_p	g_p^2	R_p	K_p	f_p
$0 < n_p < 1$	–1	$1 - 3n_p/4$	1	4	$n_p/(4-3n_p)$	$1/(1+3K_p)$
$1 < n_p < 2$	–3/4	$(2+n_p)/12$	3/2	3	$4(n_p-1)/(2+n_p)$	$1/(4-K_p)$
$2 < n_p < 3$	3/4	$(6-n_p)/12$	3/2	4	$3(n_p-2)/(6-n_p)$	$1/(3+K_p)$
$3 < n_p < 4$	1	$(3n_p-8)/4$	1	1	$4(n_p-3)/(3n_p-8)$	$1/(4-3K_p)$

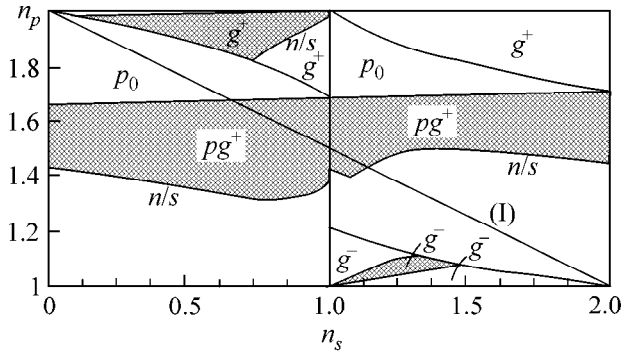

Fig. 2. Phase diagram at $T = 0$. The superconducting regions are crosshatched. Straight line (I) is the MgB_2 electroneutrality line.

each integer interval of variables n_s and n_p (table). The dimensionless amplitudes γ_s and γ_p are calculated by the Dyson method for each integer interval of the n_s and n_p values and summarized in the table [5–7].

In the model considered, the integrals with respect to momenta each depend on a single parameter that is determined by a given Fermi level. For this reason, the integration of the δ functions gives rise to the $\rho_\pm$ and ρ_p multipliers standing for the density of states at the corresponding Fermi surfaces $\xi_s^{(\pm)}(y) = 0$ and $\xi_p(x) = 0$. The densities of states depend on the parameters y and x:

$$\rho_s^{(\pm)}(y) = \rho_s(y) = \frac{8}{\pi}\frac{\sqrt{(1+sy^2)(1-y^2)}}{s|y||r-v|}, \qquad \rho_p(x) = \frac{1}{v}\theta(1-x^2). \tag{21}$$

In the case that one of the subbands is filled, the effective BCS constant is equal to the product of the energy multiplier and the corresponding density of states. Accordingly, there are three variants

$$\Lambda^{\pm}(y) = 2\left\{\frac{\gamma_s\epsilon_s}{f_s}\left|A_s^{(\mp)}(y)\right|^2 + \frac{\gamma_p\epsilon_p}{g_p^2 f_p}\left|A_s^{(\pm)}(y)\right|^2\right\}\rho_s(y), \qquad \Lambda_p(x) = 2\frac{\gamma_p\epsilon_p}{g_p^2 f_p}\rho(x). \tag{22}$$

If the p subband overlaps with the upper or lower subband $\xi_s^{(\pm)}(y)$, the density of p states depends on the position of Fermi level. In this case,

$$\Lambda^{(\pm)}(x,y) = 2\left\{\frac{\gamma_s\epsilon_s}{f_s}\left|A_s^{(\mp)}(y)\right|^2 + \frac{\gamma_p\epsilon_p}{g_p^2 f_p}\left|A_s^{(\pm)}(y)\right|^2\right\}\rho_s(y) + 2\frac{\gamma_p\epsilon_p}{g_p^2 f_p}\rho_p(x), \tag{23}$$

where the y and x variables are related to each other through the condition for equality of chemical potentials:

$$x = -\frac{1}{2} - \frac{r}{2v} \pm \frac{|r-v|}{2v}\sqrt{1+sy^2}, \qquad \frac{r}{v} = 1 + 8\,\mathrm{sgn}(r-v)\frac{t}{\tau}\sqrt{\frac{f_s}{sg_p^2 f_p}}. \tag{24}$$

Inasmuch as the larger (compared to the B–B distances) Mg–B distances are compensated in part by the more extended (compared to boron) magnesium wave function, the numerical calculation of the phase diagram was carried out for a particular case $t = \tau/4$ (Fig. 2).

In the $n_s < 1$ region, superconductivity appears only starting at a certain energy level, because the p- and s-electron scattering amplitudes are positive at low energies. It appears in the region of sufficiently large energies, where the boron p subband overlaps with the upper hybridized g^+ subband.

Superconductivity is absent if the Fermi level coincides with the energy of localized p_o states. It appears again when the Fermi level reaches the energy of the upper hybridized g^+ subband. The Λ constant is maximal in this case because the density of states at the lower edge of the hybridized subband has a root singularity typical of a one-dimensional motion along the crystal axis.

In the $1 < n_s < 2$ region, where the upper Hubbard s-electron subband is filled, superconductivity occurs even for low energies of s–p excitations, because the s–s-scattering amplitude becomes negative in this region, while the number of p-electron excitations with positive scattering amplitude is small.

As the energy increases, the boron p subband overlaps with the hybridized s–p subband. In this region, superconductivity appears only if the energy of boron electrons achieves a value for which their scattering amplitude becomes negative.

The corresponding s/n boundary appears in the region where the negative p–p-scattering amplitude compensates for the positive s–s-scattering amplitude.

One can see from Fig. 2 that the MgB_2 electroneutrality line (I) intersects the superconducting regions where the upper hybridized subband overlaps with the upper half of the boron p subband. However, it does not intersect the $g^\pm$ regions corresponding to the filling of purely hybridized subbands.

Therein lies the main distinction of the MgB_2 superconductivity from the cuprate superconductivity, in which the anion–cation distances are the shortest, as compared to the anion–anion and cation–cation separations.

Since the magnesium Hubbard energy does not differ strongly from the copper Hubbard energy, one can assert that the superconductivity mechanism in MgB_2 is

basically no different from the superconductivity mechanism in cuprate compounds.

I am grateful to V.G. Orlov and N.A. Babushkina for the information about the discovery of superconductivity in MgB_2.

REFERENCES

1. J. Akimitsu, in *Proceedings of the Symposium of Transition Metal Oxides, Sendai, 2001*.
2. G. V. Samsonov, T. N. Serebryakova, and V. A. Neronov, *Borides* (Atomizdat, Moscow, 1975).
3. J. Hubbard, Proc. R. Soc. London, Ser. A **281**, 401 (1964).
4. V. J. Emery, Phys. Rev. Lett. **58**, 2794 (1987).
5. R. O. Zaĭtsev, Fiz. Tverd. Tela (Leningrad) **31**, 1725 (1989).
6. R. O. Zaitsev, Solid State Commun. **76**, 795 (1990).
7. R. O. Zaĭtsev and Yu. V. Mikhaĭlova, Zh. Éksp. Teor. Fiz. **109**, 1859 (1996) [JETP **82**, 1001 (1996)].

Translated by V. Sakun

JETP Letters, Vol. 73, No. 7, 2001, pp. 336–340. Translated from Pis'ma v Zhurnal Éksperimental'noĭ i Teoreticheskoĭ Fiziki, Vol. 73, No. 7, 2001, pp. 378–382.

Band Structure of the Superconducting MgB_2 Compound and Modeling of Related Ternary Systems

N. I. Medvedeva, J. E. Medvedeva*, A. L. Ivanovskiĭ, V. G. Zubkov, and A. J. Freeman*

Institute of Solid-State Chemistry, Ural Division, Russian Academy of Sciences, Yekaterinburg, 620219 Russia
e-mail: medvedeva@ihim.uran.ru

**Department of Physics and Astronomy, Northwestern University, Evanston, Illinois 60208-3112, USA*

Received February 22, 2001

Band structure of a novel superconductor—magnesium diboride—is studied by the self-consistent FP-LMTO method. Density of states near the Fermi level of MgB_2 and its electronic properties are governed by the metal-like boron 2*p* orbitals in the planar network of boron atoms. The modification of the band structure of MgB_2 upon doping the boron (with Be, C, N, and O substitutional impurities) and the magnesium (with Be, Ca, Li, and Na substitutional impurities) sublattices or upon the introduction of structural vacancies (boron nonstoichiomety) is analyzed. The electronic structures of MgB_2 and hypothetical CaB_2 are also studied as functions of pressure. © *2001 MAIK "Nauka/Interperiodica".*

PACS numbers: 71.20.Ps; 71.15.Nc

The discovery (in January, 2001 [1]) of a superconducting transition in magnesium diboride (MgB_2) may become a milestone in further development of the superconductivity concept. In contrast to known high-T_c superconductors, the composition and structure of MgB_2 (it belongs to a large group of *p*-, *d*-, and *f*-metal diborides with the AlB_2-type structure; space group $P6/mmm$ and $Z = 1$ [2]) are exceedingly simple. At the same time, its transition temperature ($T_c \approx 40$ K) is "intermediate" because it is more than twice as high as the highest T_c values of "ordinary" superconductors, e.g., binary phases with the structures of the *B*1 (NbN, $T_c \approx 17.3$ K) or *A*15 (Nb_3Ge, $T_c \approx 23$ K [3]) type.

No doubt, the discovery of such a pronounced superconducting effect in a representative of a new class of substances (diborides) will initiate in the near future inquiries into the nature of superconductivity in MgB_2 and a search for superconductivity in related compounds. In the latter case, the general strategy consists in the extension of the class of possible MgB_2-based superconductors by the planned modification of the chemical composition of the generic compound (MgB_2).

It is the purpose of this work to study in detail the electronic energy spectrum (EES) of MgB_2 and theoretically forecast the electronic properties of MgB_2 with modified composition and lattice parameters. It has been pointed out in [4] that the superconducting effect in MgB_2 can be explained within the framework of the standard electron–phonon mechanism. The critical temperature for this mechanism is given by the well-known McMillan formula $T_c \approx \langle\omega\rangle \exp\{f(\lambda)\}$, where $\langle\omega\rangle$ is the mean phonon frequency (inversely proportional to the atomic mass) and λ is the electron–phonon coupling constant; $\lambda \sim N(E_F)\langle I^2\rangle$, where $N(E_F)$ is the density of states (DOS) at the Fermi level and $\langle I^2\rangle$ is the electron–ion matrix element specified by the bond ionicity in the compound. It follows from this formula that in the search for new superconductors with enhanced T_c among the MgB_2-related binary and multicomponent compounds one should take into account that the possible candidates must satisfy the following requirements: they must (1) have large $N(E_F)$ values, (2) mainly consist of light atoms, and (3) have a sufficiently large ionic component of the metal–boron bond.

One of the ways to modify the superconducting properties of MgB_2 amounts to preparing ternary solid solutions on its base by doping the sublattices with foreign atoms. Depending on their nature, the dopants may function as both hetero- and isoelectronic impurities and, respectively, either change the concentration of valence electrons (VEC) or leave it constant. We have analyzed the possible consequences of (1) doping the boron sublattice (with heteroelectronic impurities Be, C, N, and O), (2) doping the magnesium sublattice (with the iso- and heteroelectronic impurities Be, Ca, Li, and Na), and (3) modifying the diboride composition through the formation of vacancies in the B sublattice.

It is worth noting that MgB_2 falls far short of being the first superconducting compound among the boron-containing phases. This effect ($T_c \sim$ several kelvin) is known for some ternary borides (of the $LnRh_4B_4$ type [5]); rather high T_c values (≈16–23 K) were found in a group of the so-called borocarbide intermetallic compounds (BCICs) such as layered four-component

phases of the $LuNi_2B_2C$ type [6]. The studies have shown (see review [7]) that BCICs can be assigned to the superconductors with the BCS-type superconductivity. It should be emphasized that the transition-metal (M) states make a sizable contribution to the near-Fermi BCIC states that are involved in the mechanism of electron–phonon interaction (with high-frequency Ba_{1g} phonons). The interatomic bonds are formed by the strong covalent M–B and C–B interactions and greatly influence the lattice dynamics [7].

The electronic structure and the nature of the chemical bond in MgB_2 are basically different. The first *ab initio* band calculation (by the FP-LMTO method) [8] has shown that the energy bands in MgB_2 are formed due to the strong B–B interactions (in the planar hexagonal networks of boron atoms). The Fermi level falls within the band of bonding states so that the boron $2p$ states make the greatest contribution to the $N(E_F)$ value. The DOS profile displays a pronounced B($2p$)-like peak at the Fermi level. Note that, as shown in [8], E_F in AlB_2 is positioned in the region of a pseudogap that separates the bonding and antibonding bands, resulting in a sharp decrease in $N(E_F)$. In conjunction with other factors (increase in the covalent component of the metal–boron bond and decrease in the fraction of the B–B bond), the results [8] indicate that superconductivity in AlB_2 is highly improbable.

The mechanism of formation of interatomic bonds in MgB_2 is examined in detail in our work [8], where the cohesion energies (E_{coh}) were compared for MgB_2 and two hypothetical "MgB_2" structures with removed boron and magnesium layers, respectively. Numerical estimates of the contributions from different bond types to E_{coh} of the crystal showed that the B–B bonds in the graphite-like boron networks are the strongest, while the Mg–B and Mg–Mg interactions are much weaker [B–B (68%), B–Mg (23%), and Mg–Mg (9%)]. The E_{coh} value correlates with the melting temperature of the crystal and its lattice stability. It is not high for MgB_2; a comparison with our FP-LMTO results for almost all known *p*- and *d*-metal diborides [8–10] indicates that it is close to the E_{coh} value for MnB_2 diboride, which exists only in the form of a high-temperature modification.

In this work, the band calculations are carried out for MgB_2 by the *ab initio* self-consistent FP-LMTO method [11] using a supercell ($2 \times 2 \times 1$) incorporating four unit cells of MgB_2. The ternary borides of formal stoichiometry $MgB_{1.75}$(Be, C, N, O)$_{0.25}$, $Mg_{0.75}$(Be, Ca, Li, Na)$_{0.25}B_2$, and $Mg_{0.5}$(Li, Na)$_{0.5}B_2$ were modeled by substituting the Be, C, N, O or Be, Ca, Li, Na impurities for the B and Mg atoms in the Mg_4B_8 supercell, respectively. A nonstoichiometric composition of the $MgB_{1.75}$ boride was modeled by introducing structural vacancy ($\square_B$). In all calculations, the structural parameters of ideal MgB_2 were used and the lattice relaxation effects caused by the introduction of impurities (or vacancy) were disregarded.

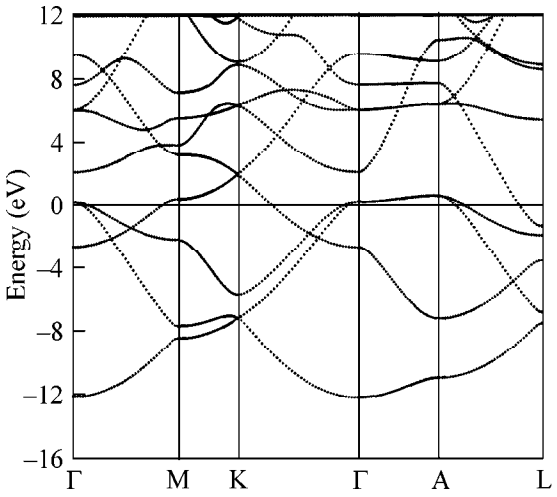

Fig. 1. Energy bands of MgB_2.

The energy bands of MgB_2 are presented in Fig. 1. All bands show a considerable dispersion. The $E(k)$ dependences are markedly different for different symmetry directions in the Brillouin zone (BZ). The $E(k)$ dispersion law for the bonding B($2p_{x,y}$)-type bands is the greatest in the $k_{x,y}$ direction (Γ–K). These bands are of the two-dimensional (2D) type and form plateaus in the k_z direction (Γ–A). They reflect the distribution of pp_σ states in the planar graphite-like boron networks. These states make a sizable contribution to the DOS at the Fermi level and are responsible for the metallic properties of diboride (Fig. 2). Since the Fermi level is situated in the bonding region, the conduction of MgB_2 is of the hole type. The cylindrical Fermi surface at the Γ point is formed by two $p_{x,y}$ bands. Note that it was assumed in [12] that the hole type of carriers is the necessary condition for the appearance of superconductivity in magnesium diboride.

A group of B($2p_z$)-like bands reflect the weaker pp_π interactions between the atomic layers (the ratio of intra- to interplanar distances is ~0.58). These 3D-like bands show the greatest dispersion in the k_z direction (Γ–A). The Mg *s*, *p* and B *s* states mix with the B($2p$)-like bands at the bottom of valence band and in the conduction band. The Mg atoms are in the cationic state, with the charge transfer occurring in the Mg ⟶ B direction.

As is mentioned above, the variation of the topology, energy, and composition of the near-Fermi bands may prove to be an important factor governing the superconducting properties of the multicomponent phases based on magnesium diboride. Such a variation may be attained by the planned doping of MgB_2. For the purpose of predicting the results of possible attempts at synthesizing new MgB_2-based ternary

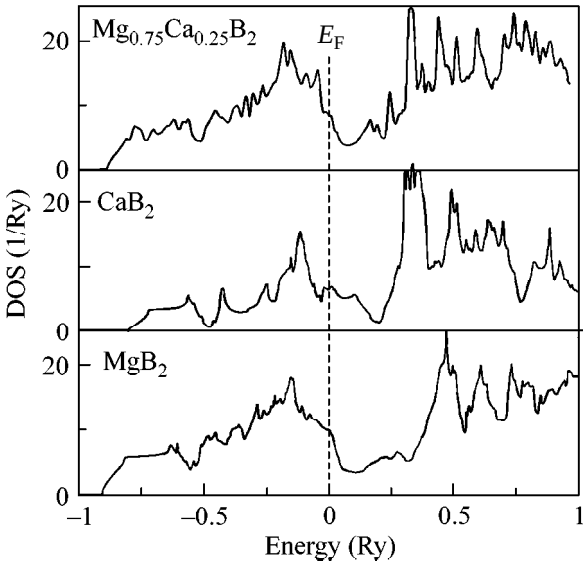

Fig. 2. Density of states for MgB_2, hypothetical CaB_2, and ternary phase $Mg_{0.75}Ca_{0.25}B_2$.

borides, we modeled how the band structure of MgB_2 is affected (1) upon doping the boron sublattice (with Be, C, N, and O), (2) upon doping the magnesium sublattice (with Be, Ca, Li, and Na), and (3) upon the formation of vacancies in the B sublattice.

A rigid-band scheme is a widely used model allowing the analysis of possible results of such experiments. Based on the calculated spectra of MgB_2, this model predicts the following effects. The substitution of the Be, C, N, and O atoms for boron in MgB_2 (VEC = 8*e*) both decreases ($MgB_{1.75}Be_{0.25}$; VEC = 7.75*e*) and increases VEC to 8.25 ($MgB_{1.75}C_{0.25}$) and 8.75*e* ($MgB_{1.75}O_{0.25}$). The replacement of the Mg atoms by Li, Na, Be, and Ca in the cationic sublattice either decreases [$Mg_{0.75}(Li, Na)_{0.25}B_2$; VEC = 7.75*e*] or does not change the VEC [$Mg_{0.75}(Be, Ca)_{0.25}B_2$; VEC = 8*e*]. One should expect that some of the bands become "depleted" with a decrease in VEC (the B $\longrightarrow$ Be, $\square_B$ and Mg $\longrightarrow$ Li, Na substitutions), E_F shifts inside the valence band, and the near-Fermi DOS increases. The dopants increasing VEC (the B $\longrightarrow$ C, N, and O substitutions) are expected to produce the opposite effect: E_F is shifted into the region of a deep DOS minimum. The role of isoelectronic impurities remains unclear in this model. One may assume that the effects in this case are mainly associated with the lattice deformation, i.e., with change in *c*/*a*.

Density of states at the Fermi level [$N(E_F)$, 1/(Ry f.u.)] for MgB_2 and some ternary phases on its base

Boride	$N(E_F)$	Boride	$N(E_F)$
MgB_2	11.44	$Mg_{0.75}Li_{0.25}B_2$	11.89
$MgB_{1.75}$	9.01	$Mg_{0.75}Na_{0.25}B_2$	9.53
$MgB_{1.75}Be_{0.25}$	10.47	$Mg_{0.75}Be_{0.25}B_2$	10.61
$MgB_{1.75}C_{0.25}$	5.79	$Mg_{0.75}Ca_{0.25}B_2$	11.34
$MgB_{1.75}N_{0.25}$	8.04	$Mg_{0.5}Li_{0.5}B_2$	9.39
$MgB_{1.75}O_{0.25}$	9.46	$Mg_{0.5}Na_{0.5}B_2$	9.43

The numerically calculated EES of the hypothetical ternary borides display a more complicated behavior (Figs. 2–4, table) and lead to the following conclusions.

1. Doping of the boron sublattice. As the VEC decreases (in the order of $MgB_2 \longrightarrow MgB_{1.75}Be_{0.25} \longrightarrow MgB_{1.75}$), E_F systematically shifts to larger binding energies but $N(E_F)$ diminishes. This occurs because of the bond system destruction in the graphite-like boron layers, the splitting of the near-Fermi bands, and a change in their dispersion law near E_F. The EES parameters change nonmonotonically upon the transition $MgB_2 \longrightarrow MgB_{1.75}C_{0.25} \longrightarrow MgB_{1.75}N_{0.25} \longrightarrow MgB_{1.75}O_{0.25}$. As the dopant's electronegativity rises (C $\longrightarrow$ O), (1) the impurity C,N,O(2*s*, 2*p*) bands are systematically shifted to higher binding energies and (2) the C,N,O(2*p*)-band splitting into the bonding and antibonding bands decreases as a result of weakening the boron–impurity interactions. The impurity 2*p* bands form peaks in the region of DOS minimum (Fig. 3). As a result, a sharp decrease in $N(E_F)$ upon the $MgB_2 \longrightarrow MgB_{1.75}C_{0.25}$ transition ($MgB_{1.75}C_{0.25} \longrightarrow MgB_{1.75}N_{0.25} \longrightarrow MgB_{1.75}O_{0.25}$) gives way to a rise in $N(E_F)$. Nevertheless, in all borides doped at the B sublattice, $N(E_F)$ is smaller than in the ideal magnesium boride. These results indicate that attempts at markedly increasing the density of near-Fermi states by varying composition of the boron sublattice are hopeless. It should also be taken into account that the doping of the boron sublattice encounters difficulties associated with the energetic effect accompanying the "rupture" of the strong B–B bonds and the possible lattice relaxation from the planar geometry of the host crystal.

2. Doping of the magnesium sublattice. Considering the binding energies of the substituted center (Mg) in the matrix, this approach seems to be much more realistic. As the VEC decreases for $MgB_2 \longrightarrow Mg_{0.75}Li_{0.25}B_2$ or $MgB_2 \longrightarrow Mg_{0.75}Na_{0.25}B_2$, the Fermi level shifts to lower energies, but no appreciable increase in the near-Fermi DOS occurs. For the compounds considered, a small increase in $N(E_F)$ was found for the Mg $\longrightarrow$ Li substitution; additional DOS peaks emerge near E_F upon the Mg $\longrightarrow$ Na substitution (Fig. 4). An increase in the dopant concentration [$Mg_{0.5}(Li, Na)_{0.5}B_2$ system] and the isoelectronic substitutions $MgB_2 \longrightarrow Mg_{0.75}Be_{0.25}B_2$ and $MgB_2 \longrightarrow Mg_{0.75}Ca_{0.25}B_2$ do not raise $N(E_F)$ (Figs. 2, 4 and table).

Thus, the theoretical modeling of the effects caused by the modification of the energy spectrum of MgB_2 upon doping its sublattices with iso- and heteroelectronic impurities or upon the introduction of lattice

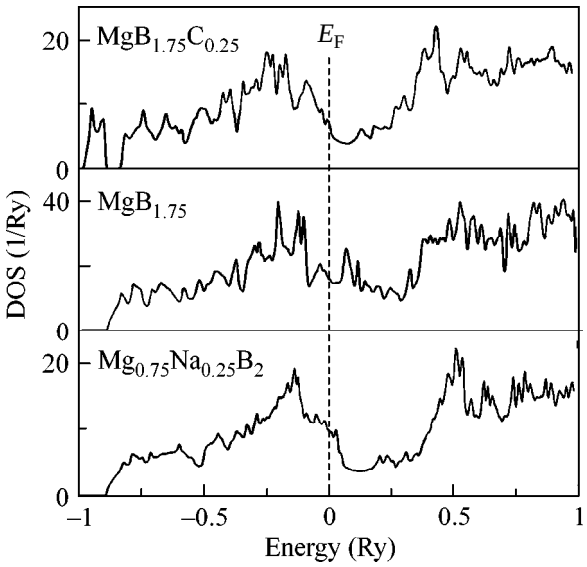

Fig. 3. Density of states for nonstoichiometric $MgB_{1.75}$ and ternary hexagonal phases $MgB_{1.75}C_{0.25}$ and $Mg_{0.75}Na_{0.25}B_2$.

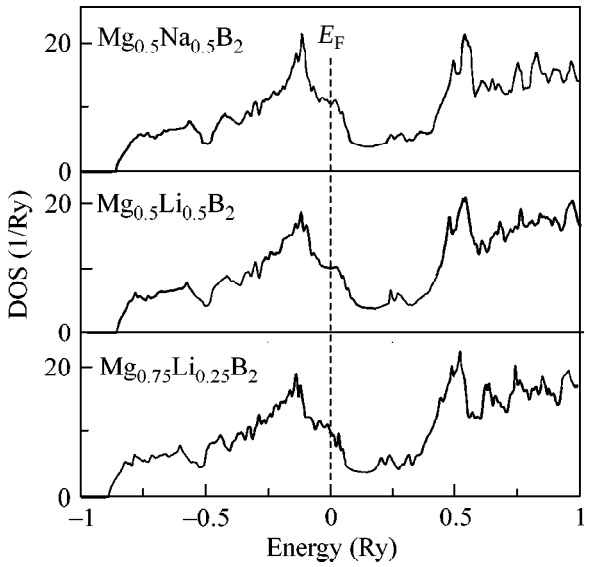

Fig. 4. Density of states for ternary hexagonal phases $Mg_{0.75}Li_{0.25}B_2$ and $Mg_{0.5}M_{0.5}B_2$ (M = Li and Na).

vacancies has demonstrated that attempts at increasing the density of near-Fermi states by doping the boron sublattice are inefficient. It is found that, among the cationic dopants considered, Li slightly increases $N(E_F)$ upon replacing 25% of Mg; i.e., the cationic substitution can be considered as a possible way of controlling those properties which are determined by the density of near-Fermi states. It should also be noted that T_c may be increased by increasing phonon frequencies as a result of replacing Mg by lighter atoms (Li, Na, and Be).

Note in conclusion that a change in the lattice parameters may become an important factor in the modification of the electronic spectrum of MgB_2 (and related compounds). A check of the simplest case (modeling of the isotropic compression of MgB_2 in the pressure range 0–10 GPa) showed that $N(E_F)$ slightly increased (by ≈5%) with pressure. Because of a high rigidity of the system of B–B bonds in the planar boron networks, a change in the interplanar spacing (ratio of unit-cell parameters c/a) may become much more efficient. For the diboride family, this value is known to vary (depending on the cation radius r_c) over rather wide limits [2]. We carried out preliminary calculations for MgB_2 and estimated the role of this parameter upon changing c/a from 1.08 to 1.16. The corresponding $N(E_F)$ value changed in the range 8.5–11.8 state/Ry. For the hypothetical CaB_2 (for which the equilibrium lattice parameters were found to be a = 3.205 Å and c/a = 1.24), the $N(E_F)$ value increased to 20.8 state/Ry. One can see from Fig. 5 that this is caused by the localization of the B p_z states near the Fermi level.

The c/a ratio in superconducting MgB_2 can be increased, e.g., through the substitution of large-radius isoelectronic atoms such as Ca, Sr, or Ba (r_c = 1.04, 1.20, and 1.38 Å, respectively) for magnesium (Mg; r_c = 0.74 Å). The formation of hexagonal diboride structures with alternating layers of atoms of different sort (of the type …B/Ca/B/Mg/B/…) is one of the possible ways. The calculations of the EES of these structures, of the lattice relaxation effects caused by the introduction of substitutional impurities, and of the formation energies (characterizing the feasibility of one or another substitution, i.e., practical implementation of the corresponding ternary systems) are now in progress.

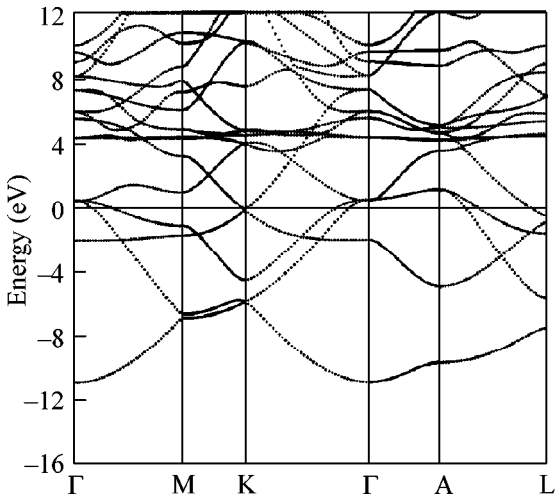

Fig. 5. Energy bands of hypothetical CaB_2.

REFERENCES

1. J. Akimitsu, in *Proceedings of the Symposium on Transition Metal Oxides, Sendai, 2001*.
2. B. Aronsson, T. Lundstrom, and S. Rundqvist, *Refractory Borides, Silicides and Phosphides* (Methuem, London, 1965).
3. S. V. Vonsovskiĭ, Yu. A. Izyumov, and É. Z. Kurmaev, *Superconductivity of Transition Metals, Their Alloys, and Compounds* (Nauka, Moscow, 1977).
4. J. Kortus, I. I. Mazin, K. D. Belashenko, *et al.*, cond-mat/0101446 (2001).
5. R. B. King, J. Chem. Inf. Comput. Sci. **39**, 180 (1999).
6. R. J. Cava, H. Takagi, B. Batlogg, *et al.*, Nature **367**, 146 (1994).
7. A. L. Ivanovskii, Russ. Chem. Rev. **67**, 357 (1998).
8. A. L. Ivanovskii and N. I. Medvedeva, Russ. J. Inorg. Chem. **45**, 1234 (2000).
9. A. L. Ivanovskiĭ, N. I. Medvedeva, Yu. E. Medvedeva, *et al.*, Metallofiz. Noveĭshie Tekhnol. **20**, 41 (1998).
10. A. L. Ivanovskiĭ, N. I. Medvedeva, and Yu. E. Medvedeva, Metallofiz. Noveĭshie Tekhnol. **21**, 19 (1999).
11. M. Methfessel and M. Scheffler, Physica B (Amsterdam) **172**, 175 (1991).
12. J. E. Hirsch, cond-mat/0102115 (2001).

Translated by V. Sakun

JETP Letters, Vol. 73, No. 7, 2001, pp. 341–343. From Pis'ma v Zhurnal Éksperimental'noĭ i Teoreticheskoĭ Fiziki, Vol. 73, No. 7, 2001, pp. 383–385.

Charged Frenkel Biexcitons in Organic Molecular Crystals[1]

V. M. Agranovich, O. A. Dubovsky, and A. M. Kamchatnov

Institute of Spectroscopy, Russian Academy of Sciences, Troitsk, Moscow region, 142190 Russia

e-mail: kamch@isan.troitsk.ru

Received January 30, 2001; in final form, February 20, 2001

It is known that the energy of the lowest electronic transition in the neutral molecules of anthracene, tetracene, and other polyacenes is blue-shifted in comparison with the corresponding transition energy in univalent molecular ions. This effect in a molecular crystal may be responsible for the attraction between a molecular (Frenkel) exciton and a charge carrier. Due to this attraction, a bound state of Frenkel exciton and free charge (charged Frenkel exciton) may be formed [5]. As we demonstrate below, the same mechanism can be responsible for the formation of a charged biexciton (bound state of two Frenkel excitons and a charge carrier). A one-dimensional lattice model is used which corresponds to *J* aggregates and is also a good approximation for quasi-one-dimensional crystals. Calculations are performed for molecular crystals like tetracene, where the exciton band at low temperature is much narrower than the band of the charge carrier. © *2001 MAIK "Nauka/Interperiodica"*.

PACS numbers: 71.35.Aa

Investigations of physical properties of molecular crystals under conditions where both excitons and charge carriers are present in a crystal have a long history (see, e.g., [1]). It was shown, for example, that an exciton can transfer its energy to a charge, either a trapped one, causing its detrapping, or to a free one, which is then excited to a higher conducting state. This direction of investigations has recently received new emphasis after high-quality crystals made of various molecular compounds were grown, and it was shown that these crystals demonstrate high carrier mobility [2]. Bandlike motion of delocalized charge carriers has been clearly observed at low temperatures in molecular crystals of various polyacenes and oligothiophenes. One may expect that various effects of exciton–charge interactions can be investigated in such crystals.

Interaction of a charge carrier with an exciton can arise due to different physical mechanisms. One of them is the Coulomb interaction [3] caused by a change in the polarizability of a molecule upon its excitation. This interaction decreases with distance r between exciton and charge carrier as r^{-4} and is highly anisotropic. Another mechanism is due to the fact that the excitation energy of an ionized molecule may differ from that of the neutral molecule by some negative value $-\Delta$ ($\Delta > 0$); see, e.g., [4]. This leads to a contact exciton–charge interaction and to the formation of bound states of a Frenkel exciton and a free charge carrier [5]. Such "charged" excitations might be important in applications, since the motion of these quasiparticles and, hence, transport of their energy can be controlled by an external electric field. In this paper, we demonstrate that the bound states of two Frenkel excitons and one charge carrier can also be formed due to the short-range interaction of the above-mentioned nature. For definiteness, we will consider negatively charged biexcitons formed by two Frenkel excitons and an electron by invoking experimental data for negative molecular ions [4].

We consider a one-dimensional lattice with one molecule in a unit cell labeled index n and introduce the creation and annihilation operators $B_n^\dagger$ and B_n for excitons and $c_n^\dagger$ and c_n for electrons. We restrict ourselves to the case of "heavy" excitons with the energy-bandwidth much narrower than that of an electron. According to [2], such a situation takes place, for example, for singlet excitons in tetracene at low temperature, where the excitonic hopping matrix element V_{exc} is about 50 cm^{-1}, whereas the electronic hopping matrix element V is about 350 cm^{-1}. For such molecular structures, we can use the adiabatic approximation and neglect, to the first order, the exciton motion. Such adiabatic approximation may be even better for triplet excitons in molecular crystals, for which the hopping matrix element is about 5–10 cm^{-1}. Thus, in this approximation we have to find the solution of a one-particle Schrödinger equation for an electron moving in the potential created by two excitons located at two dif-

[1] This article was submitted by the authors in English.

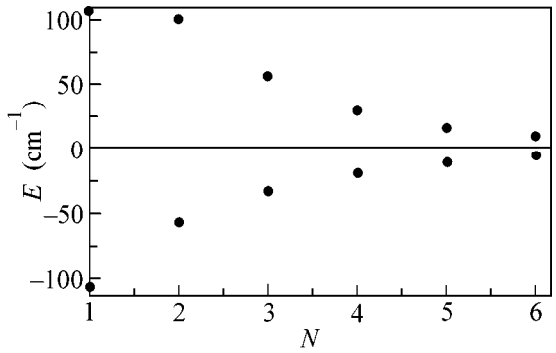

Dependence of the energy of a charged biexciton on the distance between excitons. Zero energy corresponds to the dissociated state consisting of the charged and uncharged excitons with infinite distance between them.

ferent sites of the lattice. The Hamiltonian of the system can be written in the form

$$H = E_0\sum_n B_n^\dagger B_n + \epsilon_0\sum_n c_n^\dagger c_n - V\sum_n (c_n^\dagger c_{n+1} + c_{n+1}^\dagger c_n) - \Delta\sum_n B_n^\dagger B_n c_n^\dagger c_n, \quad (1)$$

where we take into account only the nearest-neighbor interaction, E_0 is the energy of an exciton, ϵ_0 is the energy of an electron, V is the electron hopping matrix element ($V > 0$), and $\Delta > 0$ is the exciton–electron interaction constant. The wave function has the form

$$|3\rangle = \sum_p \psi_p B_n^\dagger B_m^\dagger c_p^\dagger |0\rangle, \quad (2)$$

where $|0\rangle$ is the "vacuum" state without any quasiparticles; and excitons are located at the sites n and m. Substitution of Eqs. (2) and (1) into the Schrödinger equation $H|3\rangle = E|3\rangle$ yields the system

$$E'\psi_p = V(\psi_{p+1} + \psi_{p-1}) - \Delta(\delta_{mp} + \delta_{np})\psi_p, \quad E' = E - 2E_0 - \epsilon_0 \quad (3)$$

for the energy E and electron amplitudes ψ_p. It can be easily solved for any n and m. At $p \longrightarrow \pm\infty$, the wave function ψ_p decays exponentially $\sim\exp(-\kappa|p|)$ and the energy E is connected with κ by the simple formula

$$E = 2E_0 + \epsilon_0 - 2V\cosh\kappa. \quad (4)$$

The parameter κ is determined by the equation

$$(\Delta/V)\cosh(\kappa N/2) = \exp[\kappa N/2]\sinh\kappa, \text{ even states}, \quad (\Delta/V)\sinh(\kappa N/2) = \exp[\kappa N/2]\sinh\kappa, \text{ odd states}, \quad (5)$$

where $N = |m - n|$, and $\psi_m = \psi_n$ for the even electronic states and $\psi_m = -\psi_n$ for the odd states.

For the case $N = 1$, when excitons are separated by one lattice constant, these equations are solved explicitly to give

$$\exp\kappa = \begin{cases}\Delta/V + 1, & \text{even states}\\ \Delta/V - 1, & \text{odd states},\end{cases} \quad (6)$$

and, hence, the energies of these states are given by

$$E = \begin{cases}2E_0 + \epsilon_0 - \Delta - V - V^2/(\Delta + V), & \text{even states}\\ 2E_0 + \epsilon_0 - \Delta + V - V^2/(\Delta - V), & \text{odd states}.\end{cases} \quad (7)$$

On the other hand, in the limit of large $\kappa N \gg 1$, each of Eqs. (5) gives

$$\exp\kappa = \frac{\Delta}{2V} + \sqrt{\left(\frac{\Delta}{2V}\right)^2 + 1}, \quad (8)$$

and thus the energy for both types of states becomes

$$E = 2E_0 + \epsilon_0 + E' = 2E_0 + \epsilon_0 - \sqrt{\Delta^2 + 4V^2}. \quad (9)$$

Due to the degeneracy of these states, this energy coincides with the energy of a partially dissociated state which consists of a charged exciton (bound state of an exciton and an electron) and a free exciton separated considerably from each other. Correction to Eq. (9) shows exponential dependence of the spectrum on N

$$E = 2E_0 + \epsilon_0 - \sqrt{\Delta^2(1 \pm 2e^{-\kappa(N+1)} + 4V^2)}, \quad N \gg 1/\kappa, \quad (10)$$

converging to energy (9) from below for the even states and from above for the odd states. The subtraction of energy (9) from the one given by Eq. (4) gives the binding energy of charged biexciton states for finite N.

For estimations, we use typical values $V = 300$ cm^{-1} [2] and $\Delta = 400$ cm^{-1} (anthracene) and $\Delta = 800$ cm^{-1} (tetracene) [4]. The dependence of binding energies $E_b = E(N) - E(\infty)$ on N for tetracene is shown in the figure. We see from this figure that the even charged biexciton states have energies smaller than energy (9) of the partially dissociated state, whereas the odd states have energies greater than the energy of the partially dissociated states. Hence, only even states are stable against the dissociation into charged and free excitons. Obviously, corrections to the adiabatic approximation will destroy the states with large N. The number of states with small N that can be observed experimentally depends crucially on the crystal parameters. In particular, in the case of parameters chosen above, the binding energy of a biexciton with $N = 1$ is about $\simeq 100$ cm^{-1}, which is greater than the width δ of the lowest energy excitonic resonance $\delta \lesssim 20$ cm^{-1} (see, e.g., [6]). The differences in binding energies of the states with $N = 1$ and 2 are about 50 cm^{-1}. Hence, at least these two states may be observed in spectroscopic experiments. The states considered must make a contribution to the biex-

citonic part of all optical nonlinearities, and this contribution is controlled by the concentration of free charge carriers. The formation of such states should lead to the dependence of carrier mobility on the exciton concentration in molecular crystals (anthracene, tetracene) doped with univalent ions and having dark conductivity and carriers arising due to the injection by means of field-effect transistors (see [2]).

The theory of charged biexcitons taking into account the exciton motion will be published later.

This work was supported in part by the Russian Foundation for Basic Research (project no. 99-03-32178) and the program "Physics of Nanostructures" of the Russian Ministry of Science and Technology (project no. 97-1074). V.M.A. acknowledges partial support from the Royal Society (UK).

REFERENCES

1. M. Pope and C. E. Swenberg, *Electronic Processes in Organic Crystals and Polymers* (Oxford Univ. Press, Oxford, 1999).
2. C. Kloc, P. G. Simpkins, T. Siegrist, and R. A. Landise, J. Cryst. Growth **182**, 416 (1997); J. H. Schoen, C. Kloc, and B. Batlogg, Phys. Rev. B **61**, 10803 (2000).
3. V. M. Agranovich and A. A. Zakhidov, Chem. Phys. Lett. **68**, 86 (1979).
4. G. J. Hoitink, N. H. Velthorst, and P. J. Zandstra, Mol. Phys. **3**, 533 (1960).
5. V. M. Agranovich, D. M. Basko, F. Bassani, *et al.*, Chem. Phys. (2001) (in press).
6. H. C. Wolf, Z. Naturforsch. A **13**, 414 (1958).

JETP Letters, Vol. 73, No. 7, 2001, pp. 344–348. Translated from Pis'ma v Zhurnal Éksperimental'noĭ i Teoreticheskoĭ Fiziki, Vol. 73, No. 7, 2001, pp. 386–391.

π-Phase Magnetism in Ferromagnet–Superconductor Superlattices

M. G. Khusainov[1,2,*], Yu. A. Izyumov[3], and Yu. N. Proshin[1,]**

[1] *Kazan State University, Kazan, 420008 Russia*

** e-mail: mgkh@vostok-inc.com*

*** e-mail: yurii.proshin@ksu.ru*

[2] *Kazan State Technical University, Chistopol, 422950 Russia*

[3] *Institute of Metal Physics, Ural Division, Russian Academy of Sciences, Yekaterinburg, 620219 Russia*

Received October 31, 2000; in final form, February 22, 2001

New 0π and ππ Larkin–Ovchinnikov–Fulde–Ferrell (LOFF) states with antiferromagnetic orientation of magnetizations in the neighboring layers of a ferromagnetic metal (FM) are predicted for FM/superconductor (FM/S) superlattices. Under certain conditions, the critical temperature T_c of these states is higher than for the known 00 and π0 LOFF states with ferromagnetic ordering of the FM layers. It is shown that the nonmonotonic behavior of T_c in the FM/S superlattices with S-layer thickness d_s less than the threshold value d_s^π is due to the phase transition cascade 0π–ππ–0π. At $d_s > d_s^\pi$, the T_c oscillations are caused by the 00–π0–00 transitions. New logic elements based on the FM/S structures and combining the advantages of the superconducting and magnetic data-record channels in a single sample are proposed. © *2001 MAIK "Nauka/Interperiodica".*

PACS numbers: 75.70.Cn; 74.80.Dm

The mutual influence of superconductivity and ferromagnetism in ferromagnetic metal/superconductor (FM/S) superlattices is characterized by a pronounced nonmonotonic dependence of critical temperature T_c on the thickness d_f of ferromagnetic interlayer [1, 2]. The existing theories of proximity effect in the FM/S superlattices [3–7] relate the $T_c(d_f)$ oscillations to a competition between the 0- and π-phase types of superconductivity in the neighboring S layers and disregard the back action of superconductivity on the magnetism of FM layers and mutual orientation of their magnetizations. One of us has shown in [8–10] that the long-range Ruderman–Kittel–Kasuya–Yosida (RKKY) exchange through the S layers in analogous structures with layers of a ferromagnetic dielectric (FD) playing the role of FM layers gives rise to a layered antiferromagnetic superconducting (AFS) state. In the AFS state, the magnetic order parameters of the neighboring ferromagnetic layers are π-shifted in phase. This markedly depresses the pair-breaking effect of exchange field I on the S layers and, hence, increases T_c of a layered structure. This type of superconducting and magnetic order-parameter adjustment resulting in the π-phase magnetism reflects the quantum coupling between the interfaces and should also be expected to occur in the FM/S superlattices. It was also predicted in [9, 10] that one can control the superconducting and magnetic states of the FD/S superlattices using an external magnetic field. In recent theoretical works [11, 12], this problem was studied only for an FM/S/FM trilayer.

Let us consider an FM/S superlattice formed by the d_f-thick FM and d_s-thick S layers alternating along the z axis. Superconductivity in such FM/S structures is a combination of Cooper pairing with zero total momentum in the S layers and Larkin–Ovchinnikov–Fulde–Ferrell (LOFF) pairing with nonzero total momentum **k** in the FM layers [5–7]. In studying the mutual adjustment of these competing types of pairing, on the one hand, and magnetism, on the other, the unit cell of the FM/S superlattice can conveniently be chosen as /S/FM/S/FM/. The corresponding boundary problem was formulated in terms of the Usadel function $F_{s(f)}(z, \omega, I)$ in our recent works [5–7]. The s and f indices hereafter refer the functions and parameters to the S and FM layers, respectively; ω is the Matsubara frequency; and the exchange field I of localized spins plays the role of magnetic order parameter in the FM layers.

The differential equations for the Usadel function $F_s(z, \omega)$ in the S layers of a unit cell $[0 < z < d_s; -(d_s + d_f) < z < -d_f]$ read

$$\left[\omega - \frac{D_s}{2}\frac{\partial^2}{\partial z^2}\right]F_s(z, \omega) = \Delta_s(z). \qquad (1)$$

Similarly, for $F_f(z, \omega, I)$ in the FM layers $[-d_f < z < 0; d_s < z < d_s + d_f]$, one has

$$\left[\omega + iI - \frac{D_f(I)}{2}\frac{\partial^2}{\partial z^2}\right]F_f(z, \omega, I) = \Delta_f(z, I). \quad (2)$$

In these equations, $D_{s(f)}$ is the ordinary diffusion coefficient and $D_f(I)$ is the complex diffusion coefficient given by the expressions (see [5–7]) $D_f(I) \simeq D_f/(1 + 2iI\tau_f)$ for $2I\tau_f < 1$ and $D_f(I) \simeq 3D_f/(1 + 2iI\tau_f)$ for $2I\tau_f > 1$ (τ is the electron mean free time). The boundary conditions corresponding to Eqs. (1) and (2) at the central FM/S interface $z = 0$ are

$$\frac{4D_s}{\sigma_s v_s}\frac{\partial F_s(z, \omega)}{\partial z}\bigg|_{z=+0} = \frac{4D_f(I)}{\sigma_f v_f}\frac{\partial F_f(z, \omega, I)}{\partial z}\bigg|_{z=-0} \quad (3)$$
$$= F_s(+0, \omega) - F_f(-0, \omega, I),$$

where σ_s and σ_f are the interface transparencies on the sides of S and FM metals, respectively; they satisfy the detailed balance relation $\sigma_s v_s N_s = \sigma_f v_f N_f$, where $N_{s(f)}$ and $v_{s(f)}$ are the Fermi density of states and the Fermi velocities, respectively. At the remaining unit-cell boundaries $z = d_s$, $z = -d_f$, $z = -(d_s + d_f)$, and $z = d_s + d_f$, the relations analogous to Eq. (3) are supplemented by the periodicity conditions

$$F(z + L, \omega, I) = e^{i\phi}F(z, \omega, Ie^{i\chi}), \quad (4)$$

where $L = d_s + d_f$ is the superlattice constant and ϕ and χ are the phases of superconducting and magnetic order parameters, respectively.

By solving boundary problem (3) and (4) for the Usadel function in conjunction with the Gor'kov self-consistency equations

$$\Delta_s(z) = 2\lambda_s\pi T\,\mathrm{Re}\sum_{\omega>0}{}' F_s(z, \omega),$$

$$\Delta_f(z, I) = 2\lambda_f\pi T\,\mathrm{Re}\sum_{\omega>0}{}' F_f(z, \omega, I)$$

(λ_s and λ_f are the dimensionless parameters of electron–electron interaction in the S and FM layers, respectively), the superconducting transition temperature of the FM/S contact can be determined as a function of interface transparency σ_s, layer thicknesses d_s and d_f, parameters $2I\tau_f$, $n_{sf} = N_s v_s/N_f v_f$, etc.

A strong pair-breaking effect of the exchange field I ($I \gg \pi T_{cs}$, where T_{cs} is the critical temperature of the isolated S layer) is the main mechanism of superconductivity damping in the FM/S systems. Ignoring, for simplicity, the electron–electron interaction in the FM layers ($\lambda_f = 0$ and $\Delta_f = 0$), we seek the solution of Eqs. (1)–(3) in the form of a linear combination of functions symmetric and antisymmetric about the centers of the S and FM layers. In particular, the corresponding solutions for the central FM/S contact in the unit cell have the form

$$F_s(z, \omega) = A(\omega)\frac{\cos[k_s(z - d_s/2)]}{\cos(k_s d_s/2)}$$
$$+ C(\omega)\frac{\sin[k_s(z - d_s/2)]}{\sin(k_s d_s/2)}, \quad 0 < z < d_s,$$
$$F_f(z) = B\frac{\cos[k_f(z + d_f/2)]}{\cos(k_f d_f/2)} \quad (5)$$
$$+ D\frac{\sin[k_f(z + d_f/2)]}{\sin(k_f d_f/2)}, \quad -d_f < z < 0,$$

where the coefficients $A(\omega)$, $C(\omega)$, B, and D are independent of z, while the wavenumbers k_s and k_f are independent of frequency ω ($\omega \ll I$) and describe the transverse spatial variation of the pair amplitude. The solutions for the two end S and FM layers in the /S/FM/S/FM/ unit cell are analogous to Eqs. (5) and should satisfy periodicity conditions (4). The minimization of the unit-cell free energy with respect to the phase of superconducting (ϕ) and magnetic (χ) order parameters yields four possible different LOFF states:

1) 00 phase ($\phi = 0, \chi = 0$);
2) π0 phase ($\phi = \pi, \chi = 0$);
3) 0π phase ($\phi = 0, \chi = \pi$); (6)
4) $\pi\pi$ phase ($\phi = \pi, \chi = \pi$).

In the 00 state, $C(\omega) = D = 0$, so that pair amplitudes (5) are even functions about the centers of the S and FM layers, whereas in the π0 phase $C(\omega) = B = 0$, so that the pair amplitude in the FM layer becomes odd. In the two new LOFF states 0π with $D = 0$ and $B \neq 0$ and $\pi\pi$ with $B = 0$ and $D \neq 0$, the coefficients $A(\omega)$ and $C(\omega)$ are nonzero; i.e., pair amplitude in the S layer is not characterized by a certain parity. The presence of an admixture of the sine solutions to the cosine solutions in Eq. (5) indicates that the paramagnetic effect of exchange field I is partially compensated in the S layers if the neighboring FM layers are in the AFS state with antiparallel orientations of their magnetizations.

The first two states 00 and π0 were considered earlier in [3–7], where it was tacitly assumed that $\chi = 0$, i.e., that the superlattice was in the ferromagnetic superconducting (FS) state [8–10] with parallel orientations of magnetizations of all FM layers. In the limit of large thicknesses of S layers, $d_s \gg \xi_s$ (ξ_s is the coherence length in the superconductor), this is justified because the mutual orientation of magnetizations in the neighboring FM layers is irrelevant as long as the antiferromagnetic RKKY exchange through the S interlayers is exponentially small [8–10]. However, for the short-period FM/S superlattices with thicknesses d_s close to the critical value $d_s^c \sim \xi_s$, the T_c values in the π-magnetic phases 0π and $\pi\pi$ are, likely, higher than in

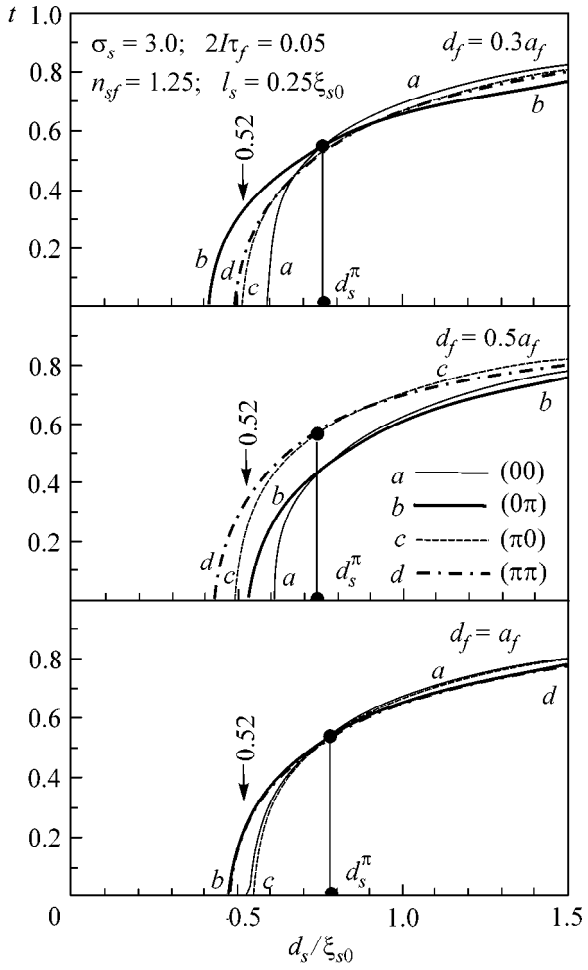

Fig. 1. Reduced critical temperature $t = T_c/T_{cs}$ of the FM/S superlattice vs. reduced thickness d_s/ξ_{s0} of the S layer for different thicknesses of the FM layer. The values of main parameters of the theory are indicated in the upper panel, and the curve assignment is shown in the middle panel. The $d_s = 0.52\xi_{s0}$ value indicated by the vertical arrows corresponds to the $t(d_f)$ curves in Fig. 2.

the 0-magnetic phases 00 and π0, respectively. Thus, the superconducting state of the FM/S superlattice is, generally, the result of an intricate competition of four different LOFF states (Figs. 1, 2).

The calculations lead to the usual Abrikosov–Gor'kov-type equation for the reduced superconducting transition temperature $t = T_c/T_{cs}$ of the FM/S superlattice:

$$\ln t = \Psi\left(\frac{1}{2}\right) - \mathrm{Re}\,\Psi\left(\frac{1}{2} + \frac{D_s k_s^2}{4\pi T_{cs} t}\right), \tag{7}$$

where $\Psi(x)$ is the digamma function and the pair-breaking parameter $D_s k_s^2$ is the solution of another transcendental equation [of its own type for each of the four phases (6)]. For the 00 phase, this equation reads

$$D_s k_s^{00} \tan(k_s^{00} d_s/2) = \frac{\sigma_s v_s}{4 - (\sigma_s v_f n_{sf}/D_f(I) k_f)\cot(k_f d_f/2)}. \tag{8}$$

For $2I\tau_f < 1$ and $I \gg \pi T_{cs}$, the wavenumber k_f is given by the expression

$$k_f^2 = -\frac{2iI}{D_f(I)} = -\frac{2iI(1 + 2iI\tau_f)}{D_f}. \tag{9}$$

For $2I\tau_f > 1$, D_f in Eqs. (8) and (9) should be replaced by $3D_f$.

To find the critical temperature for the 0π state, Eqs. (7)–(9) should be supplemented by the following relationship between $k_s^{0\pi}$ and k_s^{00}:

$$(k_s^{0\pi})^2 - 2\,\mathrm{Re}[k_s^{00}\tan(k_s^{00} d_s/2)]\, k_s^{0\pi}\cot(k_s^{0\pi} d_s) = \left|k_s^{00}\tan(k_s^{00} d_s/2)\right|^2. \tag{10}$$

The transcendental equation for the pair-breaking factor in the π0 state is obtained from Eq. (8) through replacing k_s^{00} by $k_s^{\pi 0}$ on its left-hand side and $\cot(k_f d_f/2)$ by $-\tan(k_f d_f/2)$ on its right-hand side. The relationship between $k_s^{\pi 0}$ and $k_s^{\pi\pi}$, which is required for calculating the critical temperature in the ππ state, is obtained from Eq. (10) through replacing k_s^{00} by $k_s^{\pi 0}$ and $k_s^{0\pi}$ by $k_s^{\pi\pi}$.

The set of Eqs. (7)–(10) can be used to study the dependence of the reduced critical temperature t of the FM/S superlattice on the reduced thicknesses of superconducting (d_s/ξ_{s0}) and magnetic (d_f/a_f) interlayers for different ratios between the parameters σ_s, $2I\tau_f = l_f/a_f$, n_{sf}, and l_s/ξ_{s0}, where ξ_{s0} is the BCS coherence length, $l_{s(f)}$ is the mean free path in the S(FM) layer, and $a_f = v_f/2I$ is the spin stiffness length.

In Fig. 1, a set of phase diagrams $t(d_s)$ is presented for superlattices with different thicknesses of the FM layers and reasonable values of the remaining parameters. As expected, in the range of d_s thicknesses smaller than the threshold value d_s^π, the AFS 0π and ππ LOFF states (curves *b* and *d*) with the antiparallel orientations of magnetizations in the neighboring FM layers are energetically more favorable than the known FS 00 and π0 states (curves *a* and *c*). The threshold thickness d_s^π below which the π-magnetic phases dominate in the FM/S superlattices depends on the other parameters of the theory and varies in the range from $0.6\xi_{s0}$ to $0.85\xi_{s0}$. It is also important that the critical thickness d_s^c of superconducting layers for which T_c goes to zero is always lower for the AFS states than for the FS states; i.e., $d_s^c(\mathrm{AFS}) < d_s^c(\mathrm{FS})$, where $d_s^c(\mathrm{AFS}) = \min\{d_s^c(0\pi),$

$d_s^c(\pi\pi)\}$ and $d_s^c(\mathrm{FS}) = \min\{d_s^c(00),\ d_s^c(\pi 0)\}$. Thus, superconductivity of the superlattices with thicknesses of superconducting layers $d_s^c(\mathrm{AFS}) < d_s < d_s^\pi$ has a purely AFS nature. One can see from Fig. 1 that this range is rather broad for the parameters chosen and may exceed $0.3\xi_{s0}$. Besides, the difference $T_c(\mathrm{AFS}) - T_c(\mathrm{FS})$ between the critical temperatures may become appreciable for certain d_s thicknesses from this range. For instance, this difference exceeds $0.3T_{cs}$ for $T_c(\mathrm{FS}) \approx 0$. The competition between the AFS 0π and ππ states themselves (curves *b* and *d* in Fig. 1) at different thicknesses d_f of the FM layers is also noteworthy. It gives evidence that the nature of the $T_c(d_f)$ oscillations at $d_s < d_s^\pi$ is associated with the 0π–ππ–0π cascade of phase transitions between the new AFS LOFF states (Fig. 2).

As the S-layer thickness increases, the gain due to a partial compensation for the paramagnetic effect of exchange field in the AFS state diminishes and becomes negligible at $d_s > d_s^\pi$. In this case, the symmetric FS 00 and π0 solutions with smaller Cooper-pair flux through the S/FM boundaries have a slightly higher critical temperature than in the 0π and ππ LOFF states. However, the difference between $T_c(\mathrm{AFS})$ and $T_c(\mathrm{FS})$ at thicknesses $d_s > d_s^\pi$ is quite insignificant and can hardly be detected experimentally. It is most likely that in this thickness range the FM/S superlattice is magnetically quasi-two-dimensional, i.e., decomposes into the system of S/FM/S sandwiches for which the correlation between the phases of magnetic order parameter in the neighboring FM layers is absent. At the same time, in this case the 0- or π-type phase matching is retained for the superconducting order parameters in the neighboring S layers. Because of this, the nonmonotonic behavior of $T_c(d_f)$ at large S-layer thicknesses ($d_s > d_s^\pi$) is expected to be due to another transition chain 00–π0–00, as was previously shown in [3–7].

Our analysis of Fig. 1 shows that the range of d_s thicknesses where the differences in the critical temperatures of all four superlattice states are the greatest is physically the most interesting. For this reason, the $t(d_f)$ dependences in Fig. 2 are presented for the S-layer thickness $d_s = 0.52\xi_{s0}$ corresponding to the indicated interval and the same set of remaining parameters as in Fig. 1. It is seen in Fig. 2 that curves *b* and *d* for the AFS 0π and ππ states go markedly higher than the FS 00 and π0 states (curves *a* and *c*) and fully suppress the realization of the latter. Consequently, the appearance of new AFS 0π and ππ LOFF states prevents the T_c going to zero and noticeably extends the areas of superconducting regions in the phase diagrams in Figs. 1 and 2.

Interestingly, Figs. 1 and 2 are also suited to the analysis of the $T_c(d_s)$ and $T_c(d_f)$ phase diagrams of the three-layer structures FM/S/FM in which the π-phase superconductivity is basically impossible. To this end,

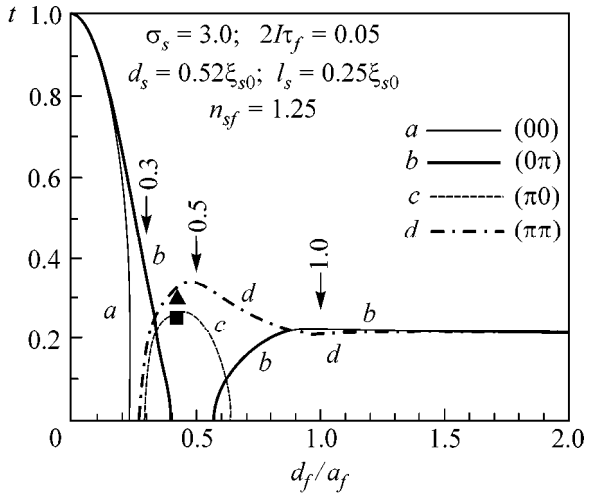

Fig. 2. Reduced critical temperature t of the multilayer FM/S system vs. reduced thickness d_f/a_f of the FM layer for $d_s = 0.52\xi_{s0}$. The vertical arrows indicate the d_f thicknesses for which the phase diagrams are drawn in Fig. 1.

one has only to remove the *c* (π0) and *d* (ππ) curves from these figures and replace d_f by $2d_f$. Thus, the three-layer FM/S/FM systems discussed in [11, 12] are a particular case of our theory. Moreover, it was assumed in the cited works that T_c in the AFS state is higher than in the FS state for any S-layer thickness d_s, although the estimates for the $T_c(d_s)$ dependence were made only in the Cooper limit ($d_s \ll \xi_s$). We have shown above that the AFS state dominates only at d_s values below the threshold value d_s^π (Fig. 1). In the opposite case, the critical temperature of the FS state becomes higher. Recall that in our case $d_s \geq d_s^c \approx 0.4\xi_{s0} > \xi_s \approx \approx 0.3\xi_{s0}$.

To obtain the $T_c(d_s)$ and $T_c(d_f)$ phase diagrams for the S/FM/S trilayers in which the π-phase magnetism is impossible, one has to remove curves *b* (0π) and *d* (ππ) from Figs. 1 and 2 and replace d_s by $2d_s$. The resulting $T_c(d_f)$ phase diagram with curves *a* (00) and *c* (π0) corresponds to reentrant superconductivity.

The simplest structure allowing the competition between the 0- and π-phase magnetism and the 0- and π-phase superconductivity in a common sample is provided by a four-layer FM/S/FM/S system, whose phase diagrams are analogous to the ones shown in Figs. 1 and 2 for superlattices. Simultaneous examination of the phase diagrams $T_c(d_s)$ in Fig. 1 and $T_c(d_f)$ in Fig. 2 allows one to optimize the choice of parameters for the four-layer structure, making possible the control of its superconducting and magnetic states, e.g., by using a weak external magnetic field. To reorient the magnetizations of the neighboring FM layers from the antiferromagnetic state to the ferromagnetic state, magnetic fields H must be higher than the FM coercive field H_{coer}.

The corresponding fields ($H_{coer} \sim 10$–100 Oe; see, e.g., [13]) are too weak to strongly modify phase diagrams of the FM/S/FM/S structures possessing two data-record channels simultaneously, namely, on the superconducting current and on the magnetic order. In particular, it follows from Fig. 2 that, if the operating point is chosen beneath curve d (e.g., $t \approx 0.3$ and $d_f \approx 0.45a_f$; black triangle), the field $H > H_{coer}$ will drive the system from the AFS($\pi\pi$) state immediately to the ferromagnetic normal (FN) state, thus making the superconducting current resistive. Switching-off of this field returns the system to the initial AFS state. In this regime, the four-layer FM/S/FM/S system operates as a device with 100% negative magnetoresistance. This is reminiscent of a "spin switch" model based on the FM/S/FM trilayers that was suggested in [11, 12]. However, the three-layer FM/S/FM structure possesses considerably fewer logically different variants of data record than the four-layer FM/S/FM/S structures (see below).

In particular, if the magnetization orientation in the first FM layer is fixed, e.g., by virtue of pinning at the contact with a magnetic dielectric, then one may drive the four-layer structure from the AFS to the antiferromagnetic normal (AFN) state upon applying a field H (higher than the upper critical field H_{c2}) in the opposite direction. In this case, only that information changes which was recorded on the superconducting current, whereas the information recorded on the mutual orientation of magnetizations of the FM layers will be retained. Note that by the appropriate choice of the operating point about the superconducting transition curve $T_c(d_f)$ in Fig. 2 one can always attain the desired magnitude of the H_{c2} field to make it lower than the depinning field H_p. An additional AFN $\longrightarrow$ FN transition occurs in the FM/S/FM/S system upon applying a field $H > H_p$.

At the same time, according to the theory of second-order phase transitions, the system under these conditions will be in the state with lower free energy (higher critical temperature). For this reason, if the operating point is chosen under curve c ($t \approx 0.25$ and $d_f \approx 0.45a_f$; black square), then the field H of the appropriate magnitude and direction will induce the AFS($\pi\pi$) $\longrightarrow$ FS(π0) transition and change the magnetic information but retain the information recorded on the superconducting current. As the field rises to a value higher than H_{c2} in the FS(π0) state, the FM/S/FM/S structure undergoes transition to the FN state. The above-mentioned AFS($\pi\pi$) $\longrightarrow$ AFN $\longrightarrow$ FN chain of transitions occurs upon applying the oppositely oriented fields first higher than H_{c2} and then higher than H_p. Switching-off of the external fields again returns the system to the initial AFS($\pi\pi$) state.

Thus, the FM/S superlattices can serve as elements in the design of microelectronic devices of a basically new type combining advantages of the superconducting and magnetic data-record channels in a *common* sample. It should be emphasized that the range of parameters providing pronounced π-phase magnetism is rather narrow. In particular, the $|t(\mathrm{AFS}) - t(\mathrm{FS})|$ difference becomes less than 0.02 for $2I\tau_f \gg 0.1$ and n_{sf} on the order of unity or less; i.e., the π-magnetic and 0-magnetic states of the FM/S superlattice become practically indistinguishable. The knowledge of a physically important range of parameters where the competition between the AFS and FS LOFF states (Fig. 2) results in a multicritical behavior of the $T_c(d_f)$ phase diagrams can be helpful in developing the technology of FM/S superlattices with new π-magnetic properties.

This work was supported in part (M. Khusainov and Yu. Proshin) by the Russian Foundation for Basic Research (project nos. 01-02-17534 and 01-02-17822) and the CRDF (grant no. REC-007).

REFERENCES

1. J. S. Jiang, D. Davidović, D. H. Reich, *et al.*, Phys. Rev. Lett. **74**, 314 (1995).
2. Y. Obi, V. Ikebe, T. Kubo, *et al.*, Physica C (Amsterdam) **317–318**, 149 (1999).
3. Z. Radović, M. Ledvij, L. Dobrosavljević-Grujić, *et al.*, Phys. Rev. B **44**, 759 (1991).
4. A. I. Buzdin, B. Bujićić, and M. Yu. Kupriyanov, Zh. Éksp. Teor. Fiz. **101**, 231 (1992) [Sov. Phys. JETP **74**, 124 (1992)].
5. M. G. Khusainov and Yu. N. Proshin, Phys. Rev. B **56**, R14 283 (1997); **62**, 6832 (2000).
6. Yu. N. Proshin and M. G. Khusainov, Pis'ma Zh. Éksp. Teor. Fiz. **66**, 527 (1997) [JETP Lett. **66**, 562 (1997)].
7. Yu. N. Proshin and M. G. Khusainov, Zh. Éksp. Teor. Fiz. **113**, 1708 (1998) [JETP **86**, 930 (1998)]; Zh. Éksp. Teor. Fiz. **116**, 1882 (1999) [JETP **89**, 1021 (1999)].
8. M. G. Khusainov, Pis'ma Zh. Éksp. Teor. Fiz. **61**, 947 (1995) [JETP Lett. **61**, 972 (1995)].
9. M. G. Khusainov, Zh. Éksp. Teor. Fiz. **109**, 524 (1996) [JETP **82**, 278 (1996)].
10. M. G. Khusainov, Zh. Éksp. Teor. Fiz. **110**, 966 (1996) [JETP **83**, 533 (1996)].
11. A. I. Buzdin, A. V. Vedyayev, and N. V. Ryzhanova, Europhys. Lett. **48**, 686 (1999).
12. L. R. Tagirov, Phys. Rev. Lett. **83**, 2058 (1999).
13. Ch. Kittel, *Introduction to Solid State Physics* (Wiley, New York, 1976; Nauka, Moscow, 1978).

Translated by V. Sakun

JETP Letters, Vol. 73, No. 7, 2001, pp. 349–351. Translated from Pis'ma v Zhurnal Éksperimental'noĭ i Teoreticheskoĭ Fiziki, Vol. 73, No. 7, 2001, pp. 392–395.

Phase Transition in Electronic Manganite $Ca_{0.85}Sm_{0.15}MnO_3$

A. N. Vasil'ev, T. N. Voloshok, and R. Suryanarayanan*

Moscow State University, Vorob'evy gory, Moscow, 119899 Russia

** University Paris-Sud, 91405 Orsay, France*

Received February 26, 2001

The resistivity, the magnetic susceptibility, the magnetization, and the specific heat of electronic manganite $Ca_{0.85}Sm_{0.15}MnO_3$ were studied. The data obtained suggest that this compound undergoes phase transition into the insulator antiferromagnetic state at $T_c \sim 115$ K and displays negative magnetoresistance at $T < T_c$. A minor ferromagnetic component of $0.025\mu_B$ in the magnetization of $Ca_{0.85}Sm_{0.15}MnO_3$ may be caused by the deviation of this composition from the exact stoichiometry $Mn^{3+} : Mn^{4+} = 1 : 8$. The Debye temperature $\Theta_D = 575$ K and the entropy of phase transition $\Delta S = 5.1$ J/(mol K) were derived from the temperature dependence of specific heat. © *2001 MAIK "Nauka/Interperiodica".*

PACS numbers: 75.30.Kz; 75.30.Vn; 75.30.Cr; 75.60.E; 75.40.Cx

Perovskite-like manganites $A_{1-x}B_xMnO_3$, where A is tervalent lanthanide and B is bivalent alkaline-earth metal, attract interest as materials with colossal negative magnetoresistance. The ratio between A and B cations determines the $Mn^{3+} : Mn^{4+}$ ratio in the structure of these compounds. Electronic manganites ($x > 0.5$) with predominating Mn^{4+} have been studied much less thoroughly than hole manganites with predominating Mn^{3+} ($x < 0.5$). Nevertheless, they are of considerable interest because the phase diagrams of hole and electronic manganites are qualitatively different [1, 2]. For instance, $La_{1-x}Ca_xMnO_3$ exhibits a broad region of compositions $0.18 \le x < 0.5$, where the system undergoes transition into the metallic ferromagnetic state upon lowering temperature. Hole manganites display colossal magnetoresistance precisely in this phase. In the electronic manganite $Ca_{1-x}Sm_xMnO_3$, the metallic ferromagnetic state occurs for none of the x values and the colossal magnetoresistance effect is observed only in a narrow range of compositions near $x \sim 0.15$.

The studies of the structure and the transport and magnetic properties of $Ca_{0.85}Sm_{0.15}MnO_3$ were initiated in [3–5]. At high temperatures, this compound has the orthorhombic *Pnma* lattice with parameters $a = 5.3215$ Å, $b = 7.5010$ Å, and $c = 5.3021$ Å ($T = 300$ K). With lowering temperature, $Ca_{0.85}Sm_{0.15}MnO_3$ undergoes first-order phase transition into the monoclinic $P2_1/m$ modification with parameters $a = 5.3340$ Å, $b = 7.4432$ Å, $c = 5.3076$ Å, and $\beta = 91.062°$ ($T = 10$ K). During this transition, the high- and low-temperature phases of $Ca_{0.85}Sm_{0.15}MnO_3$ coexist in a certain temperature range, and in each of them its own antiferromagnetic order is established with lowering temperature. Simultaneously with the formation of the $P2_1/m$ phase, a *C*-type magnetic structure appears in it at $T \sim 125$ K [6]. The *c*-directed ferromagnetic Ising chains in this structure are coupled with each other via the antiferromagnetic interaction. In the supercooled *Pnma* phase, the antiferromagnetic *G*-type state [6] typical of $CaMnO_3$ is formed at $T \sim 115$ K.

Magnetization measurements systematically indicate the presence of a compositionally dependent ferromagnetic moment in $Ca_{1-x}Sm_xMnO_3$ ($x \le 0.15$) at low temperatures. In $Ca_{0.85}Sm_{0.15}MnO_3$, this moment is equal to approximately $0.015\mu_B$ per formula unit in weak magnetic fields [5]. There are different guesses in the literature as to the origin of the ferromagnetic component [3, 5]. According to [3], ferromagnetism is caused by the canting of antiferromagnetic *G* phase that remains in the *Pnma* clusters down to low temperatures. It is conjectured in [5] that both insulator antiferromagnetic and conducting ferromagnetic states may form in the *Pnma* clusters.

A wealth of proposed structural and magnetic states in $Ca_{0.85}Sm_{0.15}MnO_3$ has stimulated this work, in which the measured specific heat is compared with the results of our measurements of magnetization, magnetic susceptibility, and resistivity of this compound.

$Ca_{0.85}Sm_{0.15}MnO_3$ ceramic was prepared by solid-phase synthesis from the nominal Sm_2O_3, MnO_2, and $CaCO_3$ composition. A powder-pressed pellet was repeatedly ground and annealed at temperatures gradually increasing in the range 980–1200°C. The final synthesis was conducted in air atmosphere at 1300°C for 36 h followed by cooling in a furnace. The homogeneity of the sample and the correspondence of its cationic composition to the nominal composition were confirmed by X-ray powder diffraction at $T = 300$ K and by local X-ray spectrum analysis. The physical properties of $Ca_{0.85}Sm_{0.15}MnO_3$ were measured over the tempera-

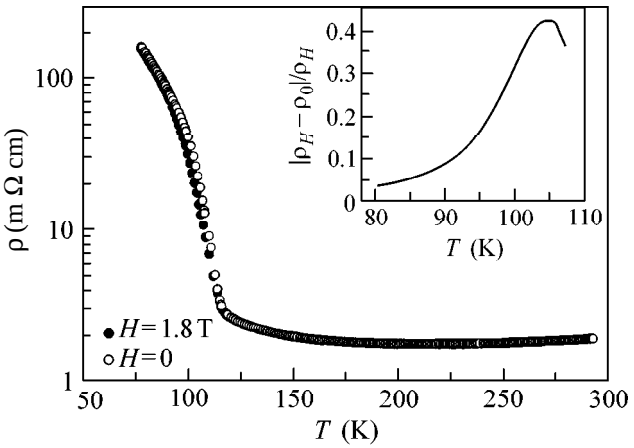

Fig. 1. Temperature dependences of the resistivity of $Ca_{0.85}Sm_{0.15}MnO_3$ in zero magnetic field and in the field $H = 1.8$ T. Temperature dependence of the negative magnetoresistance is shown in the inset.

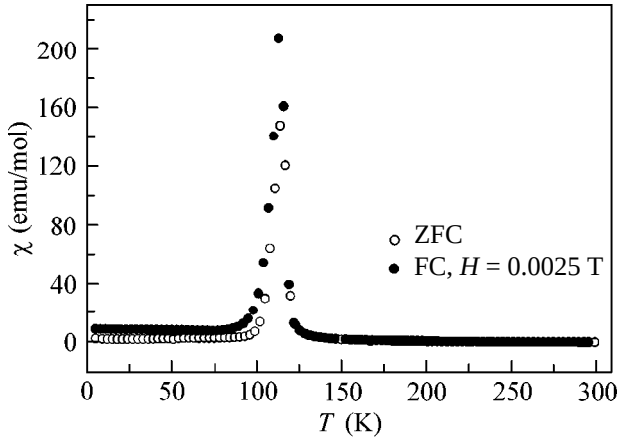

Fig. 2. Temperature dependences of the magnetic susceptibility of $Ca_{0.85}Sm_{0.15}MnO_3$, as measured in the zero-field-cooling (ZFC) and field-cooling (FC; $H = 0.0025$ T) regimes.

ture range 5–300 K. The magnetization and magnetic susceptibility were measured by a SQUID magnetometer (Quantum Design) in fields of up to 5 T. The resistivity was measured by the standard four-probe technique. The specific heat was measured using a quasi-adiabatic microcalorimeter by the heat pulse technique.

The temperature dependences of the resistivity ρ of the ceramic sample of $Ca_{0.85}Sm_{0.15}MnO_3$ in zero field and in field $H = 1.8$ T are shown in Fig. 1. At high temperatures, the resistivity displays a weak metallic behavior and sharply rises at $T_c \sim 115$ K, indicating the transition into the insulator state. At $T < T_c$, the magnetoresistance is negative; its magnitude in the field $H = 1.8$ T at $T = 105$ K equals $|\rho_H - \rho_0|/\rho_H = 40\%$. In the range of magnetic fields studied in this work, the magnitude of negative magnetoresistance of $Ca_{0.85}Sm_{0.15}MnO_3$ is comparatively small, although in fields ~7 T it reaches values typical of hole manganites [3, 6].

The temperature dependences of the magnetic susceptibility of $Ca_{0.85}Sm_{0.15}MnO_3$ were measured in the zero-field-cooling (ZFC) and field-cooling (FC; $H = 0.0025$ T) regimes (Fig. 2). The $\chi(T)$ curves show a peak at $T_c \sim 115$ K. At $T < T_c$, the FC susceptibility markedly exceeds the ZFC one. These features of magnetic susceptibility are typical of the systems undergoing transition into the spin (or cluster) glass state. However, for $Ca_{0.85}Sm_{0.15}MnO_3$, this state is quite specific. As seen from the field dependence of magnetization M shown in Fig. 3, there is a ferromagnetic component of about $0.025\mu_B$ in weak fields and M grows linearly with the field and reaches $0.09\mu_B$ at $H = 5$ T. The $M(H)$ curve shows a weak hysteresis in the entire range of magnetic fields studied. The appearance of a small ferromagnetic component in the magnetization of $Ca_{0.85}Sm_{0.15}MnO_3$ at low temperatures may be due to the deviation of the composition from a composition with $Mn^{3+} : Mn^{4+} = 1 : 8$. For this ratio, the Mn^{3+} and Mn^{4+} positions may be ordered to form the antiferromagnetic structure. The magnetic moments of the Mn^{3+} and Mn^{4+} ions are $\mu_{Mn^{3+}} = 4.9\mu_B$ and $\mu_{Mn^{4+}} = 3.9\mu_B$, respectively. For the composition with 2.5% excess Mn^{3+} ions, the uncompensated ferromagnetic moment is $M = 0.025(\mu_{Mn^{3+}} - \mu_{Mn^{4+}}) = 0.025\mu_B$.

The temperature dependence of the specific heat of $Ca_{0.15}Sm_{0.85}MnO_3$ is presented in Fig. 4. A clearly defined λ-type anomaly confirms the presence of phase transition at $T_c \sim 115$ K.

Generally, the specific heat of a magnet contains at $T < T_c$ the phonon C_{ph}, the electronic C_{el}, and the magnon C_{mag} components:

$$C = C_{ph} + C_{el} + C_{mag}.$$

At low temperatures, the lattice contribution is $C_{ph} = \beta T^3 + \alpha T^5$, the electronic contribution is $C_{el} = \gamma T$, and the contribution of spin excitations is $C_{mag} = \delta T^n$. The exponent n depends on the type of spin excitations; $n = 3/2$ or 3 for the magnons in a three-dimensional ferromagnet or antiferromagnet, respectively [7].

The fact that the linear electronic contribution to the specific heat was not observed indicates that the low-temperature state of the sample is dielectric. No contribution proportional to $T^{3/2}$ was revealed in the specific heat of $Ca_{0.85}Sm_{0.15}MnO_3$ either, in compliance with the smallness of the ferromagnetic component in the magnetization of this compound at low temperatures. The sum $(\beta + \delta)T^3 + \alpha T^5$ with parameters $\beta + \delta = (5.0 \pm 0.3) \times 10^{-5}$ J/(mol K^4) and $\alpha = (3.7 \pm 0.3) \times 10^{-7}$ J/(mol K^6) is the best fit to the experimental data in the temperature range 7–12 K. The magnon component δT^3 of the specific heat of a three-dimensional antiferromagnet and

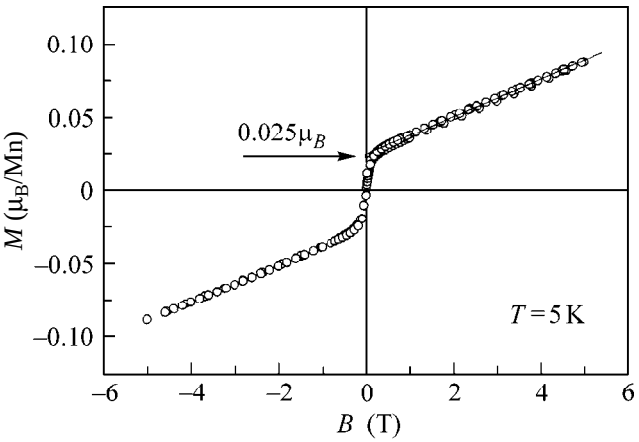

Fig. 3. Field dependence of the magnetization of $Ca_{0.85}Sm_{0.15}MnO_3$ at T = 5 K.

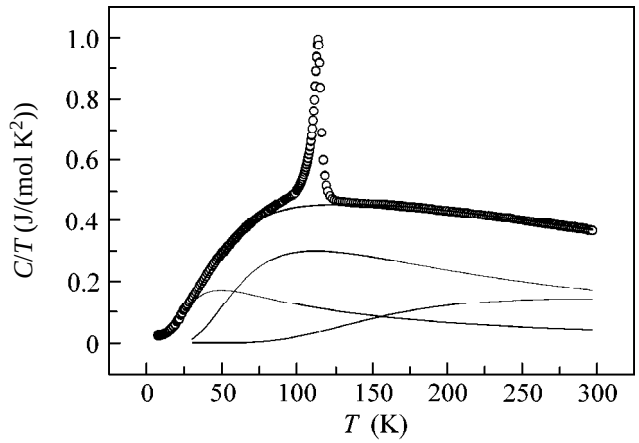

Fig. 4. Temperature dependence of the specific heat of $Ca_{0.85}Sm_{0.15}MnO_3$. Solid line is the approximation of phonon contribution by the sum of three Einstein modes.

the phonon component βT^3 are additive. Using the formula $\beta = 12\pi^4 R\nu/5\Theta_D^3$, where R is the universal gas constant and $\nu = 5$ is the number of atoms in formula unit [8], the lower bound to the Debye temperature was estimated at $\Theta_D \sim 575$ K. This value agrees rather well with the results of systematic studies of the parameters of Ca-containing manganites. For instance, Θ_D in the $La_{1-x}Ca_xMnO_3$ system increases from 368 K in $La_{0.9}Ca_{0.1}MnO_3$ [9] to 500 K in $La_{0.37}Ca_{0.63}MnO_3$ [10].

Excluding the phase transition region, the specific heat of the sample studied can be approximated by three Einstein optical modes $\hbar\omega_{E1}/k_B$ = 130 K, $\hbar\omega_{E2}/k_B$ = 290 K, and $\hbar\omega_{E3}/k_B$ = 760 K over a wide temperature range. As shown in Fig. 4, this allows the entropy of phase transition to be estimated at ΔS = 5.1 J/(mol K). The theoretical estimate of magnetic contribution to the entropy of phase transition $\Delta S_{mag} = R\ln(2S + 1) = 8.314(0.15\ln5 + 0.85\ln4) = 11.8$ J/(mol K) markedly exceeds this value. However, it should be noted that the procedure of setting off the entropy of phase transition is highly sensitive to the interval where the Einstein approximation is used. The agreement between the experiment and theory betters if the magnetic entropy released in the pretransition fluctuation region is included in ΔS.

In our measurements of the transport, magnetic, and notably thermal properties, clear-cut anomalies are observed for $Ca_{0.85}Sm_{0.15}MnO_3$ only at the temperature T_c = 115 K. The obvious contradiction with the results of studies [2, 3, 5], where several phase transitions were observed at close temperatures, is probably caused by the fact that the experiments were conducted at different rates. Different structures and magnetic phases of $Ca_{0.85}Sm_{0.15}MnO_3$ are energetically close to one another, so that the system undergoes transition into the phase-separated state of the cluster-glass type upon fast cooling [5]. Under quasi-adiabatic conditions, the system with a multiwell potential can transfer to the lowest energy state. Under these conditions, a nearly homogeneous antiferromagnetic state with a small fraction of ferromagnetic clusters is likely formed at low temperatures. The applied magnetic field lowers the energy of the ferromagnetic state at low temperatures, leading to an increase in the volume of ferromagnetic clusters over which electron transport is possible.

This work was supported by the Russian Foundation for Basic Research (project no. 99-02-17828), the INTAS (grant no. 99-0155), and the NWO (grant no. 047-008-012).

REFERENCES

1. P. Schiffer, A. P. Ramírez, W. Bao, and S.-W. Cheong, Phys. Rev. Lett. **75**, 3336 (1995).
2. C. Martin, A. Maignan, M. Hervieu, and B. Raveau, Phys. Rev. B **60**, 12 191 (1999).
3. C. Martin, A. Maignan, M. Hervieu, *et al.*, J. Magn. Magn. Mater. **205**, 184 (1999).
4. C. Martin, A. Maignan, F. Damay, *et al.*, J. Solid State Chem. **134**, 198 (1997).
5. R. Mahendiran, A. Maignan, C. Martin, *et al.*, Phys. Rev. B **62**, 11 644 (2000).
6. V. M. Loktev and Yu. G. Pogorelov, Fiz. Nizk. Temp. **26**, 1 (2000) [Low Temp. Phys. **26**, 171 (2000)].
7. A. I. Akhiezer, V. G. Bar'yakhtar, and S. V. Peletminskii, *Spin Waves* (Nauka, Moscow, 1967; North-Holland, Amsterdam, 1968).
8. E. S. R. Gopal, *Specific Heat at Low Temperatures* (Plenum, New York, 1966).
9. L. Ghivelder, I. Abrego Castillo, N. McN. Alford, *et al.*, J. Magn. Magn. Mater. **189**, 274 (1998).
10. P. Schiffer, A. P. Ramírez, S.-W. Cheong, *et al.*, Phys. Rev. Lett. **76**, 3188 (1996).

Translated by V. Sakun

JETP Letters, Vol. 73, No. 7, 2001, pp. 352–356. Translated from Pis'ma v Zhurnal Éksperimental'noĭ i Teoreticheskoĭ Fiziki, Vol. 73, No. 7, 2001, pp. 396–400.

Low-Temperature Ferromagnetism in a New Diluted Magnetic Semiconductor $Bi_{2-x}Fe_xTe_3$

V. A. Kul'bachinskiĭ*, A. Yu. Kaminskiĭ*, K. Kindo, Y. Narumi**, K. Suga**, P. Lostak***, and P. Svanda*****

** Moscow State University, Vorob'evy gory, Moscow, 119899 Russia*

*** Osaka University, 560-8531 Osaka, Japan*

**** Pardubice University, 53210 Pardubice, Czech Republic*

Received February 26, 2001

Single crystals of a new diluted magnetic semiconductor $Bi_{2-x}Fe_xTe_3$ ($0 \le x \le 0.08$) were grown. For all crystals, the transition into a ferromagnetic state with easy axis parallel to the C_3 axis was observed at temperature T_c increasing with iron concentration and reaching 12 K at $x = 0.08$. An increase in the Seebeck coefficient, anomalous Hall effect, and resistivity jump at $T = T_c$ were also observed. The frequency of the de Haas–van Alphen oscillations decreases with increasing x, indicating the donor properties of Fe. © *2001 MAIK "Nauka/Interperiodica".*

PACS numbers: 75.40.-s; 75.30.Kz; 75.50.Pp

1. Semiconductors containing transition or rare-earth ions in an amount excluding direct exchange interaction between their magnetic moments are referred to as diluted magnetic semiconductors (DMS). The rare-earth and transition-metal chalcogenide DMS are most thoroughly studied [1]. The exchange interaction between free charge carriers and the localized magnetic moments of ions strongly affects the optical, transport, and magnetic properties of host semiconductors. As a rule, DMS materials undergo transition into the spin-glass state upon lowering temperature [2, 3]. For example, the solubility limit for magnetic impurities in III–V semiconductors, e.g., InAs or GaAs, is very low, $\sim 10^{19}$ cm^{-3}. For this reason, the corresponding DMS can be prepared only as thin layers under non-equilibrium conditions of molecular beam epitaxy at low growth temperatures and a considerable excess over the solubility limit. Earlier, partial ferromagnetism was observed at low temperatures [5] in uniform III–V (In, Mn)As films grown on a GaAs substrate [4]. Ferromagnetism was also observed in (Ga, Mn)As films [6] and in Group IV–VI PbSnMnTe DMS [7].

Ferromagnetism in DMS is induced by free charge carriers because the direct exchange interaction between the localized magnetic moments in DMS is absent. It is not only of a scientific interest but is also practically important because it offers strong possibilities of using a magnetic field for the control of properties of various devices [8]. From this point of view, of special interest are thermoelectric compounds, especially those based on Bi_2Te_3, Sb_2Te_3, and related mixed crystals, because they are the most efficient currently available thermoelectric materials. To date, magnetic thermoelectric materials based on bismuth and antimony tellurides or selenides, as well as their magnetic and electronic properties, have not been studied.

2. Bi_2Te_3 is a layered narrow-gap semiconductor ($E_g = 0.20$ eV at room temperature [9]) with the rhombohedral symmetry of the crystal lattice belonging to the space group R_{3m}–D_{3d}^5 with twofold axis C_2 and threefold axis C_3 (perpendicular to the layers). Five-layer packages Te^1–Bi–Te^2–Bi–Te^1 (Te^1 and Te^2 denote two possible tellurium sites in the lattice) with strong mostly covalent–ionic bonds form the bismuth telluride lattice. The five-layer packages interact with each other through weak van der Waals forces.

Stoichiometric Bi_2Te_3 crystals always grow in the p type and have high hole concentration because of the presence of a considerable amount of negatively charged antisite point defects; i.e., many of the Te lattice sites are occupied by the Bi atoms. The doping primarily changes the bond polarity and, hence, the number of antisite defects. Therefore, any element can function as a donor or acceptor irrespective of its Group number. For example, Group III element indium functions as a donor in V_2– VI_3 semiconductor Bi_2Te_3 [10].

3. Single crystals of Group V_2–VI_3 DMS, specifically, of p-$Bi_{2-x}Fe_xTe_3$ grown by the Bridgman method, were studied in this work. Magnetic susceptibility, magnetic moment, Hall effect, and temperature dependence of resistance were studied over the temperature range 2–300 K; the Seebeck coefficient was also measured.

0021-3640/01/7307-0352$21.00

Samples were prepared from elements of 99.999% purity. A Fe_2Te_3 polycrystal was synthesized and then mixed with the Bi and Te elements in a ratio of $Bi_{2-x}Fe_xTe_3$ with x = 0, 0.005, 0.04, and 0.08, after which a single crystal was grown by the Bridgman method. The 3 × 0.8 × 0.8-mm samples for magnetic and transport measurements were cut from an ingot by the electric-spark method.

The magnetic susceptibility and the magnetic moment were measured over the temperature range 2–300 K in a magnetic field of up to 7 T using an MPSL-XL7L SQUID magnetometer (Quantum Design Co. Ltd.).

4. Magnetic susceptibility χ of the Bi_2Te_3 single crystals points to their diamagnetism over the whole temperature range from 2 to 300 K. It does not depend on the temperature and is $\chi_{C_3} = -0.45 \times 10^{-6}$ emu/g along the C_3 axis, i.e., perpendicular to the layers, and $\chi_{C_2} = -0.33 \times 10^{-6}$ emu/g along the C_2 axis. In the iron-doped sample, the magnetic susceptibility increases with lowering temperature from room to 2 K and becomes positive with a maximum value of $\chi_{C_3} \approx 2.5 \times 10^{-5}$ emu/g along the C_3 axis in the x = 0.08 sample.

At liquid helium temperatures and $B \parallel C_3$, the magnetic moment vs. magnetic field curve exhibits a hysteresis loop typical of ferromagnets. The loop width increases as the iron content in $Bi_{2-x}Fe_xTe_3$ grows (Fig. 1). It also depends on the crystallographic orientation. Figure 2 shows the field dependences of magnetic moment for B directed along the C_2 axis. A comparison of Figs. 1 and 2 indicates that the hysteresis loop is much smaller for the field aligned with the C_2 axis. In addition, the oscillations due to the de Haas–van Alphen effect are clearly visible in Figs. 1 and 2 at $B > 2$ T.

The temperature dependences of the susceptibility χ along the C_3 axis upon heating in the field B = 1 mT are shown in Fig. 3. Prior to these measurements, a magnetic field of 1 T was applied at T = 2 K, and only after this were the samples heated at B = 1 mT. In this case, the Curie temperature T_c of transition into the ferromagnetic state is very close to the temperature where the susceptibility becomes zero [7]. This gave $T_c \approx 5$ K (x = 0.005), ≈8 K (x = 0.04), and ≈12 K (x = 0.08). At temperature T_c, the resistivity undergoes a reversible jump (inset in Fig. 3) caused by switching off the spin-flip scattering after the transition into the ferromagnetic state.

The Hall coefficient as a function of magnetic field is shown in Fig. 4 for the Bi_2Te_3 and $Bi_{1.92}Fe_{0.08}Te_3$ samples. An increase in the Hall coefficient with increasing magnetic field in Bi_2Te_3 is associated with a complex structure of the valence band consisting of two sixfold degenerate extrema (for details, see [10]). With the $Bi_{1.92}Fe_{0.08}Te_3$ sample, this nonmonotonic increase

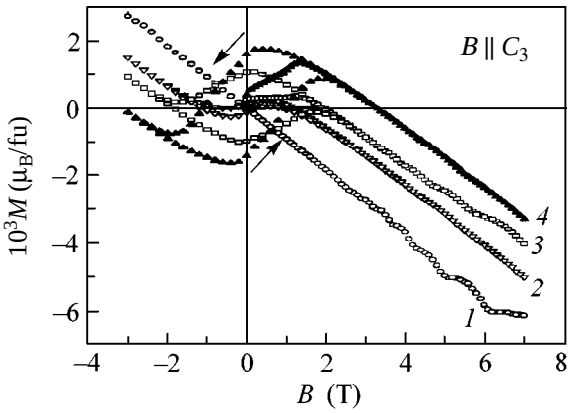

Fig. 1. Magnetization M along the C_3 axis (perpendicular to the layers) as a function of magnetic field at T = 2 K for the $Bi_{2-x}Fe_xTe_3$ samples with x = (*1*) 0, (*2*) 0.005, (*3*) 0.04, and (*4*) 0.08.

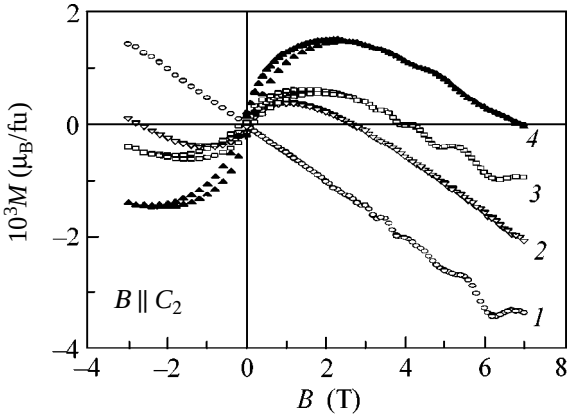

Fig. 2. Magnetization M along the C_2 axis (along the layers) as a function of magnetic field at T = 2 K for the $Bi_{2-x}Fe_xTe_3$ samples with x = (*1*) 0, (*2*) 0.005, (*3*) 0.04, and (*4*) 0.08.

is superimposed by a sharp rise in the Hall coefficient at low magnetic fields because of the appearance of magnetization in the ferromagnetic state of this sample. In other words, the hole interaction with the magnetic moments of iron ions gives rise to the anomalous Hall effect [11], which is due not to the external field but to the sample magnetization M. For the anomalous Hall effect, the Hall resistivity ρ_{xy} is related to the normal R and anomalous R_s Hall coefficients by the formula

$$\rho_{xy} = RH + R_sM. \quad (1)$$

The fact that the Hall coefficient increases with increasing iron concentration in $Bi_{1-x}Fe_xTe_3$ is evidence for the donor properties of Fe. However, the use of the Hall effect for calculating hole concentration p is hampered, for which reason the $p(x)$ dependence was derived from the de Haas–van Alphen oscillations (see below).

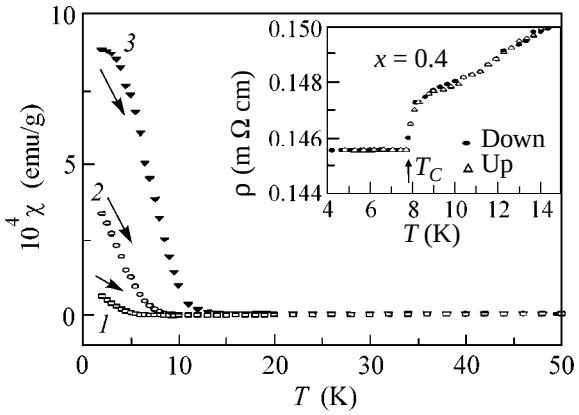

Fig. 3. Temperature dependence of the magnetic susceptibility χ in magnetic field B = 1 mT parallel to the C_3 axis in the region of ferromagnetic transition of the $Bi_{2-x}Fe_xTe_3$ samples with x = (*1*) 0.005, (*2*) 0.04, and (*3*) 0.08. Inset: the reversible resistivity jump observed for the $Bi_{1.96}Fe_{0.04}Te_3$ sample upon the transition into the ferromagnetic state at temperature T_c is indicated by the arrow.

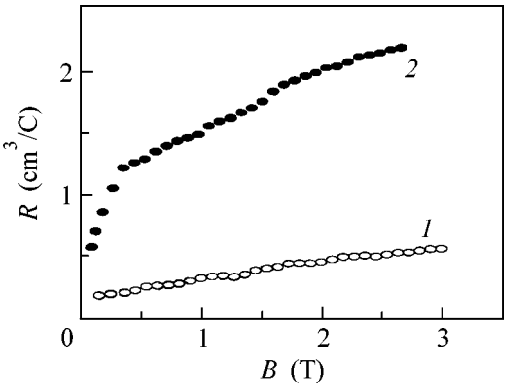

Fig. 4. Magnetic field dependence of the Hall coefficient R for (*1*) the host Bi_2Te_3 sample and (*2*) the $Bi_{1.92}Fe_{0.08}Te_3$ sample.

The Seebeck coefficient α was also measured for all samples at room temperature. It was found that the α value increased from α = 215 μV/K in pure bismuth telluride to α = 260 μV/K in $Bi_{1.92}Fe_{0.08}Te_3$ with maximum Fe content.

All $Bi_{2-x}Fe_xTe_3$ samples studied were of the *p* type. For the *n*-type systems, we chose the Bi_2Se_3 and $Bi_{1.96}Fe_{0.04}Se_3$ compounds because, contrary to Bi_2Te_3, their stoichiometric single crystals always grow in the *n* type. The magnetic susceptibility χ of the *n*-Bi_2Se_3 single crystals displayed a diamagnetic behavior at temperatures from 2 to 300 K. It was found to be temperature-independent and isotropic with $\chi_{C_3} = \chi_{C_2} = -0.3 \times 10^{-6}$ emu/g. The electron concentration increased from $n = 3.7 \times 10^{19}$ cm^{-3} in Bi_2Se_3 to $n = 6 \times 10^{19}$ cm^{-3} in $Bi_{1.96}Fe_{0.04}Se_3$ upon doping with Fe; i.e., iron was a donor, as in bismuth telluride. No ferromagnetic transition was observed down to a temperature of 2 K.

5. We assume that the iron atoms are most probably located in the interstitial sites of the Bi_2Te_3 lattice. This assumption follows from the behavior of lattice parameters in the Bi_2Te_3 samples upon their doping with iron. X-ray lattice parameters of the starting Bi_2Te_3 crystals were found to be a = 0.43821(5) and c = 3.0481(2) nm, whereas, in the $Bi_{2-x}Fe_xTe_3$ (x = 0.08) sample with the highest Fe content (according to atomic adsorption analysis, the iron concentration in this sample was $c_{Fe} = 8.8 \times 10^{19}$ cm^{-3}), these parameters are a = 0.43835(5) and c = 3.0490(2) nm. The c/a ratio remains virtually unchanged. If the iron atoms occupied the van der Waals space between the five-layer packages in the layered structure of bismuth telluride, then the c/a ratio would increase. The dielectric constant of Bi_2Te_3 is very large ($\varepsilon_\infty \approx 80$), and iron is ionized in the lattice; i.e., it is in the ionic form and functions as a donor. As a result, the initial hole concentration diminishes with increasing iron content. These data are also confirmed by the studies of the Seebeck coefficient and by the fact that the de Haas–van Alphen oscillation frequency F decreases from F = 26 T in Bi_2Te_3 to F = 18 T in $Bi_{1.92}Fe_{0.08}Te_3$ as the iron content increases.

6. The hole concentration p, the Fermi energy, and a change in both with doping can be calculated using the de Haas–van Alphen effect. For the ellipsoidal nonparabolic model [12], the dispersion law is written as

$$2m_0E/\hbar^2 = \alpha_{11}k_x^2 + \alpha_{22}k_y^2 + \alpha_{33}k_z^2 + 2\alpha_{23}k_yk_z, \quad (2)$$

where $\alpha_{ij} = m_0/m_{ij}$ are the energy-dependent components of the tensor of reciprocal effective masses and $k_{x,y,z}$ are the wave vector components: k_x is perpendicular to the mirror plane in which the C_2 and C_3 axes lie, k_y is parallel to the C_2 axis, and k_z is parallel to the C_3 axis. The major axes of ellipsoids are tilted in the C_1C_3 planes θ (θ = 31.5° in Bi_2Te_3) about the crystallographic axes. Let us denote the central cross section of ellipsoids in the plane perpendicular to the C_3 axis by S_H. The de Haas–van Alphen oscillations for the coinciding cross sections S_H of all six ellipsoids are observed in a magnetic field **B** parallel to the C_3 axis. One can show that

$$S_H = 2\pi m_0E_F/\hbar^2(\alpha_{22}^*\alpha_{33}^*\sin^2\theta + \alpha_{11}^*\alpha_{22}^*\cos^2\theta)^{1/2}, \quad (3)$$

where

$$\alpha_{22}^* + \alpha_{33}^* = \alpha_{22} + \alpha_{33},$$
$$\alpha_{22}^*\alpha_{33}^* = \alpha_{22}\alpha_{33} - (\alpha_{23})^2. \quad (4)$$

The cross section S_H of the Fermi surface in the k space is related to the de Haas–van Alphen oscillation frequency F by the formula

$$S_H = 2\pi eF/\hbar. \quad (5)$$

One thus obtains the following formulas for the Fermi energy E_F and hole concentration p:

$$E_F = F(e\hbar/m_0)^*(\alpha_{11}^*\alpha_{22}^*\cos^2\theta + \alpha_{22}^*\alpha_{33}^*\sin^2\theta)^{1/2}, \quad (6)$$

$$p = (4\sqrt{2}/\pi^2\hbar^3)(m_0^3E_F^3/\alpha_{11}^*\alpha_{22}^*\alpha_{33}^*)^{1/2}. \quad (7)$$

Thus, the values of E_F and p can be derived from the experimental frequencies F found for the de Haas–van Alphen effect in the $Bi_{2-x}Fe_xTe_3$ samples, provided that the α_{ij} parameters are known. Recent direct measurements of the cyclotron resonance in Bi_2Te_3 single crystals in a magnetic field parallel to the C_3 axis suggest that the cyclotron masses are independent of temperature and charge-carrier concentration [13]. For this reason, we carried out calculations with the parameters $\alpha_{11}^* = 2.26$, $\alpha_{22}^* = 32.5$, and $\alpha_{33}^* = 11.6$ that had earlier been determined for Bi_2Te_3. These parameters correspond to the Fermi-surface anisotropy $\eta = S_{max}/S_{min} = S_b/S_a = 3.8$. According to our experimental data, the hole concentration decreases from $p = 7.5 \times 10^{18}$ cm^{-3} (Bi_2Te_3) to $p = 4.6 \times 10^{18}$ cm^{-3} ($Bi_{1.92}Fe_{0.08}Te_3$) and the Fermi energy also decreases, respectively, from $E_F = 37.8$ meV to $E_F = 28$ meV as the iron content in the samples increases.

7. Let now discuss the magnetic susceptibility $\chi(T)$. It can generally be written in the form

$$\chi(T) = \chi_L + \chi_{ni}(0) + \chi_c(T) + \chi_i(T), \quad (8)$$

where χ_L is the lattice contribution, which is diamagnetic and independent of temperature in bismuth telluride. It is due to the atomic-core and valence-band electrons which are localized and do not carry charge. The next term $\chi_{ni}(0)$ is the temperature-independent contribution from the possible neutral impurities in the crystal; $\chi_c(T)$ is the magnetic susceptibility of free charge carriers; and $\chi_i(T)$ is the susceptibility of magnetic impurity (Fe in our case); it depends on temperature and at high temperatures is paramagnetic. It follows from our measurements that the magnetic moment of Bi_2Te_3 oscillates in a magnetic field because of the quantization of the hole energy spectrum.

Charge-carrier-induced ferromagnetism in Group III–V element alloys with magnetic impurities was discovered in (In, Mn)As and, more recently, in (Ga, Mn)As (for review, see, e.g., [14]). Ferromagnetism in Group IV–VI DMS, namely, PbSnMnTe, is caused by the Ruderman–Kittel–Kasuya–Yosida (RKKY) interaction [7]. The RKKY interaction is long-range enough for the magnetic moments to mutually interact via the interaction with free charge carriers—holes in DMS with a small content of magnetic impurities. The mean-field theory of ferromagnetism in DMS is also suggested in [15].

The RKKY T_c value calculated for (Ga, Mn)As films is in satisfactory agreement with the experimental data on T_c [16]. In principle, it is hard to choose between the RKKY and mean-field theories because both provide the same values for transition temperature T_c. The sign of the oscillating RKKY interaction corresponds to the ferromagnetic interaction, because the first RKKY zero, after which the interaction changes sign and becomes antiferromagnetic, occurs at distances considerably longer than the cutoff length. This is so because of a rather low concentration of exchange-mediating holes. The RKKY theory not only accounts for the hole-induced ferromagnetism but also explains the absence of ferromagnetic transition in *n*-type DMS materials. The ferromagnetic transition in *n*-type DMS materials is hard to occur or even practically impossible because of the smaller effective electron masses and substantially smaller values of exchange integral.

It should also be pointed out that the theory of charge-carrier-induced ferromagnetism in the $III_{1-x}Mn_xV$ DMS materials was presented in recent work [17]. The theory takes into account spin splitting and dynamic correlations in the ordered state. The polarization of charge-carrier spins is responsible for the long-range exchange interaction between the Mn^{2+} ions in $III_{1-x}Mn_xV$.

In summary, a new class of diluted magnetic superconductors $Bi_{2-x}Fe_xTe_3$ was synthesized. The transition into the ferromagnetic state was observed. The transition temperature T_c increases with iron content and reaches 12 K at $x = 0.08$. The easy magnetic axis is parallel to the crystallographic axis C_3 (perpendicular to the layers). It is most likely that the ferromagnetic transition in the $Bi_{2-x}Fe_xTe_3$ DMS is due to the RKKY interaction. The hole concentration in the $Bi_{2-x}Fe_xTe_3$ samples decreases with increasing x; i.e., Fe is a donor. In addition, the introduction of Fe in Bi_2Te_3 substantially increases the Seebeck coefficient. No transition into the ferromagnetic state was observed for the *n*-type $Bi_{2-x}Fe_xSe_3$ samples.

REFERENCES

1. For a review on DMS, see J. K. Furdyna, J. Appl. Phys. **64**, R29 (1988).
2. N. B. Brandt, Zh. T. Ismailov, V. A. Kul'bachinskiĭ, *et al.*, Fiz. Nizk. Temp. **12**, 215 (1986) [Sov. J. Low Temp. Phys. **12**, 125 (1986)].
3. V. A. Kulbachinskii, P. D. Maryanchuk, I. A. Churilov, *et al.*, Semicond. Sci. Technol. **10**, 463 (1995).
4. H. Munekata, H. Ohno, S. von Molnar, *et al.*, Phys. Rev. Lett. **63**, 1849 (1989).
5. H. Ohno, H. Munekata, T. Penny, *et al.*, Phys. Rev. Lett. **68**, 2664 (1992).
6. H. Ohno, A. Shen, F. Matsukura, *et al.*, Appl. Phys. Lett. **69**, 363 (1996).

7. T. Story, R. R. Galazka, R. B. Frankel, and P. A. Wolff, Phys. Rev. Lett. **56**, 777 (1986).
8. G. A. Prinz, Science **282**, 1660 (1998).
9. K. Funagai, Y. Miyahara, H. Ozaki, and V. A. Kulbachinskii, in *Proceedings of International Conference on Thermoelectrics, Pasadena, 1996*, Ed. by T. Caillat, p. 408.
10. N. B. Brandt and V. A. Kulbachinskii, Semicond. Sci. Technol. **7**, 907 (1992).
11. *The Hall Effect and Its Applications*, Ed. by C. L. Chien and C. R. Westgate (Plenum, New York, 1980).
12. V. A. Kulbachinskii, N. Miura, H. Nakagawa, *et al.*, J. Phys.: Condens. Matter **11**, 5273 (1999).
13. V. A. Kulbachinskii, N. Miura, H. Arimoto, *et al.*, J. Phys. Soc. Jpn. **68**, 3328 (1999).
14. H. Ohno, J. Magn. Magn. Mater. **200**, 110 (1999).
15. T. Dietl, A. Haury, and Y. Merle d'Aubigne, Phys. Rev. B **55**, R3347 (1997).
16. F. Matsukara, H. Ohno, A. Shen, and Y. Sugawara, Phys. Rev. B **57**, R2037 (1998).
17. J. Konig, Hsiu-Hau Lin, and A. H. MacDonald, Phys. Rev. Lett. **84**, 5628 (2000).

Translated by V. Sakun

JETP Letters, Vol. 73, No. 7, 2001, pp. 357–360. Translated from Pis'ma v Zhurnal Éksperimental'noĭ i Teoreticheskoĭ Fiziki, Vol. 73, No. 7, 2001, pp. 401–404.

Specific Heat of $Na_{1-x}V_2O_5$ Single Crystals

A. N. Vasil'ev*, M. M. Markina*, M. Yu. Kagan, M. Isobe***, and Y. Ueda*****

** Moscow State University, Vorob'evy gory, Moscow, 119899 Russia*

e-mail: vasil@lt.phys.msu.su

*** Kapitsa Institute for Physical Problems, Russian Academy of Sciences, Moscow, 117334 Russia*

**** Institute for Solid State Physics, Tokyo University, Kashiwa, Chiba 277-8581, Japan*

Received February 27, 2001

Temperature dependences of the specific heat C and the magnetic susceptibility χ of $Na_{1-x}V_2O_5$ single crystals (x = 0, 0.01, 0.02, 0.03, and 0.04) are studied. In NaV_2O_5, the transition to the spin-gap state (T_c = 34 K) is accompanied by a sharp decrease in χ, while C exhibits a λ-shaped anomaly. At low temperatures, the specific heat of NaV_2O_5 is approximated by the sum of phonon $\sim T^3$ and magnon $\sim\exp(-\Delta/T)$ contributions, which makes it possible to estimate the Debye temperature Θ_D = 336 K and the gap in the magnetic excitation spectrum Δ = 112 K. With the departure from stoichiometry, the anomalies observed in the behavior of χ and C are spread and shifted to lower temperatures. The low-temperature specific heat of nonstoichiometric samples is determined by the sum of phonon and magnon components and the contribution due to the presence of defects. The values of magnetic entropy characterizing the phase transitions in $Na_{1-x}V_2O_5$ are calculated. © *2001 MAIK "Nauka/Interperiodica".*

PACS numbers: 75.40.Cx

The characteristic features of the ground-state formation in NaV_2O_5 have been actively investigated since the discovery of the phase transition in this compound at $T_c \sim 34$ K [1]. According to the existing concepts, the charge transfer at this temperature occurs between V sites in NaV_2O_5, resulting in structural distortions and the appearance of an energy gap in the magnetic excitation spectrum [2, 3]. The crystal structure of NaV_2O_5 is formed by corrugated layers of VO_5 complexes separated from each other by Na atoms. At high temperatures, all V sites are equivalent and the formal valence of V is +4.5 [4]. This means that a single 3*d* electron that is not involved in the ionic-covalent bonds is divided between two nearest V ions and occupies the bonding V–O–V molecular orbital [5]. These orbitals form rungs of spin ladders shifted relative to each other by a half-period along the *b* axis in the *ab* plane.

At low temperatures, the NaV_2O_5 structure has two inequivalent V sites with formal valences $4.5 - \delta$ and $4.5 + \delta$, where δ determines the deviation of the valence from its mean value (below, we will use the notations V^{4+} and V^{5+} for these ions). The magnetic V^{4+} and nonmagnetic V^{5+} ions are positioned in the spin ladders in a zigzag manner. According to [6], the alternation of the exchange interaction in these ladders gives rise to an energy gap in the magnetic excitation spectrum of NaV_2O_5.

The specific heat of NaV_2O_5 single crystals, including those with Na deficiency, was considered in a number of papers [7–12]. Although the data reported in these publications testify to the sensitivity of the specific heat to the chemical composition, the effect of deviation from stoichiometry on the specific heat of $Na_{1-x}V_2O_5$ has never been thoroughly investigated over a wide temperature range.

This paper describes the study of $Na_{1-x}V_2O_5$ single crystals (x = 0, 0.01, 0.02, 0.03, and 0.04) grown from the melt by using $NaVO_3$ as a flux. The samples had the shape of parallelepipeds with characteristic dimensions of several millimeters and characteristic mass of several tens of milligrams. The magnetic susceptibility was measured by a Quantum Design SQUID magnetometer in a magnetic field of 0.1 T in the temperature range 5–80 K. The specific heat of single crystals was measured by an adiabatic microcalorimeter in the temperature range 5–160 K.

The temperature dependences of the magnetic susceptibility of $Na_{1-x}V_2O_5$ are presented in Fig. 1. These dependences show that, with the deviation from stoichiometry, the anomaly accompanying the phase transition becomes less pronounced and shifts to lower temperatures. Simultaneously, the contribution made by Na vacancies to χ noticeably increases. The appearance of the vacancies gives rise to the transition of part

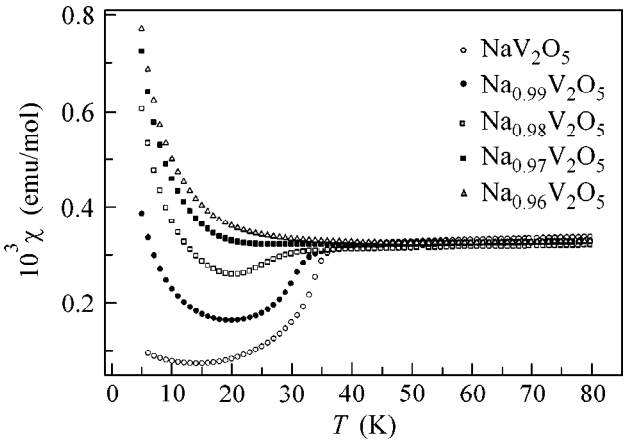

Fig. 1. Temperature dependences of the magnetic susceptibility of $Na_{1-x}V_2O_5$ single crystals.

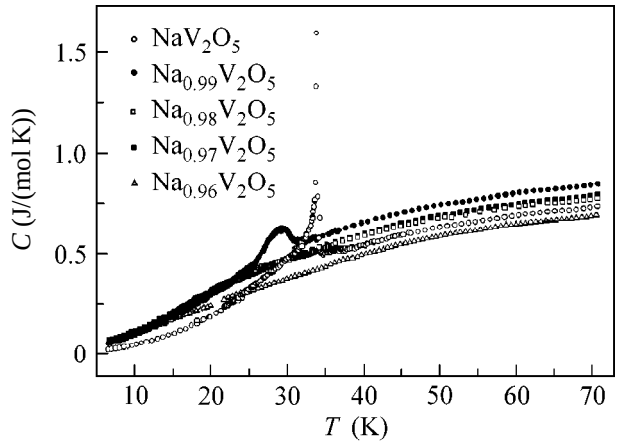

Fig. 2. Temperature dependences of the specific heat of $Na_{1-x}V_2O_5$ single crystals.

of the V^{4+} ions to the V^{5+} ionization state, and the remaining noncompensated moments of V^{4+} make an additional contribution to the susceptibility. In $Na_{1-x}V_2O_5$ samples with $x = 0.03$ and 0.04, no decrease in the magnetic susceptibility was observed at low temperatures. This result is in good agreement with the estimated value of critical defect concentration $x_c = 0.035$ above which the gap in the magnetic excitation spectrum of $Na_{1-x}V_2O_5$ does not appear. The estimate for critical defect concentration follows from the Nagaoka theorem [13], which gives $x_c \sim \Delta/2t_{\|}$. Here, $\Delta \sim 100$ K is the gap in the magnetic excitation spectrum of NaV_2O_5, and $t_{\|} \sim 1400$ K is the kinetic energy of an electron moving along the spin ladder [14]. It should be noted that the estimate obtained using the Nagaoka theorem in this case not only is correct within an order of magnitude but also agrees quantitatively with the experimental results.

The temperature dependences of the specific heat of $Na_{1-x}V_2O_5$ are presented in Fig. 2. The anomaly accompanying the phase transition is most pronounced in the sample with the stoichiometric composition. Outside the phase transition region, the specific heat of this crystal takes the lowest values, as compared to the other samples. At temperatures $T < T_c$, the specific heat increases with x (except for the sample with $x = 0.04$). The temperatures at which the anomalies of specific heat and kinks in the temperature dependences of magnetic susceptibility are observed allow one to determine the dependence of the phase transition temperature on the composition for $Na_{1-x}V_2O_5$ compounds. These data correlate well with each other and show that, with the departure from stoichiometry, the transition temperature varies according to the law $dT_c/dx = -4$ K per 1% Na deficiency.

The analysis of the temperature dependences of specific heat was performed on the assumption that the specific heat is described by the sum of phonon and magnon components plus the contribution due to the presence of Na vacancies in the samples with a nonstoichiometric composition.

In the temperature range 5–20 K, the energy gap Δ that occurs in the magnetic excitation spectrum of a stoichiometric sample can be considered to be temperature independent. Then, the temperature dependence of the specific heat can be approximated by the sum of the phonon $C_{ph} = \beta T^3$ and magnon $C_{mag} = A_0\exp(-\Delta/T)$ components. The coefficient of the phonon component $\beta = 12\pi^4 R\nu/5\Theta_D^3$, where R is the universal gas constant and $\nu = 8$ is the number of atoms in the formula unit, allows one to estimate the Debye temperature: $\Theta_D \sim 336$ K. According to the data obtained from other measurements, this value falls within 280–435 K [13–15]. The value of energy gap estimated on the basis of the experimental data, $\Delta = (112 \pm 18)$ K, agrees well with the value obtained for the gap in the magnetic excitation spectrum from neutron diffraction studies ($\Delta = 114$ K) [3]. The approximation of the experimental data for the nonstoichiometric $Na_{1-x}V_2O_5$ samples by the sum of phonon and magnon contributions yields largely underestimated values for the energy gap.

To take into account the additional contribution that is made by Na vacancies to the specific heat, it is necessary to introduce an additional term: $C_x = B_x(T/\Delta_0)^n$. The phonon contribution to the specific heat of nonstoichiometric samples, $C_{ph} = \beta T^3$ with $\beta = 0.425$ mJ/(mol K^4), is assumed to be equal to that in the stoichiometric sample. On the coefficients of the magnon (A_x) and vacancy (B_x) components, the following conditions were imposed: $A_x = A_0(1 - x/x_C)$ and $B_x = B_4 x/x_C$. The coefficients A_x and B_x, the energy gap $\Delta(x)$, and the exponent $n(x)$ that correspond to the closest agreement

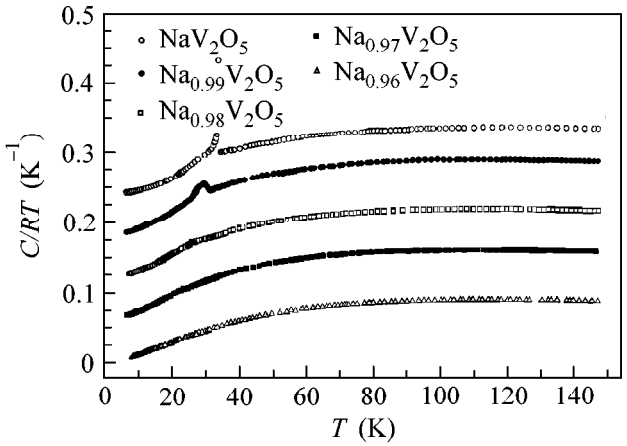

Fig. 3. Temperature dependences of the reduced specific heat C/RT of $Na_{1-x}V_2O_5$ single crystals. For convenience, the curves are spaced at 0.0625 K^{-1} intervals.

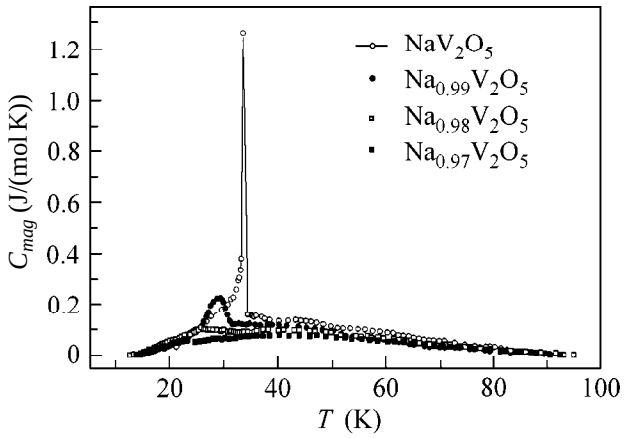

Fig. 4. Magnetic component of the specific heat of $Na_{1-x}V_2O_5$ single crystals.

between the theory and the experimental data on the specific heat of $Na_{1-x}V_2O_5$ are presented in the table. One can see that, as x increases, the energy gap in $Na_{1-x}V_2O_5$ decreases and the exponent in the vacancy term converges to two. The appearance of the term quadratic in temperature in the specific heat of nonstoichiometric samples at low temperatures could be attributed to the magnons in a two-dimensional antiferromagnet. However, it should be noted that the formation of a long-range magnetic ordering with increasing concentration of Na vacancies was never observed in $Na_{1-x}V_2O_5$.

Figure 3 shows the temperature dependences of C/T in the temperature range 5–150 K. The determination of the entropy of phase transition in $Na_{1-x}V_2O_5$ presents considerable problems, because the fluctuation region in this low-dimensional compound extends to high temperatures [15]. To set off the magnon contribution to the specific heat, the phonon contribution outside the fluctuation region in the dependence of C/T on T was approximated by a polynomial. Subtracting the phonon contribution from the experimental dependences, one can obtain the magnetic component of the specific heat, as shown in Fig. 4. The areas under these curves determine the magnetic entropy released upon the phase transition. The values of ΔS_{mag} determined in this way for $Na_{1-x}V_2O_5$ are shown in the table. These values should be compared with the theoretical estimate $\Delta S_{mag} = R\ln(2S + 1) = 5.76$ J/(mol K), which is valid for an ordered magnetic system with spin $S = 1/2$. For the stoichiometric sample, a good agreement with the theoretical estimate can be achieved upon the introduction of an upper bound $T \sim 65$ K to the region of calculations, which approximately corresponds to the transition from the regime of quasi-one-dimensional magnetic fluctuations to the regime of quasi-three-dimensional ones [15]. In the samples with the composition close to the stoichiometric one, the magnetic component of the specific heat has a peak at the phase transition point and a diffuse fluctuation region. As the deviation from stoichiometry increases, the magnetic entropy released at the phase transition decreases and the peak becomes indistinguishable.

Thus, a systematic study of the magnetic susceptibility and the specific heat of $Na_{1-x}V_2O_5$ ($x = 0$, 0.01, 0.02, 0.03, and 0.04) showed that the phase transition is rapidly suppressed with the departure from stoichiometry. A decrease in the phase transition temperature is accompanied by a decrease in the energy gap in the magnetic excitation spectrum; in the samples with $x >$ 0.03, the gap is not observed. The appearance of the component $\sim T^2$ in the specific heat of nonstoichiometric samples at low temperatures can presumably be due to the hopping degree of freedom of the unpaired electrons on the bonding V–O–V molecular orbitals.

Mean values of the parameters A_x and B_x that were used in calculating the magnon and vacancy contributions to the specific heat, the exponent in the vacancy term n_x, the energy gap in the spectrum of magnetic excitations Δ_x, and the magnetic entropy ΔS_{mag} of $Na_{1-x}V_2O_5$ single crystals

Composition x, %	A_x	B_x	Δ_x, K	n_x	ΔS_{mag}, J/(mol K)
0	14	0	112.5	–	7.7
1	10	2.3	97.8	1.53	5.7
2	6	4.6	75.5	1.75	4.6
3	2	6.7	52.0	1.85	1.2
4	0	8	–	2.00	0.1

We are grateful to K.I. Kugel', M.S. Mar'enko, A.I. Smirnov, and S.S. Sosin for useful discussions. The work was supported by the Russian Foundation for Basic Research (project nos. 02-99-17828 and 00-02-16255), a grant from the President of the Russian Federation (no. 96-15-9694), the INTAS (grant nos. 99-0155 and 97-0963), and the NWO (grant no. 047-008-012).

REFERENCES

1. M. Isobe and Y. Ueda, J. Phys. Soc. Jpn. **65**, 1178 (1996).
2. T. Ohama, H. Yasuoka, and Y. Ueda, Phys. Rev. B **59**, 3299 (1999).
3. Y. Fujii, H. Nakao, M. Nishi, *et al.*, J. Phys. Soc. Jpn. **66**, 326 (1997).
4. H.-G. von Schnering, Y. U. Grin, M. Kaupp, *et al.*, Z. Kristallogr. **213**, 246 (1998).
5. M. Cuoco, P. Horsch, and F. Mack, Phys. Rev. B **60**, R8438 (1999).
6. M. V. Mostovoy and D. I. Khomskii, Solid State Commun. **113**, 159 (1999).
7. M. Koeppen, D. Pankert, R. Hauptmann, *et al.*, Phys. Rev. B **57**, 8466 (1998).
8. H. Schwenk, S. Zherlitsyn, and C. Geibel, Phys. Rev. B **60**, 9194 (1999).
9. J. Hemberger, M. Lohmann, M. Nicklas, *et al.*, Europhys. Lett. **42**, 661 (1998).
10. D. K. Powell, J. W. Brill, Z. Zeng, *et al.*, Phys. Rev. B **58**, R2937 (1998).
11. W. Schnelle, Yu. Grin, and R. K. Kremer, Phys. Rev. B **59**, 73 (1999).
12. A. I. Smirnov, S. S. Sosin, R. Calemczuk, *et al.*, cond-mat/0003169.
13. Y. Nagaoka, Phys. Rev. **147**, 392 (1966).
14. H. Smolinski, C. Gros, W. Weber, *et al.*, Phys. Rev. Lett. **80**, 5164 (1998).
15. S. Ravy, J. Jegoudez, and A. Revcolevschi, Phys. Rev. B **59**, R681 (1999).

Translated by E. Golyamina

JETP Letters, Vol. 73, No. 7, 2001, pp. 361–365. Translated from Pis'ma v Zhurnal Éksperimental'noĭ i Teoreticheskoĭ Fiziki, Vol. 73, No. 7, 2001, pp. 405–409.

Observation of the Second Harmonic in the Phase Dependence of a Superconducting Current in Nb/Au/YBCO Heterojunctions

P. V. Komissinskiĭ[1,2], G. A. Ovsyannikov[1], E. Il'ichev[3], and Z. Ivanov[2]

[1] *Institute of Radio Engineering and Electronics, Russian Academy of Sciences, Moscow, 103907 Russia*
e-mail: gena@hitech.cplire.ru

[2] *Chalmers University of Technology, S 411 96 Göteborg, Sweden*

[3] *Institute for Physical High Technology, Department of Cryoelectronics, P.O. Box 100239, D-07702 Jena, Germany*

Received February 21, 2001; in final form, March 12, 2001

The second harmonic in the dependence of a superconducting current on the phase difference of superconducting wave functions of the electrodes was observed experimentally in Nb/Au/(001)$YBa_2Cu_3O_x$ heterojunctions. Possible reasons for its appearance were discussed within the framework of a mixed ($d \pm s$) symmetry order parameter of $YBa_2Cu_3O_x$. © *2001 MAIK "Nauka/Interperiodica".*

PACS numbers: 74.80.Dm; 73.40.-c

It is presently known that the majority of metal oxide high-T_c superconductors (MOHTS) are characterized by the *d* symmetry of the superconducting order parameter [1]. This was most clearly manifested in experiments on studying superconducting quantum interference devices (SQUIDs) containing junctions of a conventional (with the *s*-type symmetry of the order parameter) superconductor (S) connected to two orthogonal directions of the MOHTS basal plane [2]. The problem of electron transport in MOHTS/S junctions (here, the slash designates a potential barrier) in the direction perpendicular to the MOHTS basal plane still remains unclear [3–6]. Because of the *d* symmetry of the order parameter in MOHTSs, the superconducting current in these heterojunctions must be small (proportional to the second degree of the averaged interface transmittance $\overline{D}^2$) and must vary with the phase difference two times more frequently. That is, the superconducting current must contain a component corresponding to the second harmonic of the current–phase relation (CPR) [7]. However, the critical current observed in the experiments [3–6] multiplied by the normal resistance depends only slightly on the interface transmittance; however, it decreases if an epitaxial MOHTS film is used instead of a single crystal [5]. The experimental data can be explained based on the assumption that the MOHTS is characterized by the mixed *s*–*d* symmetry of the superconducting order parameter, with the *s*-wave component changing its sign (that is, changing its phase by π) and the *d*-wave component remaining unchanged at the twin boundary [6]. Studying the appearance of microwave-induced Shapiro steps in CPRs of Pb/$YBa_2Cu_3O_x$ junctions demonstrated that the second harmonic is absent in the CPR with an accuracy of up to 5% [5].

In this work, we report an experimental study of CPRs for heterojunctions constructed of niobium (*s*-wave superconductor) and a *c*-oriented $YBa_2Cu_3O_x$ (YBCO) film with an additional gold interlayer (Nb/Au/YBCO). The CPRs were measured using a radiofrequency superconducting quantum interference device (SQUID). The second harmonic of the CPR was found in the experiment. Estimates were given indicating that electron transport in heterojunctions on (001) YBCO is determined by the contact between the *s*-wave and (*d*–*s*)-wave superconductors.

Epitaxial (001) YBCO films 150 nm thick were grown by laser deposition on (001) $LaAlO_3$ and (001) $SrTiO_3$ substrates. The superconducting transition temperature of films was measured by the magnetic induction method and was found to be T_c = 88–90 K. Immediately after deposition, the YBCO film was coated with a thin Au layer without breaking a vacuum, which prevented the YBCO surface from degradation. This allowed interfaces to be obtained with a low characteristic resistance $r \equiv R_N A = 10^{-5}$–$10^{-6}\ \Omega\ \text{cm}^2$ (R_N and A are the normal resistance and the contact area, respectively). The Nb film was deposited by dc magnetron sputtering. Note that the direct Nb/YBCO contact gave the boundary with a considerably higher characteristic resistance $r \sim 10^{-2}\ \Omega\ \text{cm}^2$. Photolithography and ion-beam etching with low-energy argon ions were used to form the geometry of Nb/Au/YBCO heterojunctions (the thickness of gold is 8–20 nm, and niobium, 200 nm). The current in these heterojunctions flows perpendicular to the substrate (along the *c* axis of

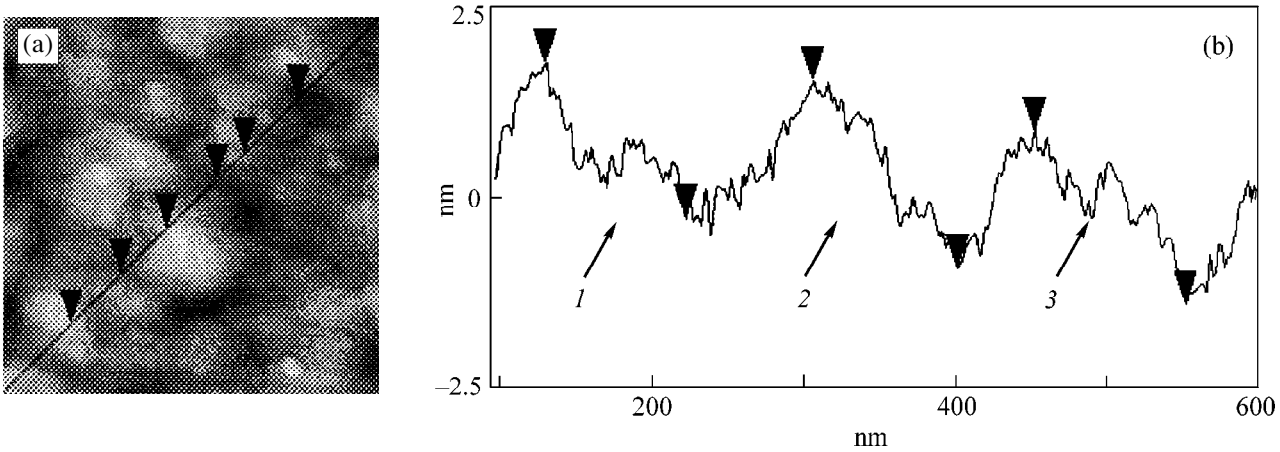

Fig. 1. (a) Two-dimensional profile of a (001) YBCO film obtained using an atomic force microscope; (b) film cross section. Numbers indicate film areas in which distances between the marks were measured. The largest horizontal and vertical distances between the marks are 100 and ~3 nm, respectively; that is, $\gamma \approx 2°$.

YBCO), and there is no contact with the basal plane of the YBCO film [8, 9].

To reduce the effect of transport along the basal plane due to the roughness of the surface, the growth process was optimized with the aim to obtain YBCO films with a smooth surface. The morphology of films was monitored in test samples using a high-resolution atomic force microscope. The greatest surface roughness of the (001) YBCO films used in heterojunctions (calculated as the difference between the points of the maximum and minimum deviations from the substrate plane) was 3 nm, with the horizontal distance between these points equal to 100 nm (Fig. 1). Hence, the typical average angle of inclination of YBCO-film surface areas to the (001) YBCO plane can be estimated at $\gamma \approx 2°$. The contribution to the measured resistance of electron transport due to contact with the basal plane of the YBCO film was estimated by calculating the characteristic resistance r of the boundaries between Au and YBCO [8, 9]. The resistance r of heterojunctions was determined from the condition that the resistances of the boundaries between Au and YBCO along the c axis (r_c) and in the basal plane of YBCO (r_{ab}) are connected in parallel. These resistances are due to the mismatch between the Fermi velocities of the contacting materials with a sharp interface:

$$r = r_c r_{ab}/(r_{ab} + r_c \tan\gamma), \qquad (1)$$

where $\tan\gamma \approx A_{ab}/A$, and A_{ab} is the total area of contacts with the basal plane of the YBCO film. The inclined film surfaces were replaced by a set of (001) YBCO planes and planes perpendicular to them with characteristic resistances r_c and r_{ab}, respectively. It was shown in [9] for the typical Fermi-momentum anisotropy of order 3 that r_c exceeds r_{ab} by no more than an order of magnitude. Hence, the current through the contact with the basal plane is small for the surface roughness observed experimentally ($\gamma \approx 2°$). This is confirmed by the absence of the conductance peak in Nb/Au/YBCO junctions at temperatures above the critical temperature of niobium and small biases [the anomaly caused by the Andreev reflection in a *d*-wave superconductor (D)]. Theory predicts the appearance of the given anomaly for a rough boundary of N/D heterojunctions (N is a normal metal) even in the case of an arbitrarily oriented *d*-wave superconductor [10]. Note that the current through superconducting short circuits formed by pinholes in the Au film between Nb and YBCO is small, because r measured for the Nb/YBCO boundary exceeds the resistance of the Au/YBCO boundary by 3–4 orders of magnitude [8].

Electrophysical properties were measured for more than 20 single junctions of sizes from 10×10 to 100×100 μm and five radiofrequency SQUIDs. The table presents typical parameters of single junctions for which the critical current grows with an increase in area. For the junctions studied, the critical current density was in the range j_c = 1–12 A/cm^2, whereas $I_c R_N$ = 10–90 μV, where R_N is the normal junction resistance determined from the differential junction resistance R_d at bias $V \approx 2$ mV. The current–voltage characteristic (I–V curve) and the voltage dependence of the differential junction resistance R_d are shown in Fig. 2. At small biases, the junction I–V curve closely corresponds to the resistive model of a small-capacitance Josephson junction. With increasing bias $V > 2$ mV, the I–V curve takes the form $V = (I + I_e)R_N$, where $I_e < 0$. The excess current $I_e > 0$ is observed in all superconducting junctions with direct (nontunnel-type) conductivity [11]. Negative I_e (low current) is a characteristic feature of superconducting two-barrier S/N/S' heterostructures, in which I_e changes its sign (transition from excess to low current takes place) as the neighborhood effect in the N interlayer decreases [12–14]. It is seen in Fig. 2 that the

junction *I–V* curves at high biases are described well by the equation [12]

$$V = IR_N + I_eR_N\tanh(eV/kT), \qquad (2)$$

which is typical for S/N/S' structures. For the junction shown in Fig. 2, $I_e = -145$ μA at $T = 4.2$ K. According to the calculation [14], the experimental parameters of the structures studied must give $I_e = (-\overline{D}_1\Delta_{YBCO} - \Delta_{Nb})/(eR_N) \approx -270$ μA, where $r = 10^{-5}$–10^{-6} Ω cm^2 determines the direction-averaged transmittance of the Au/YBCO interface $\overline{D}_1 = 2\rho_c l/3r = 10^{-4}$–$10^{-5}$, Δ_{YBCO} is the YBCO order parameter, $\Delta_{Nb} = 1.2$ mV is the Nb gap, and $\rho_c \approx 10^{-2}$ Ω cm and $l \approx 1$ nm are, respectively, the resistivity of and the mean free path in the YBCO film in the *c* direction [9].

A singularity is observed in the $R_d(V)$ curve as a decrease in R_d at $V = 1.2$ mV, which corresponds to Δ_{Nb} in magnitude. Its temperature dependence is close to that predicted by the BCS theory. The singularity in the *I–V* curve disappears together with the critical current at $T = 8.5$–9.1 K. The temperature dependence $I_c(T)$ is close to $\Delta_{Nb}(T)$. Note that gap singularities in an *s*-wave superconductor (Pb) were observed previously in Pb/YBCO [5, 6].

In order to measure the CPR, a SQUID was formed from a junction 10×10 μm in size short-circuited by a YBCO film with an inductance $L \approx 80$ pH and by a junction of a considerably larger area of 100×100 μm. The SQUID impedance was measured as a function of the external magnetic flux Φ_e with the use of an oscillatory circuit inductively coupled to a ring. The phase difference φ across the junction under study is determined by the magnetic flux in the ring Φ_i as follows: $\varphi = 2\pi\Phi_i/\Phi_0$, where $\Phi_0 = h/2e = 2.07 \times 10^{-15}$ T m^2 is the magnetic flux quantum. The CPR $f(\varphi) = I_s(\varphi)/I_c$ is determined from measurements of the phase difference α between the driving high-frequency current and the voltage across the circuit

$$\tan\alpha = k^2Qi_cf'(\varphi)/(1 + i_cf'(\varphi)), \qquad (3)$$

where $f'(\varphi) = df(\varphi)/d\varphi_e$, $\varphi_e = 2\pi\Phi_e/\Phi_0$ is the normalized external magnetic flux, $i_c = 2\pi LI_c/\Phi_0$ is the normalized critical current of the junction, and *Q* is the quality factor of the oscillatory circuit. The CPR is calculated from experimental data by Eq. (3) at $i_c < 1$. In this case, we neglect the effect of junction capacitance [15].

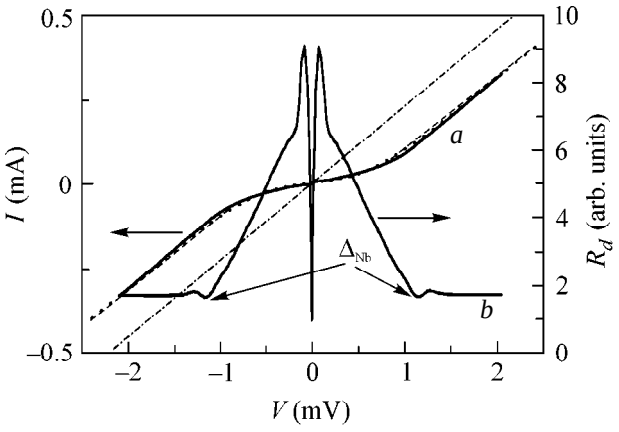

Fig. 2. *a I–V* curve and *b* voltage dependence of the differential resistance of a heterostructure at $T = 4.2$ K. The dependence obtained from Eq. (2) is shown in the *I–V* curve by the dashed line; Ohm's law $V = IR_N$ is shown by the dot-and-dash line.

Experimental $I_s(\varphi)$ curves are shown in Fig. 3 for several temperatures. As the temperature decreases, the

Parameters of the Nb/Au/YBCO heterojunctions measured at $T = 4.2$ K

Junction no.	A, μm^2	d, nm	I_c, μA	J_c, A/cm^2	R_N, Ω	R_NA, μΩ cm^2	I_cR_N, μV	Δ_{Nb}, mV
*SQ*1*J*1	100	20	5	5	4.4	4.4	22	1.2
*SQ*1*J*3	10000	20	181	1.81	0.15	15	27	–
*SQ*1*J*5	100	20	1.5	1.5	18.3	18.3	27.5	0.8
*SQ*3*J*1	100	20	1	1	68	68	68	1.1
*SQ*7*J*10	225	8	15	6.7	5.1	11.5	76.5	1.1
*SQ*7*J*11	10000	8	234	2.3	0.05	5	11.7	–
*SQ*7*J*3	625	8	20	3.2	1.3	8.1	26	1.1
*SQ*7*J*4	900	8	23	2.6	0.83	7.5	19.1	1.2
*SQ*7*J*13	400	8	10	2.5	1	4	10	–
*SQ*7*J*15	400	8	16	4	1.8	7.2	28.8	–
*SQ*7*J*17	100	8	2	2	18.8	18.8	37.6	1.2
*SQ*7*J*18	100	8	3	3	10	10	30	–
*SQ*10*J*3	100	18	1.2	1.2	60	60	72	1.2

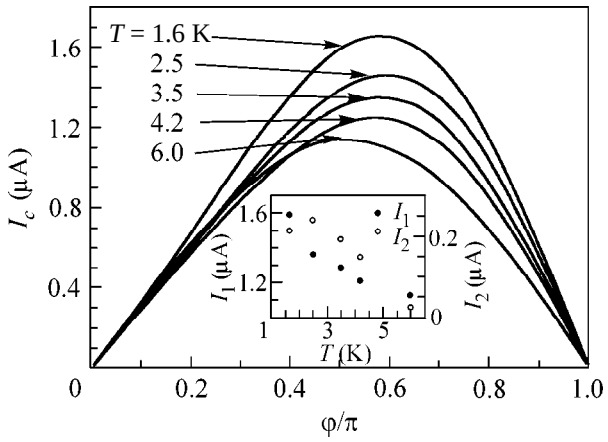

Fig. 3. Transformation of the CPR of a heterostructure as a function of temperature. The inset shows the temperature dependence of the first and the second harmonics of the Fourier transform of CPR.

CPR exhibits a transformation that corresponds to the appearance of the second harmonic of its Fourier expansion in terms of φ. Taking into account only two harmonics, one obtains $I_s(\varphi) = I_1 \sin\varphi + I_2 \sin(2\varphi + \phi)$. If, following [5], the occurrence of two harmonics of the CPR is explained by the combined *d*- and *s*-wave symmetry of the YBCO order parameter, then an agreement with the experiment is observed for *d*–*s* ($\phi = \pi$). Using the theoretical approach [7], according to which the YBCO order parameter can be represented as $\Delta_{\mathrm{YBCO}}(\theta, \psi) = \Delta_{d-\mathrm{YBCO}} \sin^2\theta \cos(2\psi) - \Delta_{s-\mathrm{YBCO}}$ (θ and ψ are the azimuthal and radial angles, respectively), and assuming that $\Delta_{\mathrm{Nb}}(\theta, \psi) = 1.2$ mV for niobium, we find that the theory [7] gives the best agreement with the experiment at $T = 1.7$ K for the following parameters: $\Delta_{d-\mathrm{YBCO}} = 20$ mV, $\Delta_{s-\mathrm{YBCO}} = 0.45$ mV, and the averaged barrier transmittance $\bar{D} \approx 3 \times 10^{-2}$.[1]

At the same time, the amplitudes of higher harmonics of the expansion of $I_s(\varphi)$ in terms of $\sin(n\varphi)$ for a tunnel junction with interface transmittance $\bar{D}_1$ are proportional to the higher degrees of interface transmittance and to the gap ratio; that is, $I_2/I_1 \approx \bar{D}_1 \Delta_{\mathrm{Nb}}/\Delta_{s-\mathrm{YBCO}} \sim \bar{D}_1$. Hence, within the framework of this simple estimate, $I_2/I_1 \sim 10^{-4}$–10^{-5}. However, the experiment at $T = 1.7$ K gives $I_2/I_1 \sim 0.16$. It may well be that the following two factors are determining, although not taken into account in these simple estimates.

The first factor is the twinning of the (001) YBCO film, which leads to the sign reversal of the *s*-wave component at the twin boundary and, hence, decreases the amplitude I_1 because of the mutual compensation of contributions from the domains with different signs of *s*-wave component. In the case of equal areas of the twin domains, I_1 must equal zero, and I_1 must increase proportional to $\sqrt{N}$ in the case of a random scatter of twin-boundary sizes, where *N* is the number of twin boundaries in the heterojunction [6, 16]. The dependence of the critical current on the junction area in our experiment is not proportional to $\sqrt{N}$ (see table), though this proportionality is typical for the random distribution of twin domain sizes. In fact, a critical current from an uncompensated part δ of domains is observed. The total superconducting current from the *s*-wave component in a heterojunction of the same area on an untwinned (001) YBCO film must be higher by a factor of δ^{-1}. In this case, the model of a Josephson junction with an alternating current density [17] applies qualitatively to the heterojunction under study. This model predicts that the amplitude of the second harmonic in the current–phase relation is significant [18]. However, further investigations are required for a quantitative comparison to be made between the theory and experiment.

Note that the contribution of the *d*-wave component is independent of the number and the size distribution of twin boundaries and that we do not observe the (*d* + *is*)-wave component (*i* is the imaginary unit). This component may arise either because of the influence of twin-boundary vicinity, where the sign changes from *d* + *s* to *d* – *s* [16], or due to the sign reversal of the *s*-wave component near the YBCO film surface [19].

The second possible reason for the existence of anomalously high I_2 is the fact that a Nb/Au interface with transmittance $\bar{D}_2 \approx 10^{-1}$ occurs in Nb/Au/YBCO. It is evident in Fig. 2 that this interface affects the *I*–*V* curve. Actually, the second harmonic of the CPR may appear in the case of a strongly asymmetric two-barrier structure [20]. On the other hand, simple estimates following from Eq. (9) of [20] indicate that $I_2/I_1 \propto \bar{D}_1$ for the Nb/Au/YBCO heterostructures studied in this work, and, hence, the second harmonic amplitude of the CPR is small. However, the ultimate answer to the question of the Nb/Au interface effect on the CPR in Nb/Au/YBCO heterostructures can be determined only after accurate numerical calculations.

Note in conclusion that, although general regularities were found in the behavior of the heterojunctions studied (*I*–*V* curve shape, temperature dependence of the critical current, gap singularity due to niobium, etc.), a rather large scatter (up to 100%) was observed for quantitative parameters such as interface resistance, critical current density, and ratio of the first and the second harmonics of the CPR. Here, along with the Au/YBCO interface, the Nb/Au interface and the twinning of YBCO films are key factors that are difficult to control by electrophysical methods.

We are grateful to D.V. Balashov, P.N. Dmitriev, S.A. Kovtonyuk, and K.I. Konstantinyan for assistance

[1] $\Delta_{\mathrm{YBCO}}(\theta, \psi)$ is normalized as $(1/2\pi)\int_0^{2\pi}\int_0^{\pi/2} \Delta_{\mathrm{YBCO}}(\theta, \psi)\sin\theta d\theta d\psi = \Delta_{d-\mathrm{YBCO}}$ [7].

in measurements and to A.V. Zaĭtsev, T. Klaeson, M.Yu. Kupriyanov, T. Lofwander, P.B. Mozhaev, I. Tanaka, A. Tsalenchuk, and V. Shumeĭko for useful discussions.

This work was supported in part by the Russian Foundation for Basic Research, the federal program "Topical Problems of Condensed Matter Physics," the subprogram "Superconductivity," the European INTAS program, the Sweden consortium for studying new materials, and the "Science for Peace" program (project no. 973559).

REFERENCES

1. C. C. Tsuei and J. R. Kirtley, Rev. Mod. Phys. **72**, 969 (2000).
2. D. A. Wollman, D. J. van Harlingen, W. C. Lee, *et al.*, Phys. Rev. Lett. **71**, 2134 (1993).
3. H. Akoh, C. Camerlingo, and S. Takada, Appl. Phys. Lett. **56**, 1487 (1990).
4. A. G. Sun, D. A. Gajewski, M. B. Maple, *et al.*, Phys. Rev. Lett. **72**, 2267 (1994).
5. R. Kleiner, A. S. Katz, A. G. Sun, *et al.*, Phys. Rev. Lett. **76**, 2161 (1996).
6. K. A. Kouznetsov, A. G. Sun, B. Chen, *et al.*, Phys. Rev. Lett. **79**, 3050 (1997).
7. Y. Tanaka, Phys. Rev. Lett. **72**, 3871 (1994).
8. P. V. Komissinskiĭ, G. A. Ovsyannikov, N. A. Tulina, *et al.*, Zh. Éksp. Teor. Fiz. **116**, 2140 (1999) [JETP **89**, 1160 (1999)].
9. P. V. Komissinskiĭ, G. A. Ovsyannikov, and Z. G. Ivanov, Fiz. Tverd. Tela (St. Petersburg) **43**, 769 (2001) [Phys. Solid State **43**, 801 (2001)].
10. M. Fogelström, D. Rainer, and J. A. Sauls, Phys. Rev. Lett. **79**, 281 (1997).
11. K. K. Likharev, Rev. Mod. Phys. **51**, 101 (1979).
12. A. V. Zaĭtsev, Pis'ma Zh. Éksp. Teor. Fiz. **51**, 35 (1990) [JETP Lett. **51**, 41 (1990)].
13. G. E. Babayn, L. V. Filippenko, G. A. Ovsyannikov, *et al.*, Supercond. Sci. Technol. **4**, 476 (1991).
14. A. F. Volkov, A. V. Zaitsev, and T. M. Klapwijk, Physica C (Amsterdam) **210**, 21 (1993).
15. E. Il'ichev, V. Zakosarenko, V. Schultze, *et al.*, Appl. Phys. Lett. **72**, 731 (1998); E. Il'ichev, V. Zakosarenko, R. P. J. Ijsselsteijn, *et al.*, Phys. Rev. Lett. **81**, 894 (1998).
16. M. Sigrist, K. Kuboki, P. A. Lee, *et al.*, Phys. Rev. B **53**, 2835 (1996).
17. R. G. Mints, Phys. Rev. B **57**, R3221 (1998).
18. E. Il'ichev, V. Zakosarenko, R. P. J. Ijsselsteijn, *et al.*, Phys. Rev. B **59**, 11 502 (1999).
19. R. Haslinger and R. Joynt, J. Phys.: Condens. Matter **12**, 8179 (2000).
20. M. Yu. Kupriyanov, A. Brinkman, A. A. Golubov, *et al.*, Physica C (Amsterdam) **326–327**, 16 (1999).

Translated by A. Bagatur'yants

JETP Letters, Vol. 73, No. 7, 2001, pp. 366–369. Translated from Pis'ma v Zhurnal Éksperimental'noĭ i Teoreticheskoĭ Fiziki, Vol. 73, No. 7, 2001, pp. 410–413.

Fractal Model of Magnetization Reversal in a Strained Garnet Ferrite Film

L. A. Dovbnya, D. E. Naumov, and B. V. Khramov

Samara State Pedagogical University, Samara, 443043 Russia

Received March 2, 2001

The domain structure in strained garnet ferrite films and its behavior in an external magnetic field are studied using the Faraday effect. Based on the experimental results, a model of magnetization reversal in thin polycrystalline layers is proposed that describes the process of remagnetization as the development of fractal clusters. The model proposed is verified using a computer simulation of magnetization reversal. © *2001 MAIK "Nauka/Interperiodica".*

PACS numbers: 75.70.Kw; 75.60.Jk

A significant mismatch exists between the lattice parameter of a garnet ferrite (GF) film a_f and that of the substrate a_c (~0.5%, $a_f > a_c$), which gives rise to critical compressing strains (~10^8 N/m^2) in the film. X-ray investigations demonstrate that the film structure forms in this case as a "facet" [1], that is, as an aggregate of closely packed single-crystal grains of size on the order of the film thickness. This structure allows a strained GF film to be considered as a model of a thin polycrystalline ferromagnet layer.

The films under study of composition $(Bi,Y,Tm,Gd)_3(Fe,Ga)_2O_{12}$ were grown in the (111) plane on gallium–gadolinium substrates and possessed the following properties: saturation magnetization M_s ~ 5 kA/m, magnetooptic quality factor Q ~ 50 degree/dB (λ = 6328 Å), and thickness h = (4–6) μm. The high magnetooptic quality factor was obtained by using a high concentration of bismuth (about one atom per formula unit) [2], and the small film thickness gave rise to a through domain structure (DS). The combination of these properties allowed the magnetooptic Faraday effect to be used for studying the DS and its dynamics.

Figure 1a is a photograph of a grained film structure obtained in transmitted light. In this photograph, light grains are surrounded by dark grain boundaries, in which the main body of macroscopic defects is concentrated. Figure 1b displays a photograph of a DS obtained in polarized light for the same film area. A comparison of the photographs leads to the conclusion that the grain size approximately equals the domain width, and the domain boundary (DB) is localized at grain boundaries. Figure 1c presents the DS of the film under study in comparison with the DS of a conventional (unstrained) GF film. It is evident that the DS in the sample in hand has a pronounced fractal nature, though it retains the hexagonal symmetry due to remanent magnetic cubic anisotropy in the film plane.

The experimental study of magnetization reversal in a uniform magnetized state was carried out on a magnetooptic setup that allowed the DS dynamics to be observed and the hysteresis loop to be constructed [3]. The initial state of the film was obtained by its magnetization to saturation in the [111] direction perpendicular to the film plane. Thereafter, a field H in the backward direction was applied and varied from $-H_s$ to $+H_s$ (H_s = 24 kA/m is the saturation field).

It was found that the process of magnetization reversal consists of three main steps (Fig. 2):

At the first step (in the range of fields 0–H_c; H_c ~ 8 kA/m is the coercive force), the development of the new magnetic phase proceeds as the growth of single-fractal clusters with fractal dimensionality D = 1.7 (Figs. 2a, 2b). The growth centers are the nuclei of reverse magnetization (the measured nucleus density is ~5×10^7 m^{-2}). In this case, only the DB areas that bound the free ends of filamentary domains move in the directions of the [110] type.

At the following step, in fields higher than H_c, single-fractal clusters coalesce into a single multifractal structure whose fractal dimensionality becomes a function of field H. The development of the new phase (Figs. 2c, 2d) proceeds through the displacement of side walls of filamentary domains, because free ends of domains are virtually absent in these fields.

At the last step, in fields on the order of H_s, some areas of the film having the form of cylindrical magnetic domains (CMDs) of irregular shape remain unremagnetized. These areas collapse in turn up to the external field equal to H_s (Figs. 2e, 2f).

The process of the development of domains of the new phase observed here can be explained if the DB is considered to be combined, that is, composed of areas of a simple high-mobility Bloch wall and areas of a

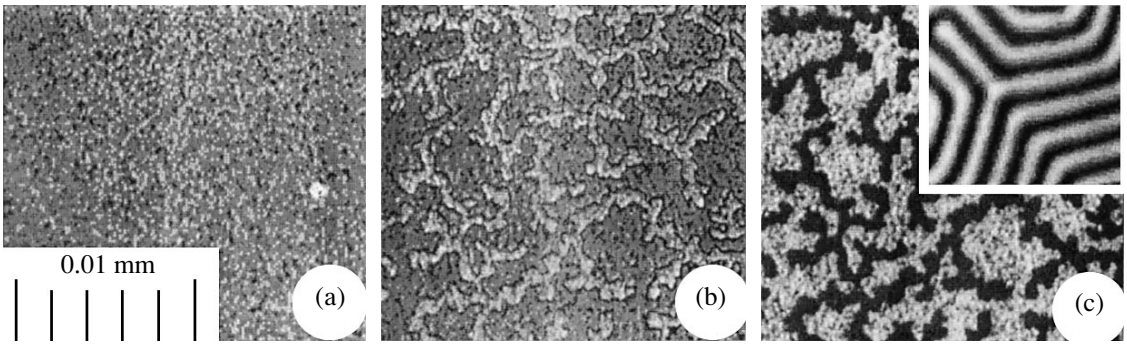

Fig. 1. Photograph of an area of the film under study $h = 5$ μm in thickness; (a) a photograph of the film structure, (b) a DS view in the same area (phase contrast), and (c) the DS of the film under study (amplitude contrast) in comparison with the DS (the fragment in the upper corner) of an unstrained GF film.

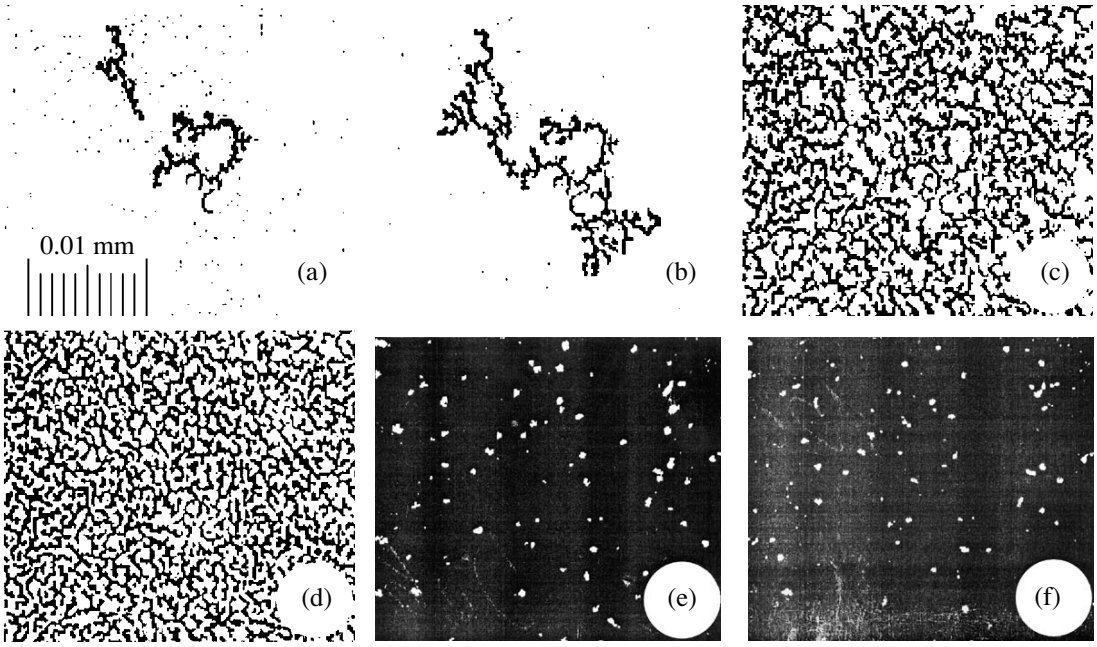

Fig. 2. Steps of sample remagnetization ($M_S = 5$ mA/m): (a) $H = 2.5$, (b) $H = 6.5$, (c) $H = 9.8$, (d) $H = 15.3$, (e) $H = 21.8$, and (f) $H = 26.2$ kA/m.

rigid wall with low mobility. The simple wall bounds the free ends of filamentary domains, and the rigid wall bounds their rectilinear sections. This suggestion is confirmed experimentally: free domain ends start to move in fields $H \sim 1$ Oe (80 A/m), and side walls start to move only in fields ~100 Oe (8 kA/m). The occurrence of rigid DB areas in strip domains was described, for example, in [4] and subsequently observed by many other authors. Only rigid DBs remain at the last step of magnetization reversal. Therefore, the resulting CMDs are rigid and must collapse in fields of 200–300 Oe (16–24 kA/m) [5]. In the films studied in this work, the saturation fields are 300–350 Oe (24–28 kA/m).

The fractal nature of both the DS and the process of its rearrangement should evidently be associated with the high density of defects concentrated in grain boundaries. If a certain average value of the magnetic field of surrounding defects is assigned to each grain, then these fields will be randomly distributed in the film plane. Hence, the DB in its motion will select such an easy direction in the film plane that the magnetic field of defects in this direction will be relatively low for a given external field H. Therefore, the growth direction of the free end of a filamentary domain must vary at random from one easy direction to another as the field H grows, which is observed experimentally. The branching of a domain can take place in two cases. First, this is possible when the magnetic fields of defects are equal in two possible growth directions. The probability of such an event is small. The second case, in which a domain bend, similar to the free end, also has a simple Bloch wall, is more realistic. Then, a new

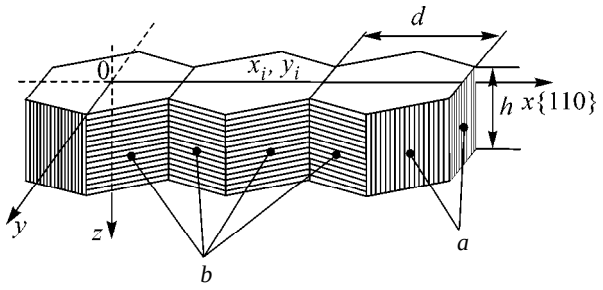

Fig. 3. Model of a filamentary domain: *a* a simple Bloch wall and *b* a rigid wall.

filamentary domain nucleates at the domain bend when the external field achieves a corresponding magnitude (see Fig. 3).

Based on the experimental data outlined above, we consider the following model of magnetization reversal for computer simulation. It is assumed that the film bulk consists of closely packed rigid dipoles oriented perpendicular to the film plane. Each dipole simulates a certain film grain and is a domain monomer. It is shaped like a hexagonal prism of height h equal to the film thickness and of transverse size $d = 2R$ (R is the radius of a circle inscribed in the hexahedron). This dipole shape corresponds to close packing and takes into account hexagonal magnetic anisotropy in the film plane. Monomeric domains with zero magnetic field of defects are nuclei of reverse magnetization in the model. DS development from these centers proceeds through the jumpwise motion of a planar DB (one of the prism faces) parallel to itself over a distance d. In this case, the neighboring dipole becomes remagnetized, etc. Thus, the filamentary domain is realized as a chain of monomeric domains whose free ends are bound by a simple Bloch wall and side walls are rigid (Fig. 3).

Computer simulation was carried out on the network of a honeycomb structure (Fig. 4). Let the geometric center of a network cell have coordinates x_i and y_j. Then, the magnetization reversal condition for the (i, j) cell is determined by the relationship

$$H \geq H_c^{i,j} + H_m^{i,j}, \tag{1}$$

where $H_c^{i,j}$ is the local magnitude of the magnetic field of defects for the (i, j) cell, and $H_m^{i,j}$ is the local magnitude of the magnetostatic field created by all remagnetized cells

$$H_m^{i,j} = \sum_{k,l}^{N} H^{k,l}, \tag{2}$$

where $(k, l) \neq (i, j)$, and N is the number of cells (a network of 200×200 cells was used; that is, $N = 4 \times 10^4$). The field $H^{k,l}$ was calculated as a field of a solenoid shaped like a regular hexahedral prism of height h and hexagon side of $2R/\sqrt{3}$ by the known method proposed, for example, in [6]. The field $H_m^{i,j}$ is calculated at each iteration step ΔH ($\Delta H = 80$ A/m). With allowance made for Eq. (2), Eq. (1) takes the form

$$H \geq H_c^{i,j} + \sum_{k,l}^{N} H^{k,l}. \tag{3}$$

The magnetic field of defects $H_c^{i,j}$ is selected from the set of arguments of the distribution function $F(H_c)$ and assigned at random to each cell. The distribution function is specified in the interval $[0–H_s]$ and normalized to the number of cells N.

At the given stage, the problem was in selecting the distribution function $F(H_c)$. A gamma distribution was

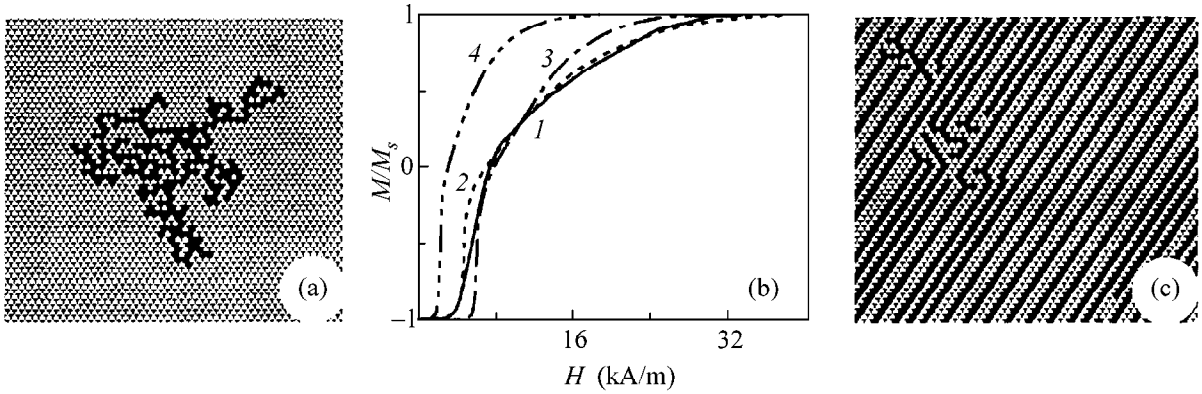

Fig. 4. Results of computer simulation for the process of sample remagnetization: (a) a fractal cluster obtained on a network of 200×200 cells in the field $H = 800$ A/m; (b) magnetization reversal curves: (*1*) experimental curve, (*2*) simulation curve for distribution parameters $\alpha = -0.3$ and $\beta = 2.8$, (*3*) the same for $\alpha = 0$ and $\beta = 1.0$, and (*4*) the same for $\alpha = 1.0$ and $\beta = 3.0$; and (c) the geometry of the simulated DS for the delta distribution of the magnetic fields of defects.

chosen as the trial function

$$F(H_c) = \frac{1}{\beta^{\alpha+1}\Gamma(\alpha+1)} H_c^{\alpha} e^{H_c/\beta}. \quad (4)$$

The best agreement with the experiment is obtained for $\alpha = -0.3$ and $\beta = 2.8$ (Fig. 4b). Apparently, this result should be associated with the fact that the main body of defects in the film is due to compressing critical strains whose magnitude is virtually constant in all film areas. Therefore, the magnetic fields caused by these strains form a compact domain, which corresponds to the distribution described by Eq. (4).

It should be expected that for a defect-free film the DS would be of the strip type. A DS of this geometry is observed in conventional CMD films. Within the framework of the model considered here, this situation implies the constancy of the magnetic field of defects at all film points. It can be modeled, e.g., by a delta distribution instead of the distribution given by Eq. (4). The DS geometry obtained by computer simulation for a sample with the same characteristics in the case of a delta distribution is shown in Fig. 4c. Its DS is actually of the strip type.

Thus, the results of computer simulation allow us to conclude that the proposed phenomenological model, in which the magnetization reversal process is considered as the development of fractal domain clusters, is confirmed, at least qualitatively, by the experiment.

Note in conclusion that we have studied a DS of fractal geometry and its rearrangement in strained GF films. The remagnetization of such samples has been studied in detail, and it has been found that this process proceeds as the development of fractal domain clusters. The results of experimental investigations allowed us to construct a model of a thin polycrystalline layer as an aggregate of rigid dipoles. These dipoles form branching chains of filamentary domains oriented along easy axes in the sample plane. Computer verification of the model demonstrates that the model proposed fully describes the hysteresis loop in the films studied in this work and predicts the DS geometry in typical CMD films. Note that the model developed in this work describes a sample composed, in principle, of an arbitrary number of particles, in contrast to the models proposed previously, for example, in [7, 8], for the remagnetization of polycrystalline layers, which consider samples containing one, two, and at most four grains. Note in conclusion that we applied a fractal approach to the description of a DS rearrangement in a magnetic field.

REFERENCES

1. D. M. Gualtieri and P. E. Tumelty, J. Appl. Phys. **57**, 3886 (1985).
2. A. Ya. Chervonenkis and A. M. Balbashov, *Magnetic Materials for Microelectronics* (Énergiya, Moscow, 1979), p. 102.
3. L. A. Dovbnya and B. V. Khramov, in *Proceedings of the International Conference of Young Scientists "Optics-99", St. Petersburg, 1999.*
4. D. I. Craik and G. Myers, Philos. Mag. **31**, 489 (1975).
5. A. H. Bobeck and E. Della Torre, *Magnetic Bubbles* (North-Holland, Amsterdam, 1975; Énergiya, Moscow, 1977).
6. T. O'Dell, *Magnetic Bubbles* (Macmillan, London, 1974; Mir, Moscow, 1978).
7. M. M. Solov'ev, Fiz. Met. Metalloved. **48**, 58 (1979).
8. A. V. Chernyshev and A. N. Kovriga, Zh. Tekh. Fiz. **66** (4), 68 (1996) [Tech. Phys. **41**, 333 (1996)].

Translated by A. Bagatur'yants